
**Development and validation of a
multilayer cloud detection algorithm
for the airborne demonstrator of the
direct detection Doppler lidar on
ADM-Aeolus**

Stephan Kox

Ludwig-Maximilians-Universität München



Meteorologisches Institut München

Dezember 2008

**Development and validation of a multilayer cloud detection
algorithm for the airborne demonstrator of the direct detection
Doppler lidar on ADM-Aeolus**

Stephan Kox

Diplomarbeit

durchgeführt am

Deutschen Zentrum für Luft- und Raumfahrt



im Rahmen eines Projektes der
Europäischen Raumfahrtagentur



vorgelegt von

Stephan Kox

aus Brunenthal

München, den 19.12.2008

Erstgutachter: Dr. Oliver Reitebuch

Zweitgutachter: Dr. Matthias Wiegner

Contents

1	Introduction	1
1.1	Impact of Clouds on Climate and Climate Change	2
1.2	Cloud Climatologies	3
2	Cloud Observations with Spaceborne Lidars	5
2.1	Lidar Principle	5
2.2	Doppler Wind Lidar	8
2.3	ADM-Aeolus - ALADIN	10
2.4	ICESat - GLAS	15
2.5	CALIPSO - CALIOP	23
2.6	Summary	31
3	Cloud Detection with the ALADIN Airborne Demonstrator	33
3.1	ALADIN Airborne Demonstrator - A2D	33
3.1.1	Transmitter	33
3.1.2	Telescope	35
3.1.3	Receiver	35
3.2	A2D - Simulator	39
3.2.1	Atmosphere	41
3.2.2	Clouds	44
3.2.3	Transmission	48
3.3	Cloud Detection from Mie Spectrometer	49
3.3.1	Signal-to-Noise Ratio	49
3.3.2	Scattering Ratio	53

3.3.3	Detection Algorithm	56
3.3.4	Simulated Signals and Minimum Detectable Cloud Optical Depth	59
3.3.5	Observed Signals and Multilayer Cloud Detection	65
3.4	Cloud Detection from Rayleigh Spectrometer	70
3.4.1	Signal-to-Noise Ratio	70
3.4.2	Detection Algorithm	72
3.4.3	Simulated Signals and Minimum Detectable Cloud Optical Depth	74
3.4.4	Observed Signals and Multilayer Cloud Detection	77
4	Comparison of A2D, MULIS and Cloud Radar	81
4.1	Ground Campaign 2007 - Overview	81
4.1.1	ADM-Aeolus Ground Campaign Objectives	81
4.1.2	METEK MIRA 36 - Cloud Radar of DWD	83
4.1.3	MULIS - Multiple Wavelength Lidar System of the University Munich	83
4.2	Cases	85
4.2.1	Multilayer Cirrus Cloud - 08.07.2007	85
4.2.2	Deep Broken Cumulus Clouds - 11.07.2007	89
4.2.3	Thin Cloud at Medium Altitudes - 13.07.2007	92
4.2.4	Thin Cirrus Cloud - 14.07.2007	96
4.2.5	Clear Sky and Thin Single Layer Cloud - 17.07.2007	100
4.3	Discussion	103
5	Conclusions	105
6	Outlook	107
	List of Figures	109
	List of Tables	115
	Appendix	117
	Bibliography	121

Acknowledgements

129

Chapter 1

Introduction

Over one hundred years ago Arrhenius [1896] elucidated that the burning of fossil fuels would increase the concentration of CO₂ within the earth's atmosphere, increasing the atmospheric greenhouse effect and thus leading to global warming.

More recently in 2008, the **Intergovernmental Panel on Climate Change** (IPCC) defined in its “Fourth Assessment Report” [IPCC, 2008] that changes in the atmospheric abundance of greenhouse gases and aerosols, in solar radiation and in land surface properties alter the energy balance of the climate system. These changes can be expressed in terms of **Radiative Forcing** (RF), which is used to compare how a range of human and natural factors drive warming or cooling influences on global climate.

The changes in RF are different for each mechanism taking place. Especially long-lived greenhouse gases lead to a positive RF while other mechanisms, for example, forced by aerosols result in a negative RF. The total aerosol radiative forcing can be split in the direct and the cloud albedo effect. Both effects are listed with a quite low scientific understanding.

But before giving an explanation of the influence of anthropogenic produced aerosols on clouds, the general influence of clouds on the climate and the atmospheric radiation budget has to be known.

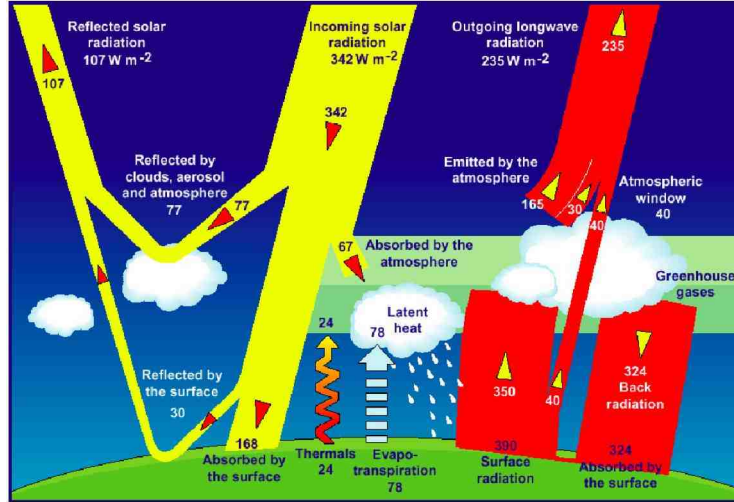


Figure 1.1: Schematic view on the earth's annual global energy budget [Kiehl and Trenberth, 1997].

1.1 Impact of Clouds on Climate and Climate Change

Beside the importance for the global and regional water circulation, clouds regulate solar and terrestrial radiation very effectively. Figure 1.1 shows, that the surface infrared radiation of $390 W m^{-2}$ corresponds to a blackbody emission at a temperature of $15^{\circ} C$ for the annual and global mean of outgoing fluxes. Some of the radiation leaving the atmosphere originates near the earth's surface and is transmitted relatively unimpeded through the atmosphere. This radiation originates from areas with no clouds and that is present in the part of the spectrum known as the atmospheric window [Kiehl and Trenberth, 1997]. The estimate of longwave radiation leaving via the atmospheric window decreases in the cloudy case to $80 W m^{-2}$, showing that there is considerable absorption and re-emission at wavelengths in the atmospheric window by clouds. The value is assigned to $40 W m^{-2}$ (Figure 1.1), which is simply 38% of the clear sky case, corresponding to the observed cloudiness of about 62% on the global scale. This emphasizes that very little radiation is transmitted directly to space although the atmosphere is transparent. The annual and global mean of shortwave incoming (solar) radiation of $342 W m^{-2}$ is reflected in parts by aerosols, clouds, and atmospheric

molecules (77 Wm^{-2}) and absorbed (67 Wm^{-2}) as well. Of course all the listed and shown numbers are only an annual and global average and change with improved in-situ, satellite, and ground-based measurements. As revealed by the **Earth Radiation Budget Experiment** (ERBE) [Harrison et al., 1990], clouds lead to a radiative cooling at Earth's surface by reflecting sunlight back to space (around -50 Wm^{-2}), while simultaneously warming the earth by absorbing and reemitting thermal radiation emitted by the surface and lower atmosphere (around 30 Wm^{-2}). Thus, combining shortwave and longwave contributions, the net global effect of clouds in our current climate, also determined by space-based measurements, is a net cooling of -20 Wm^{-2} depending on their microphysical structure and vertical extent.

This net cooling of clouds is affected by the mentioned indirect effect of aerosols, the so-called cloud albedo effect. Depending on their concentration and size aerosols influence the cloud's droplet size spectrum as condensation nuclei, which has an impact on the clouds radiation properties as well as on their lifetime and on precipitation [Wallace and Hobbs, 2006]. On the one hand the understanding of this effects is afflicted with the deficient knowledge of the aerosol distribution in the atmosphere, on the other hand there is still missing knowledge of the global horizontal and vertical distribution and the multilayering of clouds.

1.2 Cloud Climatologies

In order to study clouds and to predict them correctly in climate models, the **International Satellite Cloud Climatology Project** (ISCCP) was started as a major initiative to provide the climate modelling community with a definitive and flexible cloud climatology [Rossow and Schiffer, 1999]. The ISCCP data set of cloud amounts and other products is a more than 20 year archive of daily global observations with a nominal spatial resolution of 8 km and a temporal resolution of 3 hours. Since 1983 the infrared and visible radiances have been collected from imaging radiometers carried on the international constellation of geostationary weather satellites [Evan et al., 2007]. The ISCCP cloud datasets are used to determine cloud effects on Earth's radiation balance.

According to Rossow and Schiffer [1999] the accuracy of the ISCCP cloud amounts de-

depends on three factors: the validity of the cloud detection, the sensitivity of the cloud detection, and the accuracy of the areal cover fraction estimated by counting cloudy pixels with a finite resolution.

The first two factors depend on the magnitude of the detection thresholds, which vary with scene type in the ISCCP analysis. Additional, especially the upper-level cloudiness is underestimated, which is caused by missed detections of very thin clouds with minimum detectable cloud optical depths of 0.1 over ocean and 0.3 over land [Wielicki and Parker, 1992]. Another example for detection problems are polar clouds, which form at low temperatures and low solar illuminations, where the satellite radiometer's sensitivity is reduced [Mokhov and Schlesinger, 1993, 1994].

With the new option of orbiting lidars like GLAS onboard ICESat (Section 2.4) and CALIOP onboard CALIPSO (Section 2.5), providing the capability of obtaining high resolution of atmospheric structure, the global determination of cloud top height, cloud bottom height (for clouds with optical depth $< 3 - 4$), multilayer cloud structure and planetary boundary layer height [Palm et al., 2005], the knowledge especially of high altitude and multilayer clouds can be improved.

The aim of this thesis is to develop and to validate a cloud detection routine for the airborne prototype of the **Atmospheric Dynamics Mission** ADM-Aeolus, which will be the first **Doppler Wind Lidar** (DWL) and the first European lidar in space [Stoffelen et al., 2005]. In addition to global wind observations, ADM-Aeolus will perform aerosol and cloud detection, which completes and continues the measurements performed by ICESat and CALIPSO.

Beside the lidar and the **Doppler Wind Lidar** (DWL) principle, the ADM-Aeolus mission and the two spaceborne lidars, GLAS and CALIOP, are described in combination with their used detection and classification algorithms to give a first orientation in Chapter 2. In Chapter 3 the prototype of ADM-Aeolus, the **ALADIN Airborne Demonstrator** (A2D), is explained in detail and the end-to-end simulator give a first evidence of cloud detection and of the minimum detectable cloud optical depths. In order to analyze the possibilities of the cloud detection routine, data sets collected at ground based measurements with A2D are compared to the **Multiple wavelengths Lidar System** (MULIS) of the University of Munich in Chapter 4.

Chapter 2

Cloud Observations with Spaceborne Lidars

Nowadays remote sensing is widely spread in the atmospheric research community. Especially active remote sensing like **light detection and ranging** (lidar) and **radio detection and ranging** (radar) has become fairly common. Like radar, lidar is mainly used for profiling the earth's atmosphere. High spatial and temporal resolution of the measurements, the possibility of observing the atmosphere in ambient conditions, the potential of covering the height range from the ground to high altitudes, observations during night, including the high flexibility like measurements from an aircraft or even from space make this kind of observations even more attractive (for an overview of lidar and atmospheric application see Weitkamp [2005]).

2.1 Lidar Principle

A lidar consists of three subsystems: the transmitter, the receiver, and the detection system.

The **light amplification by stimulated emission of radiation** (laser) transmitter is the light source, which emits photons in a pulsed beam. Those photons are scattered by atmospheric molecules (oxygen, nitrogen, etc.) and particles (clouds and aerosols). Molecules evoke Rayleigh scattering, while particles cause Mie scattering.

Rayleigh scattering occurs when the wavelength of the propagating light is much larger than the diameter of the particles, as in the case of interaction of visible and ultraviolet light with air molecules.

Due to the wavelength dependency of the intensity of Rayleigh scattering with λ^{-4} , shorter wavelengths are scattered far more than larger wavelengths. So the gain of short wavelengths, like the 355 *nm* used for Atmospheric Dynamics Mission ADM-Aeolus, is an increased molecular backscatter in the atmosphere [ESA, 1999, 2008].

Mie scattering is caused by aerosols and clouds, which are atmospheric particles with a diameter close to, or even larger than the wavelength of the radiation. Here, the intensity of the backscattered light depends on the particle concentration and not or only slightly on the wavelength. It increases simultaneously with air pollution, clouds, fog, and haze.

These two backscatter mechanisms caused by the atmosphere will be reconsidered in Section 3.2, where the atmospheric simulation of the ALADIN Airborne Demonstrator is explained in detail.

Figure 2.1 shows a schematic overview of the typical backscattered signal of a spaceborne lidar like the ADM-Aeolus. The transmitter emits laser pulses (red) in direction of the lidar line-of-sight (yellow). These pulses are backscattered by atmospheric molecules, aerosols, and cloud particles.

The received energy $E(\lambda, R)$ of a lidar can be calculated with the lidar equation [Measures, 1991]:

$$E(\lambda, R) = E \cdot \frac{\Delta R \cdot A_0}{R^2} \cdot k(\lambda) \cdot \beta(R) \cdot T^2(R) \quad (2.1)$$

where R is the range from the lidar, E the energy and λ the wavelength of the transmitted pulse, and $\beta(R)$ the atmospheric backscatter coefficient. $\frac{A_0}{R^2}$ is the acceptance solid angle of the receiving optics with A_0 being the collecting area of the telescope. The instrument constant $k(\lambda)$ considers the response of the receiver like the spectral transmission. Other very important parts of the lidar equation are the atmospheric two-way transmission T^2 and the range resolution ΔR .

The receiver collects the light backscattered by the atmosphere with a telescope. This collected signal is time-dependent with the velocity of light $c = 2.9979 \cdot 10^8 \frac{m}{s}$. Using the equation $R = \frac{c \cdot t}{2}$, the time t between the transmission of the laser pulse and the

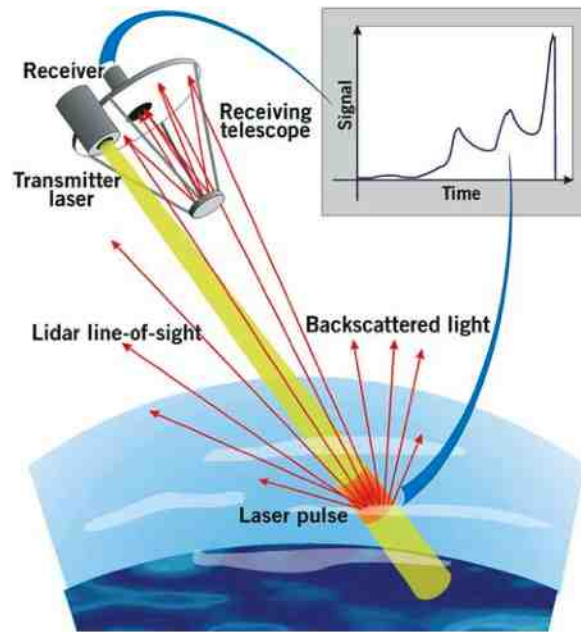


Figure 2.1: Schematic view on a spaceborne lidar [ESA, 2008].

reception of the backscattered signal can be directly related to the range R , where the scattering occurs.

The typical signal of a spaceborne lidar is shown at the right top of Figure 2.1, where the first and second peak are caused by aerosols and clouds, whereas the strongest peak is the ground return signal.

2.2 Doppler Wind Lidar

Doppler wind lidar (DWL) systems determine the **line-of-sight** (LOS) wind speed as a function of range using light-scattering particles in the air (aerosols and molecules) as tracers. The atmospheric particles moving with the wind velocity cause a frequency shift of the backscatter signal due to the Doppler effect. The frequency shift is related directly to the wind velocity along the laser beam (for an overview see Weitkamp [2005, p.325]).

The Doppler effect is a phenomenon that can be observed whenever there is relative motion between a source of waves, most notably sound, water or light waves, and an observer. The Doppler effect is the shift of a wave's frequency caused by the relative motion of an observer and the wave source. This motion causes the frequency of the wave to increase as the source and observer move towards each other and to decrease as they move apart. The Doppler effect was first described by the Austrian physicist Christian Johann Doppler in 1842.

Under a Doppler shift, the optical frequency of light is shifted by a factor of $\frac{v}{c}$, where v is the velocity at which the observer is approaching or receding from the source, and c is the speed of light. Since $v \ll c$, the resultant frequency f of the light may be written as [Weitkamp, 2005, p. 326]:

$$f' = f_0 \left(1 + \frac{v}{c}\right) \quad (2.2)$$

where f_0 is the frequency of the transmitted light.

The Doppler shift actually detected by a DWL system is the result of two Doppler shifts. The first shift in frequency is caused by the scattering particles (aerosols, clouds, and molecules) being investigated, which constitute a moving observer. The second shift arises, because the particles in the air then act as moving sources scattering the light, which has already been Doppler-shifted. Since they are sources moving with respect to the lidar system (now a stationary observer), another Doppler shift f'' is seen on the already Doppler-shifted light with frequency f' [Weitkamp, 2005, p. 326]:

$$f'' = f' \left(1 + \frac{v}{c}\right) \quad (2.3)$$

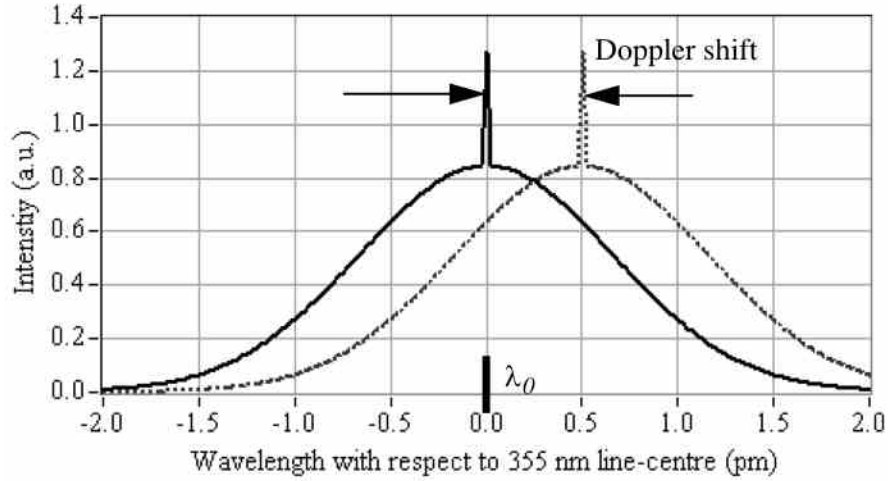


Figure 2.2: An example of Mie and Rayleigh backscatter intensities from a 355 nm (λ_0) lidar system versus wavelength. The spectrum in respect to 0 $\frac{m}{s}$ LOS wind speed (solid line) and a Doppler-shifted spectrum referring to a wind speed of 210 $\frac{m}{s}$ (dashed line) is illustrated [Paffrath, 2006].

The Doppler frequency shift detected back at the source is given by $\Delta f_D = f'' - f_0$. Assuming $v \ll c$, the shift Δf_D is given by $\Delta f_D = 2 \cdot f_0 \frac{v}{c}$, or in terms of wavelength:

$$\Delta \lambda_D = 2 \cdot \lambda_0 \frac{v}{c} \quad (2.4)$$

where λ_0 is the laser wavelength. An example of a wavelength shifted Rayleigh and Mie spectrum for the ADM-Aeolus is illustrated in Figure 2.2. In this case, a Doppler shift of 0.5 pm corresponds to a LOS wind speed of 210 m/s.



Figure 2.3: An illustrated view on ADM-Aeolus in orbit [<http://www.esa.int/esaLP>].

2.3 ADM-Aeolus - ALADIN

The Atmospheric Dynamics Mission ADM-Aeolus (Figure 2.3) of the **European Space Agency** (ESA) will be the first **Doppler Wind Lidar** (DWL) in space and the first European lidar in space [Stoffelen et al., 2005]. Aeolus will be launched into a sun-synchronous orbit of 408 km [Endemann et al., 2008]. Its launch is scheduled for late 2010.

ADM-Aeolus (Figure 2.4) will carry only one instrument, the **Atmospheric Laser Doppler Instrument** (ALADIN), which is designed to measure vertical profiles of windspeed in the line-of-sight direction (from 0-30 km altitude) in 50 km (7 seconds) averaged intervals within the remainder of 200 km (28 seconds). The decision to use burst mode measurements was taken in the early stages of mission planning in order to reduce power demand and to fit the expected grid size development down to 50 km in numerical weather prediction [Tan et al., 2007].

ALADIN is a direct detection lidar with a dual receiver for Mie and Rayleigh backscatter, operating in the ultra-violet spectrum (355 nm) transmitted by a frequency-tripled **Neodymium doped Yttrium Aluminium Garnet** (Nd:YAG) laser with a pulse energy of 120 mJ and a repetition rate of 100 Hz. It is pointing 35° to the anti-sun side with its 1.5 m diameter telescope, so that the wind velocity component orthogonal

to the ground track can be measured [ESA, 2008]. ADM-Aeolus will provide several data products. The provided raw data with a horizontal resolution of 1 – 3.5 km will be processed on ground to 50 km averages. The vertical resolution depends on the altitude range bins (–1 km to 16.5 km for the Mie channel and 0.5 km to 26.5 km for the Rayleigh channel) with a changeable resolution of 250 m (close to the ground) up to 2 km during one orbit. The measurement geometry is depicted in Figure 2.4.

The main objective of the ADM-Aeolus is to perform **Horizontal Line of Sight** (HLOS) wind measurements, which will be calculated according to the Doppler effect in Section 2.2 for the Mie spectrometer, receiving photons backscattered by aerosols and clouds, and the Rayleigh spectrometer, receiving photons backscattered by atmospheric molecules. These two spectrometers are used to measure wind HLOS wind in altitudes where no aerosol or cloud is present. Another advantage of using both receiver is the possibility of different measurement ranges, so both channels will be able to use different vertical resolutions or even measure in different altitudes. In addition to the raw data, laser internal calibration, attitude information, and receiver response calibration data will be transmitted.

Before integrating the raw data to 50 km averages during on ground processing, aerosol and cloud detection is performed to segregate clear air regions and those affected by aerosols and clouds [Tan et al., 2007].

Atmospheric data processed from ADM-Aeolus measurements will be provided for each range bin (layer) i in the following data products [Flamant et al., 2008]:

- Presence of clouds or aerosols in each vertical range bin,
- Optical depths,
- Scattering ratios $\rho_i = \frac{\beta_{A,i} + \beta_{Mol,i}}{\beta_{Mol,i}}$, where $\beta_{A,i}$ is the backscatter coefficient for particles and $\beta_{Mol,i}$ for molecules,
- Backscatter-to-extinction ratios $k_{A,i} = \frac{\beta_{A,i}}{\alpha_{A,i}}$, which can be calculated by the scattering ratio and the received signal,
- Consolidated HLOS wind profiles using external atmospheric parameters (pressure, temperature),

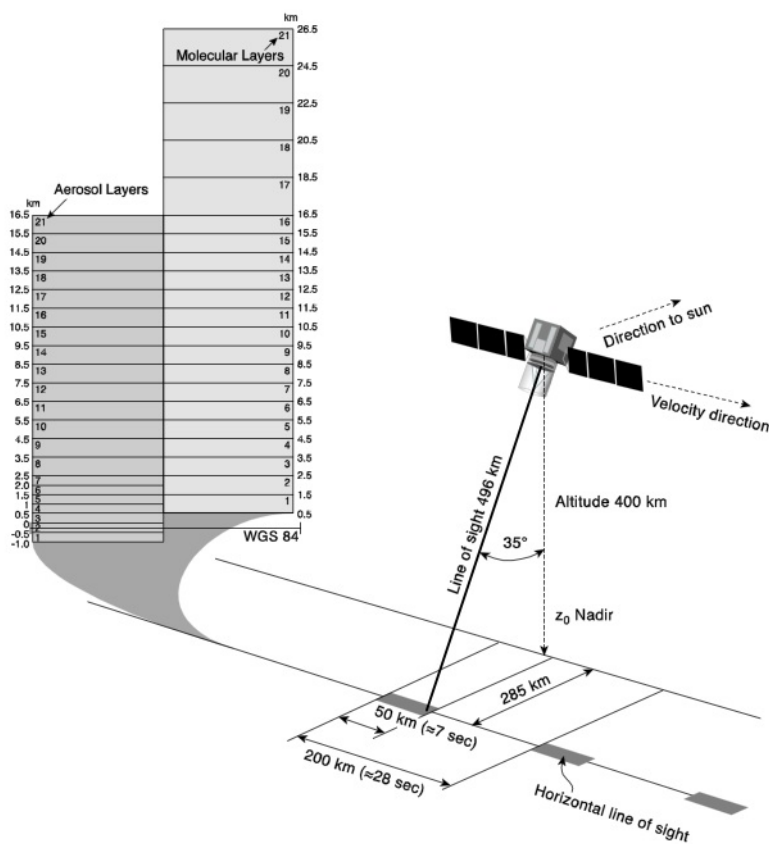


Figure 2.4: Line-of-sight viewing geometry and proposed vertical distribution of the range bins for the ADM-Aeolus, showing vertical sampling by the particle (Mie) and molecular (Rayleigh) channels separately [Stoffelen et al., 2005].

- Statistics of atmospheric variability, and
- Wind profiles of the atmosphere will finally result from **Numerical Weather Predictions** (NWP) assimilation processing.

The assimilation of the data in NWP will lead to improved wind field analyses (see references in Reitebuch and Weissmann [2008] and Stoffelen et al. [2005]), which will be distributed to the atmospheric research community.

Currently, the development of a “feature finder” and the **Scene Classification Algorithm** (SCA) for satellite observations is under progress. So, the aim of this diploma thesis is to develop a cloud detection algorithm for the ALADIN Airborne Demonstrator to get a first view on the cloud detection behaviour ground based lidar observations. This prototype is described in Section 3.1, but in the following a rough concept of the planned aerosol and cloud detection in combination with the layer discrimination algorithm [Flamant et al., 2008] is given:

Based upon the Mie channel a “feature finder” algorithm is applied, which identifies the range bins that contain particles (like aerosols and clouds) and computes a scattering ratio (a full explanation will follow in Chapter 3). With this information, a discrimination of clear air and cloud/aerosol layers can be realized. For each range bin i , measurements at a 3.5 km -scale will be used to derive the fraction of aerosol or cloud layers (not discriminated at this point) in the 50 km observation.

The algorithm is designed to retrieve:

- the particle local optical depth $LOD_{A,i}$ or a mean extinction coefficient for particles $\alpha_{A,i}$,
- backscatter-to-extinction ratio for particles or the lidar ratio $S_{A,i} = k_{A,i}^{-1}$,
- and scattering ratio ρ_i .

A rough flowchart of the retrieval algorithm described by Flamant et al. [2008] is shown in Figure 2.5. The auxiliary data sets will be used for signal processing on ground (atmospheric temperature and pressure profiles for processing of the Rayleigh channel signal and k_p^{aux} for processing of the Mie channel signals). This k_p^{aux} is the computed backscatter-to-extinction ratio for different types of aerosols, if the Rayleigh

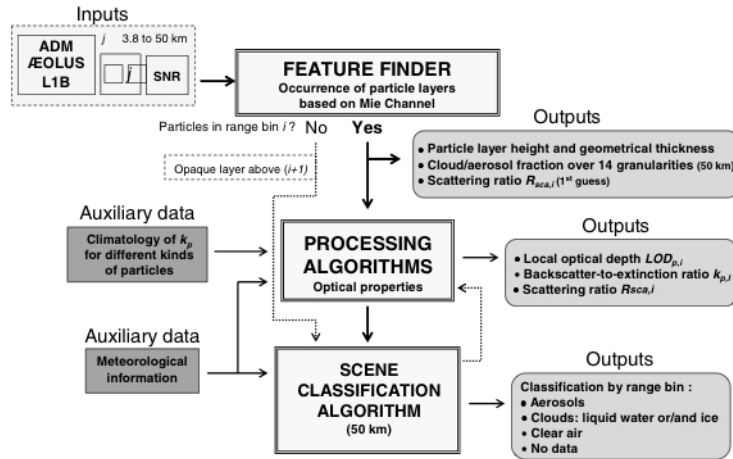


Figure 2.5: Basic concept of the algorithm to retrieve aerosol and cloud properties using ADM-Aeolus data, geophysical variables provided by **Global Circulation Model** (GCM) analysis, and microphysical properties for particles [Flamant et al., 2008].

channel is not available. Currently this database is under construction. The SCA at 50 *km*-scale will discriminate the atmospheric components detected in each range bin (aerosols, clouds, or clear air).

Two spaceborne lidar mission, ICESat and CALIPSO, were launched recently. Their aerosol and cloud detection algorithms are described briefly in the following sections to get an overview about the different options of aerosol and cloud detection.



Figure 2.6: An illustrated view on ICESat [<http://icesat.gsfc.nasa.gov>].

2.4 ICESat - GLAS

In 2003, the **Geoscience Laser Altimeter System** (GLAS) was launched onboard of the **Ice, Cloud, and Land Elevation Satellite** (ICESat) (Figure 2.6). GLAS measures nadir lidar profiles of the atmosphere at two wavelengths (532 nm and 1064 nm) with a resolution of 76 m vertical (compared to 15 cm at surface measurement elevations) and 172 m horizontal (equivalent to a pulse repetition frequency of 40 Hz) during its flight in an orbit of 600 km [Zwally et al., 2002].

Beside ice sheet mass balance, land topography, and vegetation characteristics, GLAS provides lidar signals of cloud and aerosol boundaries, corrected due to the attenuation caused by multilayering, optical thickness and extinction, and backscatter cross sections on a global scale [Spinhirne et al., 2005] using ancillary meteorological data.

A short description of cloud and aerosol boundary detection and the used algorithm [Palm et al., 2002] is given in the following:

First of all, ancillary meteorological data like vertical profiles of pressure $p(z)$ and temperature $T(z)$ are necessary to derive the molecular backscatter coefficient β_m at the calibration altitude z_C of 30 km [Measures, 1991]. With this meteorological data and some transformations of the ideal gas law, the calibration constant C_λ for $\lambda = 532\text{ nm}$

and for $\lambda = 1064 \text{ nm}$ is derived as:

$$C_\lambda = \frac{\overline{P'_\lambda(z_C)}}{\overline{\beta_m(z_C, \lambda)} \cdot T^2(\lambda)} \quad (2.5)$$

where $\overline{P'_\lambda(z_C)}$ and $\overline{\beta_m(z_C, \lambda)}$ are the horizontal average (equivalent to an averaging of 10 – 20 minutes) of the vertically integrated, normalized lidar signal and the molecular backscatter through the 2 *km* thick calibration layer around an altitude of 30 *km*.

P'_λ is the normalized lidar signal containing the range-correction R^2 and solar background energy. The two-way transmission $T^2(\lambda)$ is calculated for the attenuation forced by molecular ($T^2(532 \text{ nm}) = 0.95$) and ozone ($T^2(532 \text{ nm})$ lower than one, depending on the ozone absorption coefficient, compiled by Iqbal [1984]) components from the top of the atmosphere to the calibration altitude of 30 *km*. At altitudes above 10 *km* the decrease of the two-way transmission caused by aerosols can be neglected.

Finally the height dependent calibrated attenuated backscatter coefficients $\beta'_{532}(z)$ are retrieved taking into account the not negligible attenuation by ozone $T_{O_3}^2$ at 532 *nm*:

$$\beta'_{532}(z) = \frac{P'_{532}(z)}{(C_{532} \cdot T_{O_3}^2(532, z))} \quad (2.6)$$

where $P'_{532}(z)$ is the measured lidar signal and C_{532} the calibration constant from Equation 2.5 for the wavelength of 532 *nm*.

In clear air regions, scattering is caused entirely by air molecules (Rayleigh scattering), while the presence of particles leads to scattering above the Rayleigh scattering values. Due to this dependency and to the fact that the absorption of water vapour at the GLAS lidar wavelength is negligible, the backscatter in particle-rich regions (e.g. cloud and aerosol layers) exceeds the Rayleigh backscatter coefficient, as depicted in Figure 2.7.

Here, this dotted pure Rayleigh backscatter coefficient is calculated using the U.S. Standard Atmosphere consisting of basic data like vertical profiles of temperature and pressure [Champion, 1985].

This means, that the pure Rayleigh backscatter profile derived from temperature and pressure profiles, can be used as a baseline threshold to detect particle regions in a

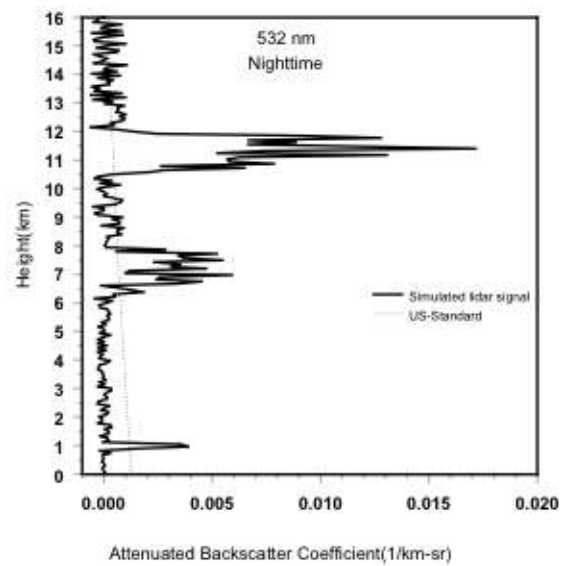


Figure 2.7: Simulated GLAS profile of attenuated backscatter coefficients at 532 *nm* in a cloudy atmosphere (black line)[Palm et al., 2002]. The dotted line shows the computed attenuated backscatter coefficients for the U.S. Standard Atmosphere for the same wavelength.

profile. However, owing to the attenuation of the lidar signal after passing through the first layer in a profile, this Rayleigh threshold would have values too high to detect other layers below, which gets obvious in Figure 2.7, where no aerosol layers are detectable at 2 to 6 *km* altitudes, below the last cloud peak in the backscatter profile.

In order to derive an optimum threshold, it is necessary to find a measure of random noise, which strongly influences the detection sensitivity, especially at weak aerosol and cloud layers. In general, this noise can be represented by the standard deviation *STD* of the lidar signal in a particle-free segment of the profile (for example in 18 - 19 *km* altitude), $P'(z = 18 \text{ km})$. In this region, the signal is only influenced by the molecular scattering and the solar background light.

The threshold $T_s(z)$ will be the sum of the minimum attenuated molecular backscatter $\beta'_m(z)$ and a constant fraction of the standard deviation *STD*. The value of the constant fraction c_f was determined by sensitivity studies between 0.25 – 0.5.

$$T_s(z) = (\beta_m(z) + c_f \cdot STD) \quad (2.7)$$

A profile of layer signal thresholds is now constructed by piecemeal, linear interpolation of the segment values. The interpolation is done at GLAS vertical resolution of 76.8 *m*. The interpolated profile will serve as a layer signal baseline upon which the presence of layer signals will be tested. So, the threshold (Equation 2.7), first taken in an aerosol free region, is updated during the measurements of an atmospheric profile.

This threshold profile has the following properties:

- Threshold values will be computed from the profile itself (automatic adjustment to current situation).
- Threshold values computed at a given level will be influenced by the attenuation of the lidar signal above.
- This technique will be valid for any temporal resolution.

After the threshold has been established for the lidar signal, the aerosol and cloud layer boundaries are sought in the following manner:

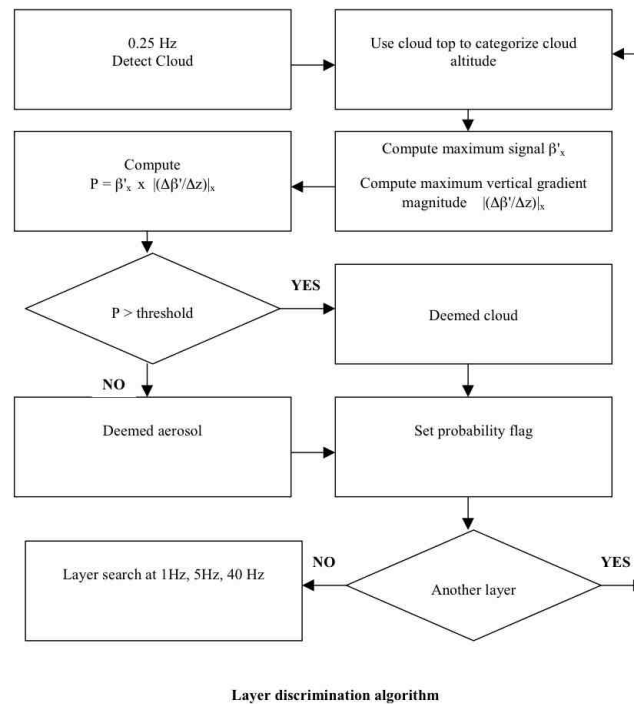


Figure 2.8: Aerosol and cloud layer discrimination algorithm [Palm et al., 2002].

The lidar signal is tested from the top of the profile to the bottom. If a value is found to exceed the threshold, it is identified as a potential layer sample. If a specified number of potential consecutive layer samples is found, the segment is designated a layered region. The top of the layered region is located at the height, where the highest of those samples was found. This testing continues under the stipulation that the profile is in a layered segment. The layer discrimination continues until several consecutive samples are found to be lower than the layer threshold, which indicates a layer-free region. The bottom of the layer is the point, where the first of the consecutive particle-free values was found. The testing then continues downward for the top of another feature, until Earth's surface is reached.

A rough flowchart of the feature detection and discrimination algorithm is shown in Figure 2.8, where the aerosol and cloud boundary analysis is first done on a 4 *s*-averaged profile (equivalent to a frequency of 0.25 *Hz*, or a horizontal resolution of 27.5 *km*) as

	Aerosol	Cloud
Signal Magnitude (top)	Smaller	Larger
Signal Gradient (top)	Smaller	Larger
Altitude (top)	Lower	Higher
Horizontal Extent	Wide spread	More localized
Horizontal Uniformity	More uniform	Less uniform
Vertical Extent	Larger	Smaller
Vertical Uniformity	More uniform	Less uniform
Relative Humidity	Lower	Higher
Attenuation	Lower	Higher

Table 2.1: Comparative attributes of aerosol and cloud layers [Palm et al., 2002].

the basis for the equivalent analysis of the four 1 *s*-profiles (1 *Hz*, or 6.9 *km*), shown in Figure 2.8. In the 1 *s*-profile, the detection is limited to the already detected boundaries of the averaged 4 *s*-profile due to the lower **Signal-to-Noise Ratio** SNR in the 1 *s*-profile, which results in incorrectly identified layers.

In the same manner, this layer detection is done for better time resolutions like 0.2 *s* (5 *Hz*, or 1.4 *km*) and 0.025 *s* (40 *Hz*, or 172 *m*). This procedure will allow detection of low altitude cloud layers that typically have strong lidar signals and horizontal distributions varying at short horizontal scales.

Once several cloud layers are detected, it is necessary to discriminate clouds and aerosols. In general, there are several layer attributes which can be used for this discrimination, as depicted in Table 2.1. These criteria were determined by modeling studies and by studies of atmospheric lidar data gathered by different high altitude lidars.

A discrimination of aerosol and cloud particles cannot be done by simply looking at the particle size due to the size distribution overlap shown in Hinds [1998], although in general cloud particles are larger than aerosol particles. According to Wang and Sassen [2001] and Liu et al. [2004], aerosol and cloud layers can be distinguished by the different influence on the lidar signal. While cirrus and water cloud layers cause a strong peak in the backscattered signal and a strong attenuation below, subvisible cirrus and aerosol layers result in a lower gradient of signal increase and attenuation

below.

So, for an operational threshold, there are difficulties in quantifying some of the listed attributes (horizontal extent, horizontal homogeneity, vertical extent, vertical homogeneity, relative humidity, and attenuation). Therefore, only the signal magnitude, signal gradient, and the altitude of the top of each layer will be used in the layer discrimination procedure based upon a thresholding process, where the value of a single parameter serves to distinguish between clouds and aerosols. Each layer detected in the averaged 4 s-profile will be assigned to an altitude category based upon the height of the layer's top. For each layer, a parameter composed of the product of the layer's maximum signal β'_x and the maximum vertical gradient magnitude $|\frac{\Delta\beta'}{\Delta z}|_x$ will be computed. Cloud layers will tend to have higher values than aerosol layers. This value will be compared to a threshold value determined for each altitude category. If the computed product exceeds the threshold, it is identified as a cloud, otherwise as an aerosol layer. Results for this discrimination measured by GLAS are shown in Figure 2.9. Here the GLAS lidar signal over China on October 23, 2003 is shown with clouds up to 16 km in combination with aerosols close to the ground [Spinhirne et al., 2005].

Clouds are plotted in blue, aerosols in yellow, and the analyzed planetary boundary layer in red. The ground is plotted in green. At the beginning of the measurement timeline, cirrus clouds up to 16 km with some mid-altitude clouds below are easily identifiable from 16° to 20° North. Over mainland China a strong planetary boundary layer is established with a top at 2 – 3 km. Within and above this boundary layer aerosols are visible over nearly the complete timeline. At 12:01, 12:04, and 12:07 clouds with different altitudes are detected, reaching 5 – 10 km height. It is obvious, that GLAS is not able to detect aerosol layers and the planetary boundary layer below some clouds. This effect is caused by the strong attenuation forced by the optical thickness of these clouds.

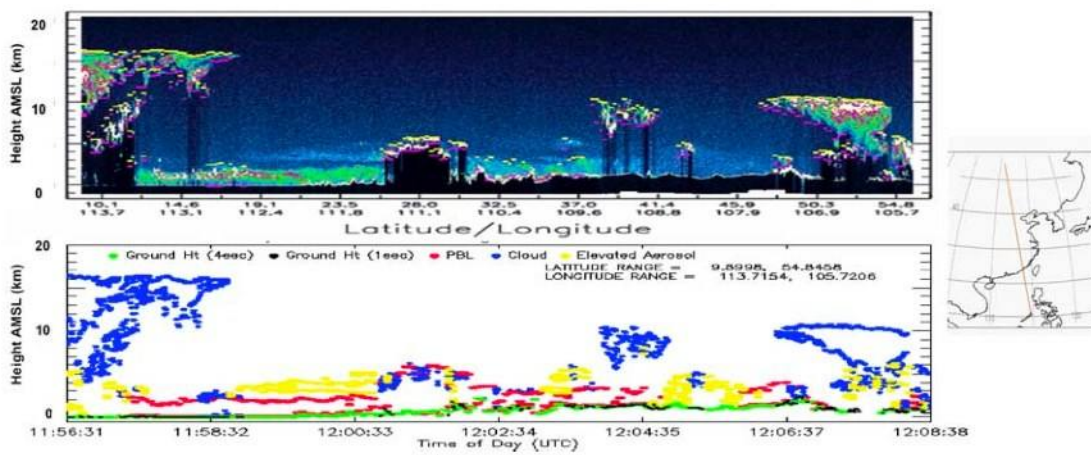


Figure 2.9: GLAS lidar over China on October 23, 2003 (top). GLAS aerosol and cloud layer height level data products produced from analysis of the signal (bottom) [Spinhirne et al., 2005].

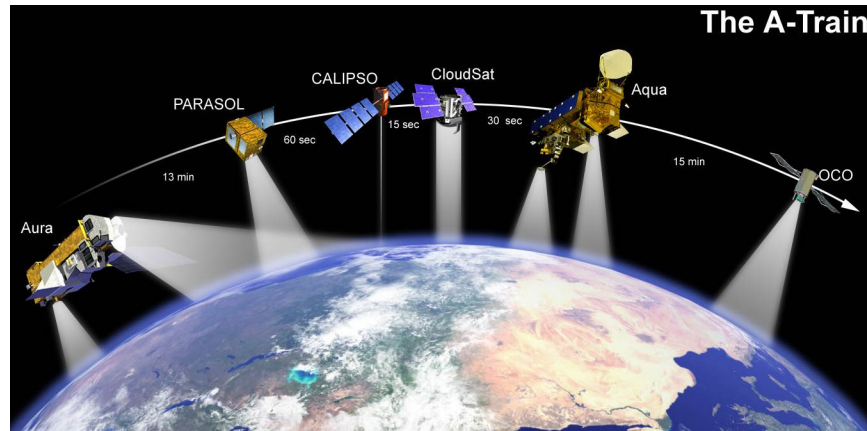


Figure 2.10: NASA afternoon train [<http://www-calipso.larc.nasa.gov>].

2.5 CALIPSO - CALIOP

Launched in April 2006, the **Cloud-Aerosol Lidar and Infrared Pathfinder Satellite Observations** (CALIPSO) mission provides global observations of aerosols and clouds with its onboard lidar **Cloud-Aerosol Lidar with Orthogonal Polarization** (CALIOP), the **Imaging Infrared Radiometer** (IIR) and the **Wide Field Camera** (WFC).

CALIPSO flies as a part of the **National Aeronautic and Space Administration** (NASA) afternoon constellation (A-Train) together with Aqua, CloudSat, PARASOL, and Aura (Figure 2.10). OCO is going to be launched in 2009. CALIPSO was injected into an orbit of 705 km . All satellites together provide simultaneous measurements of aerosols, clouds, relative humidity, temperature, and radiative fluxes for the first time. As depicted in Table 2.2, one of the features performed by CALIOP is the detection of cloud height, thickness, multilayering, and aerosol/cloud vertical distributions [Winker et al., 2002].

CALIOP uses a Nd:YAG laser emitting simultaneous, co-aligned pulses at 1064 nm and 532 nm wavelength with a repetition rate of 20.16 Hz (horizontal resolution of 333 m), a 1 m -diameter telescope, and three receiver channels, which collect the backscattered signals:

Science Objective	Measurement	CALIPSO
Direct aerosol forcing	Aerosol vertical distribution and extinction profiles	CALIOP
	Aerosol optical depth	CALIOP
	Aerosol type information	CALIOP
Indirect aerosol forcing	Aerosol and cloud vertical distributions	CALIOP
Longwave surface and atmospheric fluxes	Cloud height and thickness, multilayering	CALIOP (thin cloud)
	Cloud ice/water phase	CALIOP (profiles)
	Cirrus emissivity and particle size	CALIOP + IIR + WFC
Cloud radiative feedbacks	All elements of longwave surface/atmospheric fluxes plus: Cloud optical depth	CALIOP

Table 2.2: Measurement objectives of the CALIPSO mission [Winker et al., 2002].

One channel measuring the 1064 *nm* backscatter intensity and two channels measuring orthogonally polarized components of the 532 *nm* backscatter signal. It is possible to derive the backscatter coefficients (532 *nm* and 1064 *nm*), the color ratio of the backscatter coefficients ($\frac{532 \text{ nm}}{1064 \text{ nm}}$), and the depolarization ratio of the 532 *nm* channels [Winker et al., 2007]. Beside vertical profiles of aerosols, CALIPSO delivers vertical profiles of clouds, primarily from the 532 *nm* channel. The vertical resolution of the 532 *nm* channel is altitude-dependent from 30 *m* (up to 8.2 *km*) to 300 *m* (30 – 40 *km*). For each profile, cloud and aerosol layers are detected by a threshold detection technique [Vaughan et al., 2004].

This threshold is constructed based on estimates of both random and signal-induced noise levels. Because these estimates are derived from the profile being analyzed, the magnitudes of the threshold values scale automatically with increased signal averaging. In the following, a short description of the cloud detection algorithm of the CALIOP Algorithm Theoretical Basis Document [Vaughan et al., 2005, 2008] will be given:

The CALIPSO algorithm, scanning for aerosol and cloud layers, is applied to the range-resolved array of attenuated scattering ratios for every profile, which is calculated by the

attenuated backscatter coefficients and meteorological profile data. The meteorological data are provided by the NASA's **Global Modelling and Assimilation Office** (GMAO) numerical model. The attenuated backscatter coefficient $\beta'(z)$ is calculated for every profile as:

$$\beta'(z) = \frac{R^2 \cdot P(z)}{E \cdot G_A \cdot C} \quad (2.8)$$

where R is the range from the satellite to the sampled volume, $P(z)$ the measured signal after background subtraction and artifact removal, E the laser energy, G_A the amplifier gain, and C is the lidar calibration factor. The calibration factor is determined by comparing the measured 532 nm parallel channel signal from 30 – 34 km altitude to an estimate of the parallel backscatter coefficient computed from a modelled atmospheric density profile. This altitude is chosen for a calibration due to the low aerosol content. The calibration factor is then transformed to the 532 nm perpendicular and both 1064 nm channels. $\beta(z)$ is declared as the volume backscatter coefficient at altitude z . The two-way transmission $T^2(z)$ (i.e., signal attenuation) is part of the lidar calibration factor calculation.

In order to calculate the attenuated scattering ratios, first the attenuated clear air backscatter $\beta'_{air}(z)$ has to be calculated using temperature, pressure, and ozone profiles from the GMAO model:

$$\beta'_{air}(z) = \beta_m(z) \cdot T_m^2(z) \cdot T_{O_3}^2(z) \quad (2.9)$$

where $\beta_m(z)$ is the height-dependent molecular backscatter coefficient, $T_m^2(z)$ and $T_{O_3}^2(z)$ are the two-way attenuated height-dependent transmissions due to molecular extinction and ozone absorption.

The measured 532 nm attenuated backscatter coefficient is calculated as:

$$\beta'_{total}(z) = \beta'_{\parallel}(z) + \beta'_{\perp}(z) = (\beta_p(z) + \beta_m(z)) \cdot T_p^2(z) \cdot T_m^2(z) \cdot T_{O_3}^2(z) \quad (2.10)$$

where $\beta'_{\parallel}(z)$ and $\beta'_{\perp}(z)$ are the parallel and the perpendicular contributions of the attenuated backscatter coefficient, calculated from the measured parallel $P_{\parallel}(z)$ and per-

pendicular $P_{\perp}(z)$ signals at 532 nm using Equation 2.8. β_p is the particular backscatter coefficient.

Ratting the measured attenuated 532 nm backscatter $\beta'_{total}(z)$ and the attenuated clear air backscatter $\beta'_{air}(z)$ coefficient leads to the attenuated scattering ratio $\rho'(z)$:

$$\rho'(z) = \frac{\beta'_{total}(z)}{\beta'_{air}(z)} = \left(1 + \frac{\beta_p(z)}{\beta_m(z)}\right) \cdot T_p^2(z) \quad (2.11)$$

In order to calculate a threshold, a array function of altitude is needed for CALIPSO with lower threshold values for high clear air **Signal-to-Noise Ratio** (SNR) and higher threshold values for low clear air SNR. This measurement for CALIPSO is taken on-board the satellite by computing the **Standard Deviation** (STD) of the signal in regions of 70 to 80 km altitude for every laser pulse, which is equivalent to the **Measured Backscatter Variation** (MBV). With the Poisson distributed backscatter signal, the SNR varies as the square root of the signal. The signal's square root is nothing else than the standard deviation.

$$SNR(z) = \frac{\beta'_{air}(z)}{\sqrt{\beta'_{air}(z)}} = \sqrt{\beta'_{air}(z)} = MBV \quad (2.12)$$

Ergo, the SNR profile relative to the SNR at the maximum sample altitude $z_{max} = 70 - 80$ km is:

$$SNR_{relative} = \frac{\sqrt{\beta'_{air}(z)}}{\sqrt{\beta'_{air}(z_{max})}} \quad (2.13)$$

That leads to **relative backscatter variation** or the relative backscatter deviation (RBV):

$$RBV(z) = \frac{\beta'_{air}(z)}{SNR_{relative}(z)} = \sqrt{\beta'_{air}(z) \cdot \beta'_{air}(z_{max})} \quad (2.14)$$

With the contributions of MBV and RBV in combination with selected constants T_0 and T_1 the threshold array is computed as:

$$\beta'_{threshold}(z) = \beta'_{air}(z) + T_0 \cdot MBV + T_1 \cdot RBV(z) \quad (2.15)$$

where T_0 and T_1 are programmable parameters, based on retrievals using simulated data.

Figures 2.11- 2.13 show measurements of the **Lidar In-space Technology Experiment** (LITE), where a three-wavelength backscatter lidar developed by the NASA Langley Research Center flew onboard a Space Shuttle in September 1994 [Winker et al., 2006] and were used to develop and test the threshold in early CALIPSO mission planning.

Due to different features in the lidar data measured in the atmosphere (Figure 2.11) there would be too many events with $\rho'(z)$ exceeding the single threshold of $\beta'_{air}(z)$. So this threshold gives only a rough impression of the detected aerosol and cloud layers. For the parameterization of the feature shapes, aspect ratios are used:

$$AspectRatio = \frac{PeakAttenuatedScatteringRatio}{FeatureGeometricThickness} \quad (2.16)$$

The aspect ratio, for example, of a dust layer is much lower than the aspect ratio of an alto-cumulus cloud. Therefore, a feature finder is necessary to detect both extremes of the aspect ratio scale.

The minimum feature thickness as a measure of vertical distance in units of length is used in combination with the threshold of $\rho'(z)$ to identify most layers. In order to qualify as a feature now, the scattering ratios in a region must exceed the threshold value for all data points within a vertical extent greater than, or equal to the specified minimum feature thickness.

Once all features are detected, bases and tops will be detected automatically.

After a profile of attenuated scattering ratios is obtained and an array of threshold values is computed, another task of the detection algorithm is to search for the boundary of "clear air" and the top of the next feature. This means that the routine searches the

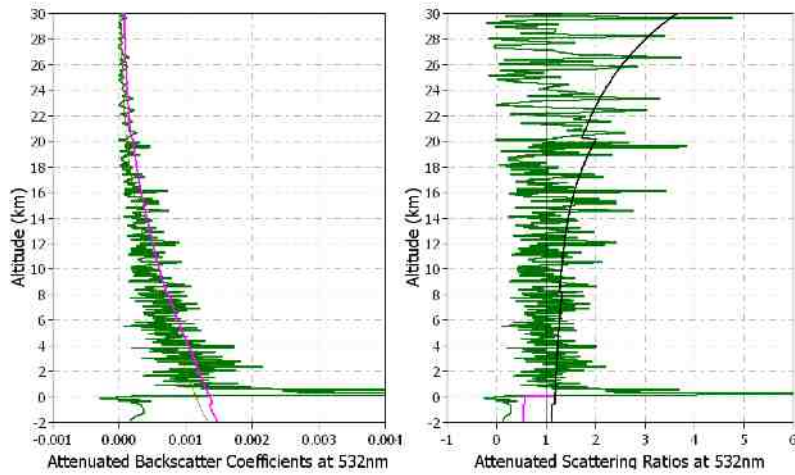


Figure 2.11: Threshold arrays (red and black) for attenuated backscatter coefficients using Equation 2.10 (left), and for attenuated scattering ratios using Equation 2.11 (right), both in green, and derived from LITE data [Vaughan et al., 2004].

whole profile, starting at a selected height and locates a feature top at the first point where the attenuated scattering ratio exceeds the threshold value for the number of consecutive points required to span the feature distance.

An additional feature of the CALIOP aerosol and cloud detection algorithm is the spike threshold factor, which is able to identify very thin, strong clouds, which cause strong peaks in the attenuated backscatter profile.

By definition, the attenuated scattering ratio at the highest cloud top will be greater than 1.00. In theory the feature base is determined at that point, where

- the mean attenuated scattering ratio is less than or equal to the mean attenuated scattering ratio above the feature, and
- the slope of the attenuated scattering ratio is zero.

In practice an algorithm called “probabilistic base locator” is used, which chooses the first point below the threshold as an initial estimate of cloud base for a depth equal to the minimum clear air distance. This estimate of cloud base altitude is continually updated as long as a pre-selected percentage of the points within the examination range

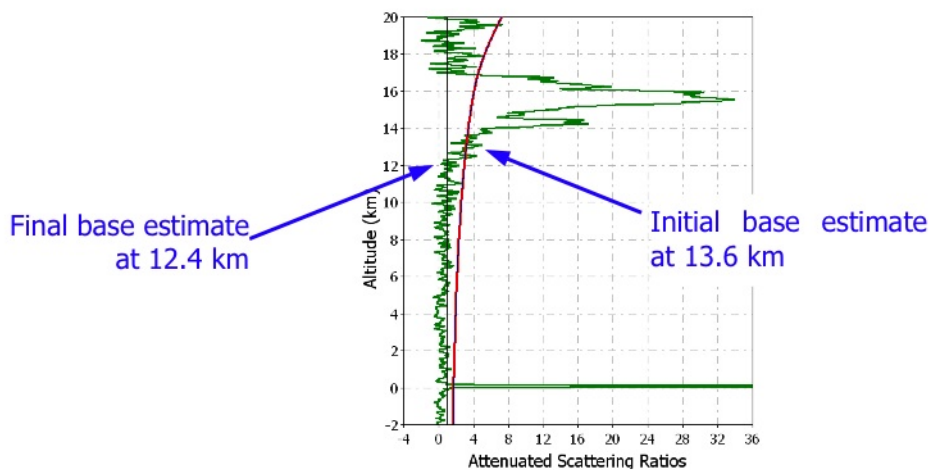


Figure 2.12: Base detection on attenuated scattering ratio in green and the calculated threshold in red [Vaughan et al., 2004].

remains above the threshold value. A semi-final estimate of cloud base is defined at an altitude, where the number of points above the threshold is less than the required percentage (in practice 50% – 70%).

Close to the cloud base the attenuated scattering ratio decreases for some distance. The slope of the attenuated scattering ratio should be negative with respect to the range. Therefore, the value of the scattering ratio stabilizes to some constant value at cloud base and the slope should go to zero. When the slope gets negative, the estimated cloud base is revised to a new, lower altitude. This whole procedure is shown for a cirrus cloud case in Figure 2.12.

After the detection of a feature, the initial threshold has to be updated due to the attenuation of the signal after propagating through a strong feature.

The left panel of Figure 2.13 shows the consequences of a non-rescaled threshold, where the aerosol layer at 1.0 *km* falls entirely beneath the threshold. The right panel demonstrates the results obtained after rescaling the threshold properly. With some assumptions, clearly explained in Vaughan et al. [2004], this update is done in a vertical profile for the first time after the first feature has been detected by first calculating the inte-

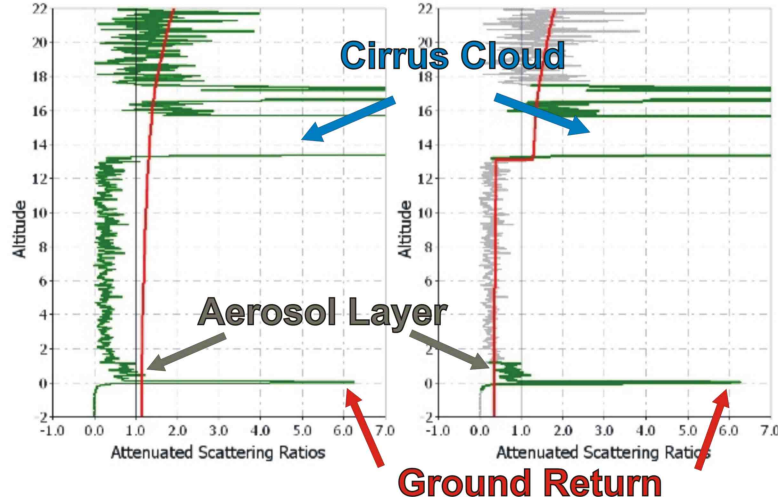


Figure 2.13: Threshold update: Initial threshold (red, left) calculated for the attenuated scattering ratios (green). Attenuated scattering ratios for feature regions (green) and for non-feature regions (gray) with the rescaled threshold (red, right) [Vaughan et al., 2004].

grated attenuated backscatter of the feature $\gamma_{feature}$:

$$\gamma_{feature} = \int_{top}^{base} \beta_p(R) \cdot T_p^2(R) dR \quad (2.17)$$

where $\beta_p(R)$ is the particular backscatter, and $T_p^2(R)$ is the particulate two-way transmittance.

After all features have been identified, a layer description is reported for each feature comprising the base and top altitudes, backscatter coefficients, depolarization ratio, temperatures at the base, top, and mid-feature altitudes. Moreover, solar and geophysical coordinates, surface height, threshold values, and the number of features are recorded for each profile. Once the detected aerosol and cloud layers are described by the properties above, the **Scene Classification Algorithms** can identify each layer with its optical, spatial, and temporal characteristics [Liu et al., 2008]. Aerosols and clouds are discriminated primarily by scattering strength and spectral dependence of

backscattering. The depolarization profile is computed by using the 532 *nm* parallel and perpendicular profiles. Cloud layers then are classified as ice or water, primarily using the depolarization signal and the temperature profile supplied as part of the additional data. Aerosol layers are identified in the same way, using indicators like depolarization, geophysical location, and backscatter intensity.

2.6 Summary

A review of Sections 2.4 and 2.5 shows, that

- both lidar systems, CALIOP and GLAS, use the attenuated backscatter coefficients to detect aerosol and cloud layers. The attenuated backscatter coefficient is calculated applying calibration constants, which are computed by ancillary meteorological data and satellite measurements in high altitudes, where molecular scattering is dominant.
- by only using the attenuated molecular backscatter coefficient as a threshold, the detection sensitivity is lowered due to the strong signal attenuation. This attenuation is due to cloud layers, which, for example, are located above aerosol layers in the lower atmosphere (Figure 2.13). Consequently these aerosol layers can only be detected with a rescaling of the threshold value in consideration of the attenuation evoked by the cirrus layer. The update process is repeated for each detected aerosol and cloud layer.
- after detecting all aerosol and cloud layers in the atmosphere, a layer discrimination takes place. In both cases this routine distinguishes aerosols, clouds, and even the planetary boundary layer. The discrimination of aerosols and clouds is done taking into account the different scattering strengths and the magnitude of the resulting height-dependent gradient of the attenuated backscatter coefficients in case of attenuation by an aerosol or cloud layer.

Chapter 3

Cloud Detection with the ALADIN Airborne Demonstrator

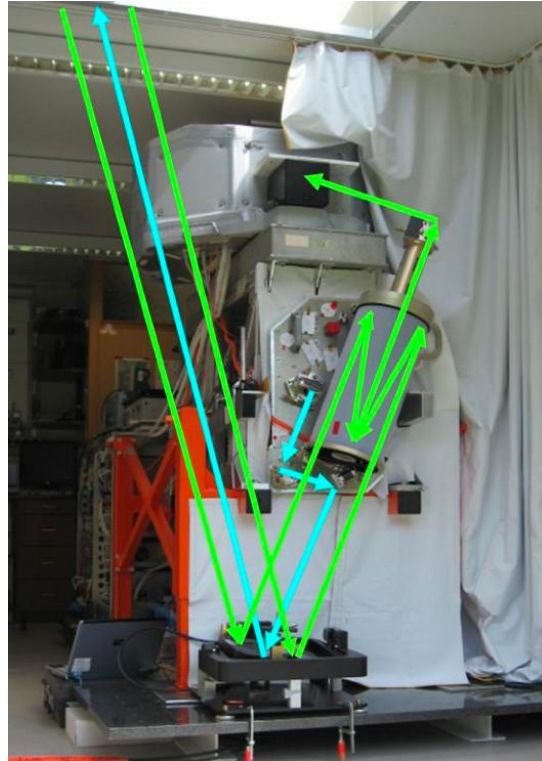
Within the pre-development program of ADM-Aeolus a prototype of the ALADIN instrument, including the transmitter, receiver, and telescope was developed [Durand et al., 2005, 2006, Reitebuch et al., 2008]. With this prototype, the **ALADIN Airborne Demonstrator** (A2D), scientific and technological challenges of the ADM-Aeolus program are investigated during airborne and ground campaigns performed by **Deutsches Zentrum für Luft- und Raumfahrt** (DLR), Oberpfaffenhofen.

3.1 ALADIN Airborne Demonstrator - A2D

3.1.1 Transmitter

According to the plans of the spaceborne transmitter, a Neodymium-doped Yttrium Aluminium Garnet (Nd:YAG) laser is used. The fundamental wavelength of 1064 *nm* (infrared) is converted by harmonic sections first to 532 *nm* (green) and finally to 355 *nm* (ultraviolet), which is then transmitted into the atmosphere with an output energy of 60-70 *mJ* and a pulse repetition rate of 50 *Hz* [Witschas, 2007]. This specific output energy, compared to 120 *mJ* for the satellite instrument, was chosen, taking into account the lower flight altitude of the DLR Falcon aircraft and the lower telescope

Figure 3.1: The A2D installed in the ground container from the front with the A2D telescope; indicated are the transmit (blue) and the receive path (green) via ground mirror for 20° off zenith pointing out off the container roof [Reitebuch et al., 2008].



diameter in order to maintain the expected levels of signal on the receiver [Durand et al., 2005].

Onboard the spacecraft, the burst mode was selected due to electrical power limitations, which is not necessary for the airborne demonstrator. The burst mode allows the laser to be switched on for 7 s (corresponding to about 50 km observation length), and to keep it switched off during the remainder of the 28 s repeat cycle (corresponding to a total ground track of 200 km). The laser design and performance is described in more detail in Witschas [2007] and Schröder et al. [2007]. For ground-based measurements, the airborne prototype A2D is set up in a container pointing vertically or with off-zenith angles up to 20° through an opening in the container roof (Figure 3.1) by use of a ground mirror.

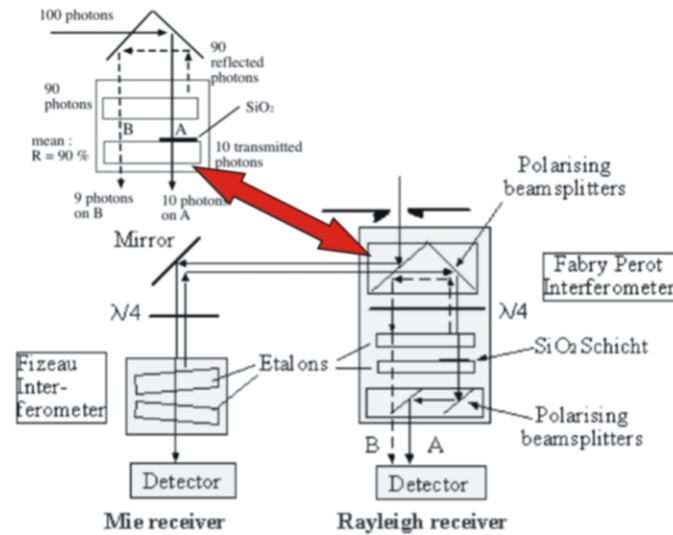


Figure 3.2: Schematic figure of the A2D receiver. Principle of the double sequential Fabry-Perot interferometer with an example of photons at channel A and B [Paffrath, 2006].

3.1.2 Telescope

The A2D telescope uses a Cassegrain configuration of a 200 *mm* primary mirror, while ADM-Aeolus uses a 1500 *mm* diameter telescope. It is slanted at an angle of only 20° in the aircraft, compared to 35° on the satellite, due to the limited space available on the DLR Falcon aircraft. Another difference is the separation of the transmit and the receive beam (Figure 3.1) instead of a transceiver telescope for the satellite.

3.1.3 Receiver

The main constituents of the A2D-receiver are based on the refurbished **Pre-Development Model** (PDM) of the lidar receiver as a part of the ALADIN instrument (Figure 3.2). The design of the receiver PDM is similar to the spacecraft in terms

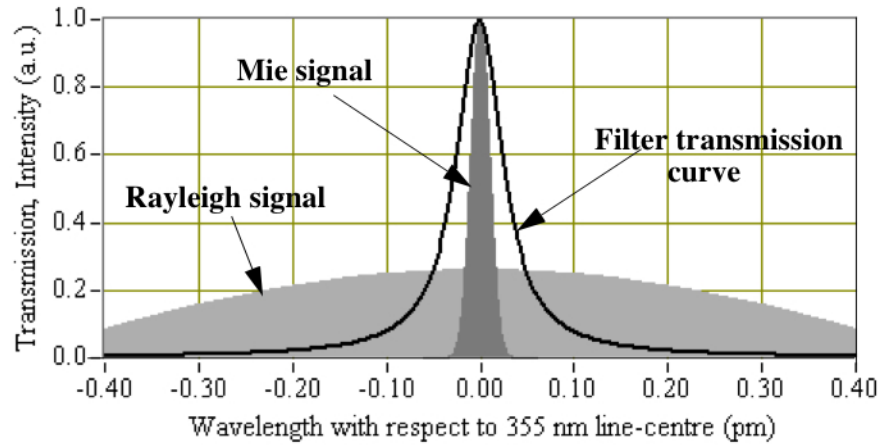


Figure 3.3: The transmission curve of the Fizeau interferometer and the intensity distribution of the Mie and Rayleigh signal from a 355 nm source versus wavelength [Paffrath, 2006].

of optical and mechanical design, except for some changes in the front optics. The background light is attenuated by the front optics where the backscatter signal passes through an interference filter and is rotated into vertical polarized light. The signal is then reflected off the polarizing beamsplitter into the Mie receiver. Figure 3.3 shows the typical shape of the transmission curve of the Fizeau interferometer. The Mie return is transmitted through the Fizeau interferometer onto the **Accumulation Charge-Coupled Device (ACCD)** and provides a linear fringe [Paffrath, 2006].

About 90% of the broad Rayleigh spectrum is reflected from the Fizeau interferometer. The signal is then directed towards the Rayleigh receiver and is still influenced by a small amount of the Mie spectrum, which make a cloud detection possible even on the Rayleigh channel.

In the Double Edge Fabry-Perot interferometer the beam is split into two zones, which is done by routing the input beam to the sides of the Rayleigh detector unit to two sides of a sequential Fabry-Perot interferometer (Figure 3.2). The sides of the interferometer differ in spacing due to a thin vacuum-deposited SiO_2 layer.

So, in presence of wind speed the Rayleigh spectrum is shifted towards one of the filter curves, resulting in two different intensities of the two signals passed to the Rayleigh

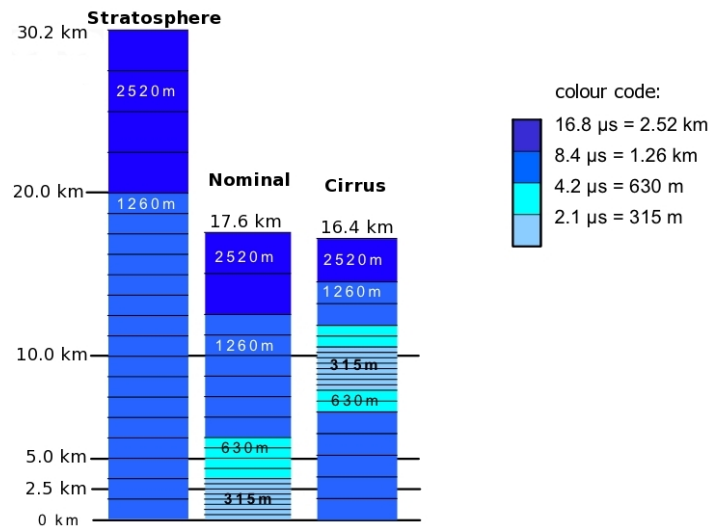


Figure 3.4: Vertical sampling modes “Stratosphere”, “Nominal”, and “Cirrus” during the 2nd ALADIN Ground Campaign with different range gate resolutions of 315 *m*, 630 *m*, 1260 *m*, and 2520 *m* [Paffrath et al., 2008].

ACCD are shifted toward one of the two channels, called A and B.

The ACCD allows to measure with different integration times for each range bin with a minimum of 2.1 μs corresponding to 315 *m* range (Figure 3.4). The A2D is operated from the ground mainly in three modes:

The “Stratosphere” mode, where the backscattered signal is measured up to a height of 30 *km*, the “Cirrus” mode, where a maximum resolution of 315 *m* is achieved at an altitude of 7.5 to 10.1 *km*, and the “Nominal” mode, where the resolution decreases with increasing measurement altitude. The last two modes are used for the intercomparison at Section 4.2.

Beside the vertical resolution, two levels of temporal resolution are selectable, called observation and measurement level. The number of laser pulses P accumulated on the ACCD per measurement is set to a value of 20, which is adequate to around 1.5 *km*

ground track of the satellite system. The number of measurements per observation N can be set either to $N = 1$, or to $N = 35$, which is comparable to a 50 *km* ground track of the satellite. So, the summarized total number T of the accumulated laser pulses on the ACCD is:

$$T = N \cdot (P - 2) \tag{3.1}$$

P is subtracted by 2 laser pulses due to the time needed to read out the ACCDs. For the observation level ($N = 35$) the number of laser pulses summarized for this detection level is 630, while it is 18 for the measurement level ($N = 1$).

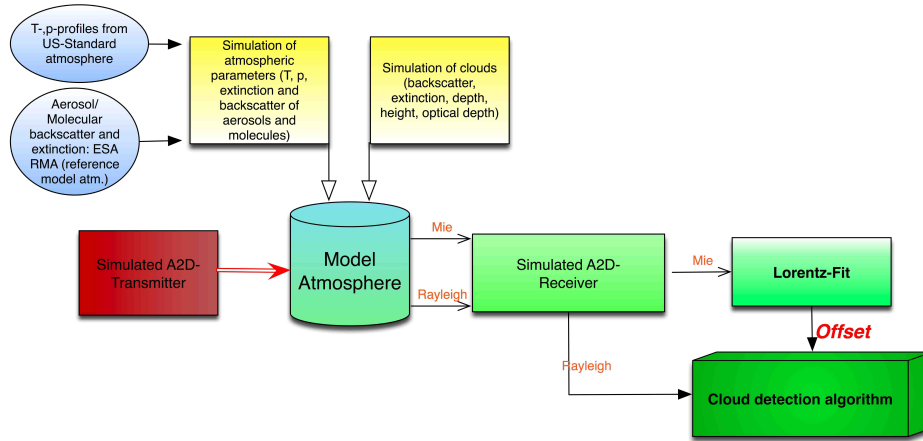


Figure 3.5: Conception of the A2D-Simulator.

3.2 A2D - Simulator

The A2D-Simulator was developed as a representative end-to-end simulator of both, the ALADIN Airborne Demonstrator and the modeled backscattering atmosphere by Paffrath [2006]. It is used to investigate the performance of a simulated A2D under various conditions.

In Figure 3.5, a rough flowchart of the simulator and the calculated signals passed to the cloud detection routine is shown. Beside the atmosphere and the cloud simulation, which will be explained below, there are simulations of the laser, the receiver, and the telescope. The number of photons emitted by the laser at a wavelength λ are calculated from the energy per photon $h \cdot \frac{c}{\lambda}$ and the laser pulse energy E :

$$N_{ph} = \frac{\lambda}{h \cdot c} E \quad (3.2)$$

where h is the Planck's constant ($6.625 \cdot 10^{-34} Js$).

The received number of photons $N_{ph}(\lambda, R)$ can be calculated with the lidar equation

[Measures, 1991]:

$$N_{ph}(\lambda, R) = \frac{\lambda}{h \cdot c} E \cdot \frac{\Delta R \cdot A_0}{R^2} \cdot k(\lambda) \cdot \beta(R) \cdot T^2(R) \quad (3.3)$$

where R is the range from the lidar, E the energy of the transmitted pulse, λ the wavelength of the transmitted pulse, and $\beta(R)$ the atmospheric backscatter coefficient. $\frac{A_0}{R^2}$ is the acceptance solid angle of the receiving optics with A_0 being the collecting area of the telescope. The instrument constant $k(\lambda)$ considers the response of the receiver like the spectral transmission. Other very important parts of the lidar equation are the atmospheric two-way transmission T^2 and the range resolution ΔR .

The telescope collects the backscattered photons that are attenuated by the transmission of the transmitter τ_T and receiver optics τ_R of the front optic modules, including the telescope, mirrors, and all other elements of the receiver unit. For the detection of the backscattered signal, two **Accumulation Charge-Coupled Devices** (ACCD) are used as detectors, one for the Mie and one for the Rayleigh channel. The Mie receiver uses the fringe imaging technique to determine the Doppler shift of the atmospheric backscatter signal, while the Rayleigh receiver uses the double edge technique (more details can be found in [Paffrath, 2006]).

In Sections 2.4 and 2.5 it is shown, that the cloud detection of both lidar instruments - GLAS and CALIOP - is based on profiles of the **Signal-to-Noise Ratio** (SNR). So, the simulator has to calculate the mean number of backscatter photons N_{Ph} (Equation 3.2 and 3.3) as well as the noise. In case of a shot noise detection unit, as for A2D and ALADIN, this noise is the variation of the calculated number of photons according to a Poisson distribution with a standard deviation of $\sigma_N = \sqrt{N_{Ph}}$.

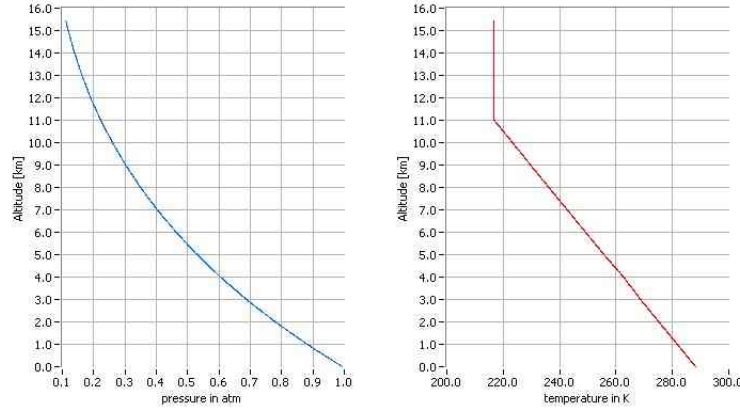


Figure 3.6: Profiles from ESA-RMA: Temperature in Kelvin (left) and Pressure in atm (right), 1 atm = 1013.25 hPa.

3.2.1 Atmosphere

Atmospheric profiles for temperature and pressure are used from the U.S. Standard Atmosphere, while backscatter and extinction are used from the **Reference Model Atmosphere** (RMA) developed by the **European Space Agency** (ESA), which was derived using backscatter climatologies at $10.6 \mu\text{m}$ [Vaughan et al., 1995].

Molecular backscatter and extinction

The RMA uses the U.S. Standard Atmosphere with defined pressures and temperatures, as depicted in Figure 3.6, and is simulated in steps of 15 m up to 15435 m altitude. Both profiles are necessary to calculate the molecular backscatter coefficient:

$$\beta_{Mol}(z) = N_{Mol}(z) \cdot \sigma_{Mol} \quad (3.4)$$

where N_{Mol} is the number of molecules per volume and σ_{Mol} is the molecular Rayleigh backscattering cross section per molecule.

The changes of the number of molecules with height $N_{Mol}(z)$ can be described as:

$$N_{Mol}(z) = \left[\frac{296 \text{ K}}{T(z)} \right] \left[\frac{p(z)}{1013 \text{ hPa}} \right] \cdot N_L(z) \quad (3.5)$$

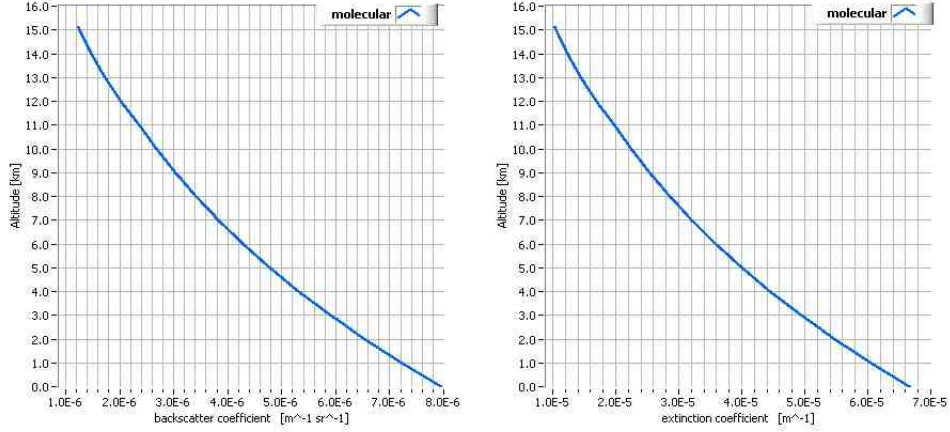


Figure 3.7: The molecular backscatter β_{Mol} (left) and extinction α_{Mol} (right) coefficient depending on altitude resulting from the U.S. Standard Atmosphere temperature and pressure profile in respect to a wavelength of $0.355 \mu m$.

where $T(z)$ is the temperature in $[K]$ and $p(z)$ is the pressure in $[hPa]$ at an altitude z . $N_L(z)$ is the Loschmidt's number, which is $N_L = 2.4791019 \cdot 10^{25} [m^{-3}]$ at $T = 296 K$ and $p = 1013 hPa$.

The molecular Rayleigh backscattering cross section σ_{Mol} was determined by Collins and Russell (1976) cited in Measures [1991]:

$$\sigma_{Mol} = \left[\frac{0.55}{\lambda[\mu m]} \right]^4 \cdot 5.45 \cdot 10^{-28} \text{ in } [cm^2 sr^{-1}] \quad (3.6)$$

In the A2D-Simulator, β_{Mol} is simulated for the ALADIN wavelength of $0.355 \mu m$ using the U.S. Standard Atmosphere temperature and pressure profiles (Figure 3.7).

The molecular extinction coefficient α_{Mol} can be calculated as [Measures, 1991]:

$$\alpha_{Mol} = S_{Mol} \cdot \beta_{Mol} \quad (3.7)$$

where β_{Mol} is the molecular backscatter coefficient, and $S_{Mol} = \frac{8\pi}{3} sr$ is the molecular lidar ratio.

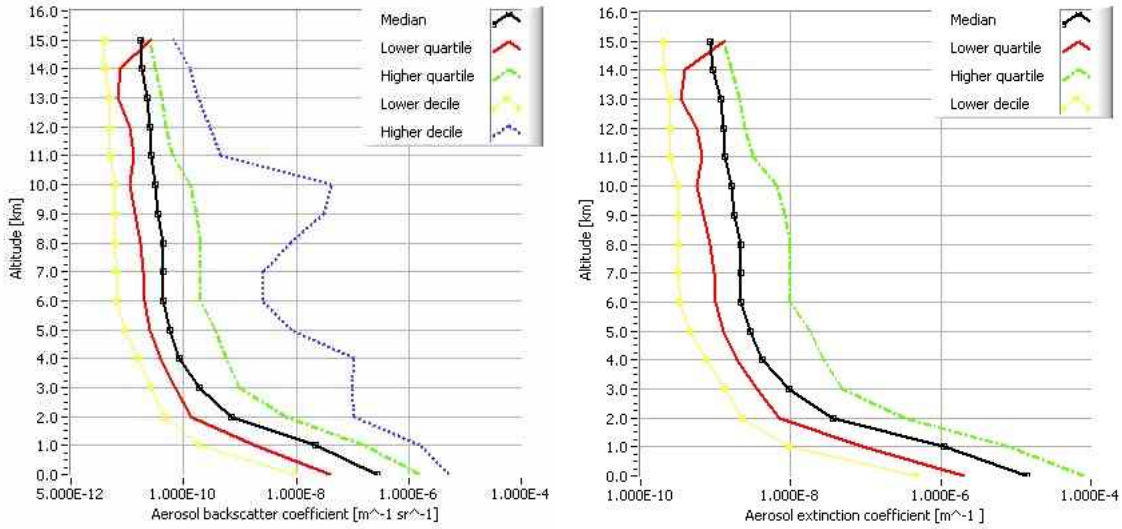


Figure 3.8: RMA-Profiles for the aerosol backscatter β_A (left) and the aerosol extinction α_A (right) at a wavelength of $0.355 \mu\text{m}$.

Aerosol backscatter and extinction

In addition to the molecular backscatter coefficient, another important parameter of the atmosphere, the aerosol backscatter, has to be simulated. The aerosol backscatter coefficients are part of the ESA RMA database and were measured at a wavelength of $10.6 \mu\text{m}$, and scaled to $0.355 \mu\text{m}$ by a conversion law [Vaughan et al., 1998].

As depicted in Figure 3.8, several aerosol cases are simulated. The definitions of “Higher Decile”, “Lower Decile”, “Higher Quartile”, “Lower Quartile”, and “Median” are used. The aerosol backscatter coefficient decreases for all five cases above the boundary layer, while near-ground aerosols are found in high concentrations. The profile of the higher decile model illustrates the effects of high aerosol concentration up to 4 km and of thin and transparent clouds at 10 km . The percentiles are those values of backscatter at which a given percentage of the data is greater or less than this values. Thus, the higher/lower quartiles have 25 % of data greater/less than, while the higher/lower deciles have 10 % of data greater/less than.

In the following simulations, only the “Median” model is used, where half of the mea-

Types of Clouds	Backscatter Coefficient	Extinction Coefficient	Lidar Ratio	Altitude
	$\beta_{Cloud} [m^{-1}sr^{-1}]$	$\alpha_{Cloud} [m^{-1}]$	S_{Cloud}	$[m]$
Stratus	$5.0 \cdot 10^{-3}$	$9.0 \cdot 10^{-2}$	18.0	200 – 700
FW Cumulus	$6.0 \cdot 10^{-4}$	$1.2 \cdot 10^{-2}$	20.0	750 – 1000
Cumulonimbus	$1.0 \cdot 10^{-2}$	$1.8 \cdot 10^{-1}$	18.0	2000 – 4000
Altostratus	$1.0 \cdot 10^{-3}$	$1.8 \cdot 10^{-2}$	18.0	4000 – 4500
Cirrus	$1.6 \cdot 10^{-5}$	$2.0 \cdot 10^{-4}$	12.5	8500 – 9500

Table 3.1: Backscatter and extinction coefficient depending on cloud types, designed in the ESA RMA [Vaughan et al., 1998].

sured data are greater respectively smaller than the median value. This “Median” profile agrees, according to Paffrath [2006] within an order of magnitude with the **European Aerosol Research Lidar Network** (EARLINET) set up to establish an aerosol climatology, [Bösenberg and Matthias, 2003]).

With the known aerosol backscatter coefficients, the calculation of the aerosol extinction coefficients (Figure 3.8) follows as [Weitkamp, 2005]:

$$\alpha_A = \beta_A \cdot S_A \quad (3.8)$$

where α_A is the aerosol extinction coefficient, β_A is the aerosol backscatter coefficient. For the lidar ratio S_A a value of 50 *sr* is chosen for the simulations, which is a typical value for continental sites [Wandinger et al., 2008], despite the fact, that the lidar ratio can vary from 20 – 80 *sr* for aerosols and clouds.

3.2.2 Clouds

Originally, the simulator could simulate five cloud types with fixed boundaries (Table 3.1). These fixed boundaries are fairly inflexible in order to simulate realistic clouds, because the aim of this work is the detection of different cloud types at different heights with, for example, changing altitude, optical thickness, or physical thickness. In Figure 3.9 the different possibilities of the simulator to change parameters per observation

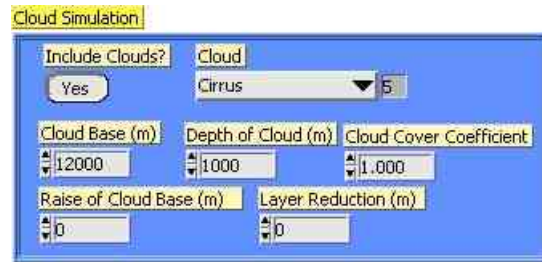


Figure 3.9: Graphical user interface of the cloud simulator.

(630 laser pulses) and per measurement (18 laser pulses) is shown:

- like in the original atmospheric simulation, it is possible to “switch” clouds on or off, and the cloud type to be simulated can be chosen out of the five defined cloud types from Table 3.1,
- the “cloud base” altitude and the “depth of cloud”, both in units of meters, can be chosen,
- the “cloud cover coefficient” influences backscatter and extinction of the cloud by multiplying it with a constant value (in order to raise or lower the cloud optical depth)
- in order to lower the “physical thickness” the “layer reduction” lowers the layer depth starting at the cloud top until the cloud disappears,
- the “raise of the cloud base” increases the cloud base and top altitude in units of meters.

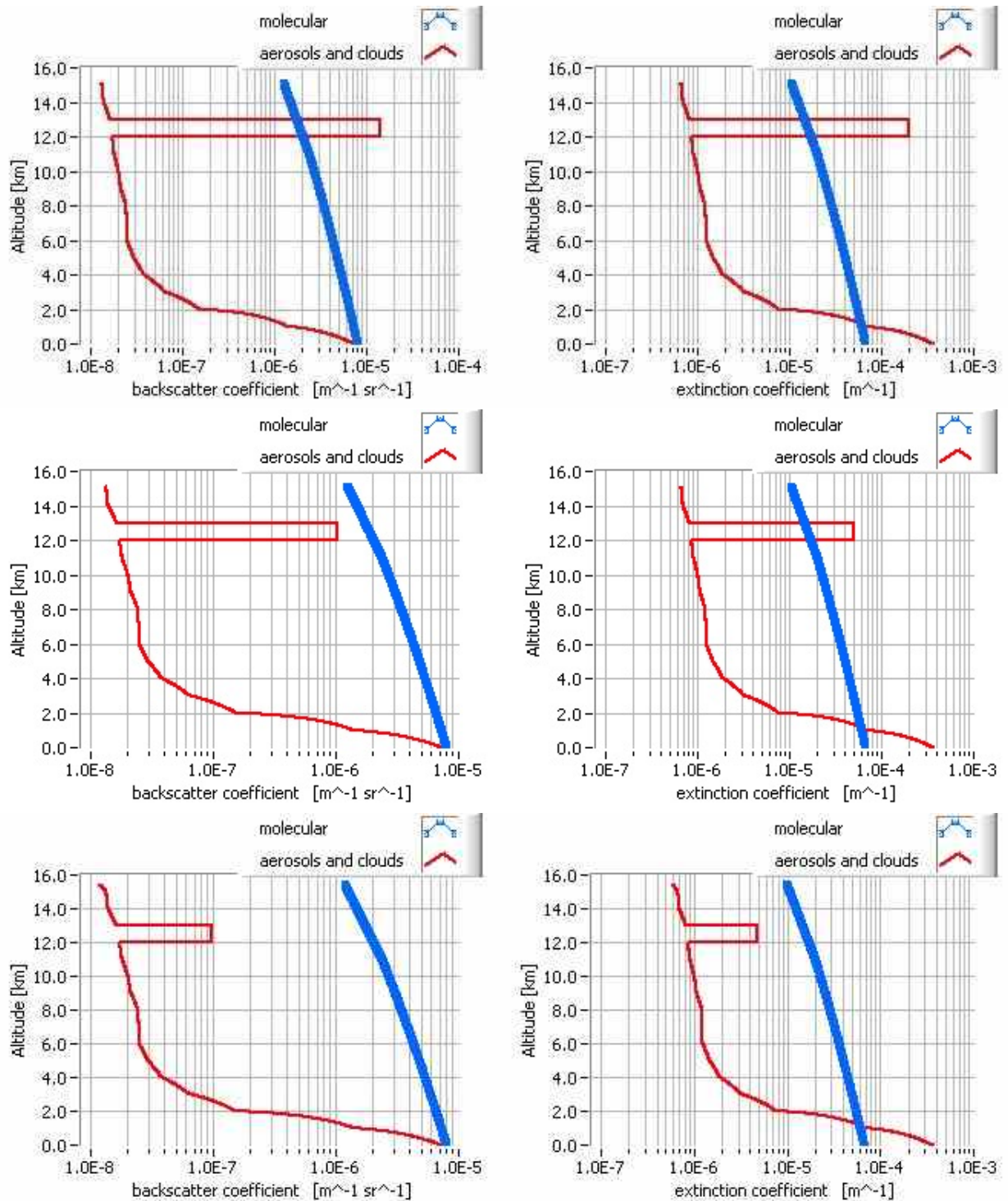


Figure 3.10: Simulated cirrus cloud with a cloud base at 12 km and its top at 13 km altitude with different cloud optical depths (COD) of $2.0 \cdot 10^{-1}$ (top), $5.0 \cdot 10^{-2}$ (middle), and $5.0 \cdot 10^{-3}$ (bottom).

The influence of the cloud simulator on the atmospheric backscatter is shown in Figure 3.10. Beside the molecular backscatter and extinction coefficients, the coefficients of aerosols and clouds are plotted as well. Clouds with different backscatter and extinction have different optical properties, which can be described by the **Cloud Optical Depth** (COD) τ [Weitkamp, 2005]:

$$\tau = \int_{z_1}^{z_2} \alpha_{Cloud} dz \quad (3.9)$$

where z_2 is the altitude of the cloud top and z_1 the altitude of the cloud base. In case of constant extinction coefficients, Equation 3.9 can be simplified to:

$$\tau = (z_2 - z_1) \cdot \alpha_{Cloud} \quad (3.10)$$

Figure 3.10 shows a cirrus clouds with a cloud base at an altitude of 12 *km* and a cloud top at 13 *km*. The backscatter and the extinction coefficient are reduced for every plot (top to bottom). The first case with an extinction of $\alpha_{Cloud} = 2.0 \cdot 10^{-4}$ has a COD of $\tau = 2.0 \cdot 10^{-1}$, while the second plot represents a subvisible cirrus cloud with an extinction of $\alpha_{Cloud} = 5.0 \cdot 10^{-5}$ resulting in a COD of $\tau = 5.0 \cdot 10^{-2}$. Subvisible cirrus cloud have a cloud optical depth between $3.0 - 5.0 \cdot 10^{-2}$ [Kärcher, 2002]. For a determination of the minimum detectable cloud optical depth the simulated cirrus with an extinction coefficient of $2.0 \cdot 10^{-4}$ provides the potential to retrieve clouds with low cloud optical depths. Thus, the last case shows, a cirrus cloud with an extinction $\alpha_{Cirrus} = 5.0 \cdot 10^{-6}$ resulting in a COD of $\tau = 5.0 \cdot 10^{-3}$. The other cloud types like stratus, cumulus, cumulonimbus, and altostratus (Table 3.1) have very high backscatter and extinction coefficients, which are not favourable to these determinations.

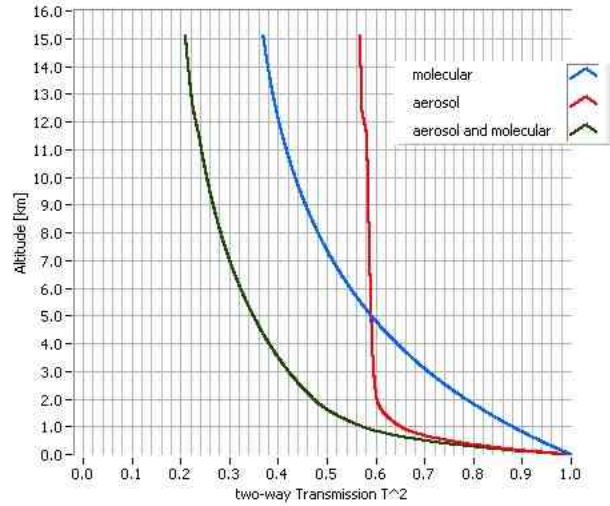


Figure 3.11: Two-way Transmission calculated for molecular (blue), aerosol (red, Median model), and summarized (green) extinction coefficients.

3.2.3 Transmission

The molecular, aerosol, and cloud extinction coefficients are used to calculate the transmission of the atmosphere. The two-way transmission $T_{A,Mol}^2(\lambda, z)$ is defined as [Measures, 1991]:

$$T_{A,Mol}^2(\lambda, z) = e^{-2 \int_0^z (\alpha_A(z) + \alpha_{Mol}(z)) dz} \quad (3.11)$$

α_{Mol} is the extinction coefficient for molecular backscatter, α_A for aerosol and cloud backscatter.

Figure 3.11 shows the strong decrease of the aerosol transmission in the boundary layer, while it gets almost constant above. The molecular transmission is decreasing over the whole altitude range.

For first tests on the cloud detection algorithms, which will be explained in the following, the simulated clouds are sufficient even though they are not realistic (especially the ability to simulate only one cloud layer).

3.3 Cloud Detection from Mie Spectrometer

In case of the Mie ACCD the collected photons arise from Mie and Rayleigh scattering in the atmosphere (Figure 3.3), so both signals have to be separated.

In order to segregate both scattering processes on the ACCD a so-called offset has to be calculated. The offset is composed mainly by the Rayleigh signal and by only a small part of solar background signal. This offset leads to the computing of the Signal-to-Noise Ratio and the Scattering Ratio, which will be used for the cloud detection in the following chapters.

3.3.1 Signal-to-Noise Ratio

For both, the Fabry-Perot and the Fizeau interferometer, the Lorentz function was used to model the filter function, which is an adequate approximation of the filter function [Paffrath, 2006, p.23]. The signal on the Mie ACCD $P(i, j, k)$ is calculated for every altitude layer (range bin) i (Figure 3.12). With the $j = 16$ pixels on the ACCD (pixel 0 – 15) the received signal can be written as $\sum_0^{15} P(i, j, k)$, where k represents the temporal integration (observation-/measurement-level).

Offset

So, to calculate the offset for the Mie received signal as a border of the Mie and the Rayleigh backscatter signal, the Lorentz function $L(j)$ can be written for every pixel j as [Streicher et al., 2006]:

$$L(j) = \frac{a \cdot FWHM^2}{4 \left[(j - j_0)^2 + \frac{FWHM^2}{4} \right]} + C \quad (3.12)$$

where j_0 is the position of the peak value in number of pixels, $FWHM$ is the **Full-Width-Half-Maximum** (FWHM), the height a , and the offset C (Figure 3.12).

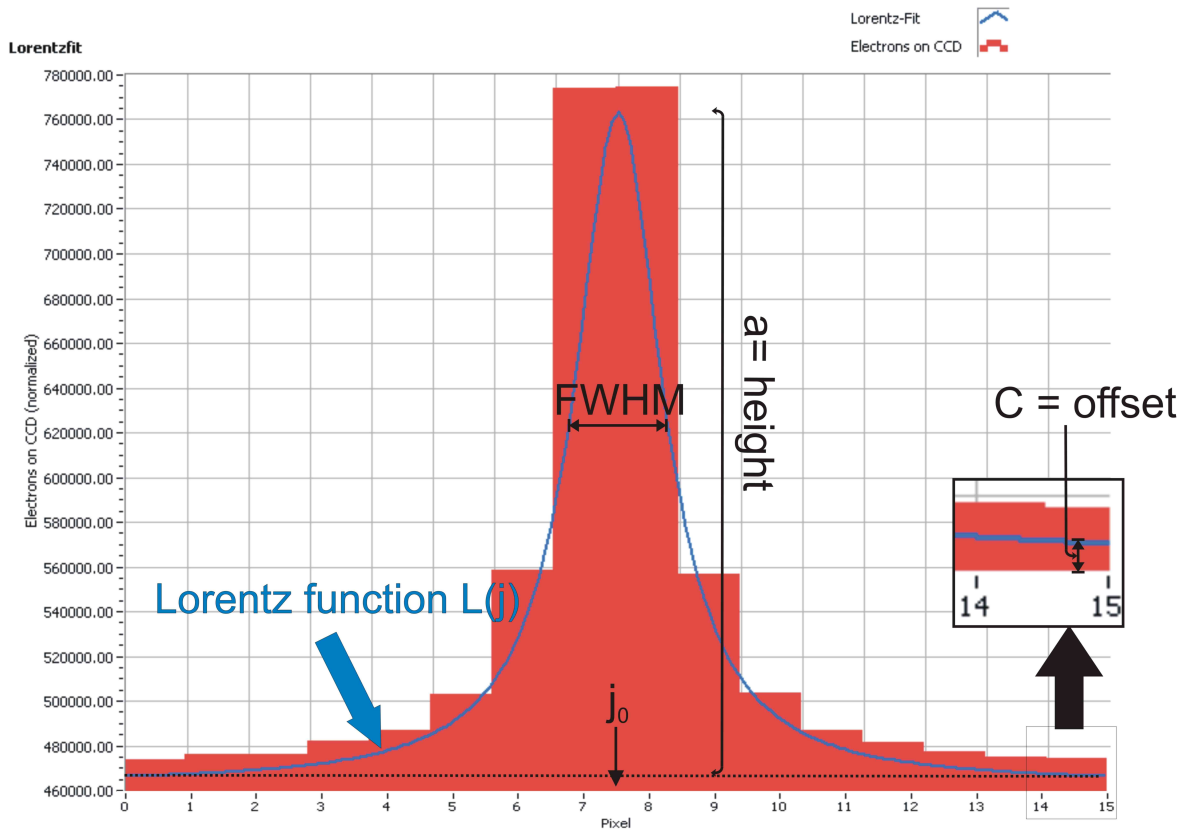


Figure 3.12: Detected signal on the Mie ACCD with the schematic variables of the Lorentz function calculation.

The Lorentz function $L(j)$ is now used to calculate the offset and the height of the Mie signal for 16 pixels by the Cholesky method according to [Bronstein et al., 2001, p.916]:

$$\begin{pmatrix} \sum L(j)^2 & \sum L(j) \\ \sum L(j) & 16 \end{pmatrix} \cdot X = \begin{pmatrix} \sum_{j=0}^{15} (P(i, j, k) \cdot L(j)) \\ \sum_{j=0}^{15} P(i, j, k) \end{pmatrix} \quad (3.13)$$

where $L(j)$ is the Lorentz function from Equation 3.12 and $\sum_{j=0}^{15} P(i, j, k)$ is the total received signal (with the index $i := \text{layer}$, $j := \text{pixel}$, $k := \text{measurement}$).

X is a one-dimensional array consisting of height a , which is the amplitude of the lidar signal minus the offset C :

$$X = \begin{pmatrix} a \\ C \end{pmatrix} \quad (3.14)$$

Offset C and height a can be explicitly expressed by solving the linear equation with:

$$C = \frac{\sum_{j=0}^{15} P(i, j, k) - \sum_{j=0}^{15} L(j) \cdot a}{16} \quad (3.15)$$

where the height a is defined by:

$$a = \frac{\sum_{j=0}^{15} (P(i, j, k) \cdot L(j) - \sum_{j=0}^{15} (L(j) \cdot C))}{\sum_{j=0}^{15} L(j)^2} \quad (3.16)$$

Signal-to-Noise Ratio

With the offset (Equation 3.15) the Signal-to-Noise Ratio $SNR(i, k)$ can be calculated with the sum of the received signal $\sum_{j=0}^{15} P(i, j, k)$. In order to compute the pure Mie backscatter signal, the received Rayleigh backscatter on the Mie ACCD has to be subtracted from the received signal. This is done by using the calculated offset and

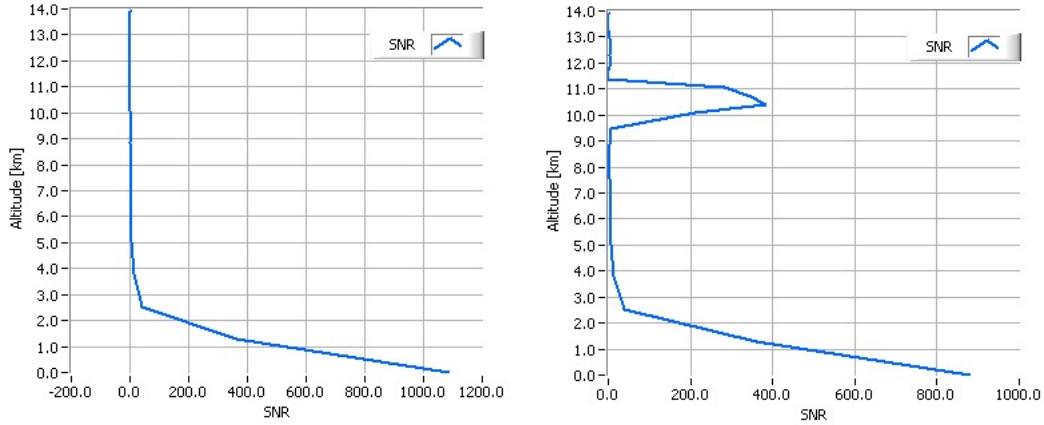


Figure 3.13: Mie SNR of clear atmosphere (left) and an atmosphere with a simulated cirrus cloud at 10 km (right) with a geometric depth of 1 km and a cloud optical depth of 0.2; U.S. Standard Atmosphere simulated with the Median aerosol model.

multiplying with the number of $j = 16$ pixels. The noise, as introduced in Section 3.2, is Poisson distributed, and can be written as $\sqrt{\sum_{j=0}^{15} P(i, j, k)}$. So, the Signal-to-Noise Ratio $SNR(i, k)$ can be calculated as:

$$SNR(i, k) = \frac{\sum_{j=0}^{15} P(i, j, k) - 16 \cdot C}{\sqrt{\sum_{j=0}^{15} P(i, j, k)}} \quad (3.17)$$

According to Equation 3.17, the SNR for an atmospheric simulation including a cirrus cloud with a cloud base altitude of 10 km and a cloud top at 11 km is depicted in Figure 3.13. Here and in the following the “Median” aerosol model is used in combination with the U.S. Standard definition for pressure, temperature, and molecules for atmospheric simulations. The Mie Signal-to-Noise Ratio increases rapidly to values of 350 when the photons are backscattered from a cloud and decreases fast in the clear atmosphere above (right, Figure 3.13), while it is close to zero (values around 5 – 15) in a clear atmosphere above 5 km (left, Figure 3.13).

3.3.2 Scattering Ratio

Another possible method for a cloud detection parameter is the unattenuated scattering ratio ρ , which is according to Measures [1991, p.344]:

$$\rho = \frac{\beta_A + \beta_{Mol}}{\beta_{Mol}} = 1 + \frac{\beta_A}{\beta_{Mol}} \quad (3.18)$$

where β_A is the backscatter coefficient caused by Mie (aerosol and cloud) scattering while β_{Mol} is caused by Rayleigh (molecular) scattering.

As introduced by Measures [1991, p.357]

$$\rho \approx \frac{E_{Mie} + E_{Rayleigh}}{E_{Rayleigh}} = 1 + \frac{E_{Mie}}{E_{Rayleigh}} \quad (3.19)$$

where E_{Mie} is the signal backscattered by Mie scattering and $E_{Rayleigh}$ is backscattered by Rayleigh scattering.

As calculated in Secton 3.3.1 the Mie signal on the Mie spectrometer E_{Mie} can be written as:

$$E_{Mie} = \sum_{j=0}^{15} (P(i, j, k) - C) = \sum_{j=0}^{15} P(i, j, k) - 16 \cdot C \quad (3.20)$$

The Rayleigh signal on the Mie spectrometer $E_{Rayleigh}$ is:

$$E_{Rayleigh} = \alpha_{Correction} \cdot 16 \cdot C \quad (3.21)$$

where $\alpha_{Correction}$ is a determined correction factor due to the small aperture of Rayleigh signal visible on the Mie ACCD [Streicher et al., 2006].

This leads to the Scattering Ratio ρ for A2D:

$$\rho = 1 + \frac{\sum_{j=0}^{15} P(i, j, k) - 16 \cdot C}{\alpha_{Correction} \cdot 16 \cdot C} \quad (3.22)$$

$$\rho = 1 + \left[\frac{\sum_{j=0}^{15} P(i, j, k)}{\alpha_{Correction} \cdot 16 \cdot C} - \frac{1}{\alpha_{Correction}} \right] \quad (3.23)$$

$$\rho = 1 + \frac{1}{\alpha_{Correction}} \left[\frac{\sum_{j=0}^{15} P(i, j, k)}{16 \cdot C} - 1 \right] \quad (3.24)$$

$$\Rightarrow \rho = 1 + \alpha_{CorrBackScatterRatio} \left[\frac{1}{16} \frac{\sum_{j=0}^{15} P(i, j, k)}{C} - 1 \right] \quad (3.25)$$

where $\alpha_{CorrBackScatterRatio} = \frac{1}{\alpha_{Correction}} < 1$.

For A2D the offset C (Equation 3.15) can be approximated as:

$$C \approx \frac{1}{4} \sum_{m=1}^4 LIDasc \quad (3.26)$$

where $\frac{1}{4} \sum_{m=1}^4 LIDasc$ is the average of the four pixel on the Mie CCD with the lowest amount of backscattered photons.

This approximation is valid for low scattering ratios, while it leads to an underestimation at high scattering ratios [Streicher et al., 2006], which is not relevant for a general cloud detection. So, the scattering ratio can be calculated as [Streicher et al., 2006]:

$$\rho(i, k) = 1 + \alpha_{CorrBackScatterRatio} \left[\frac{4}{16} \frac{\sum_{j=0}^{15} P(i, j, k)}{\sum_{m=1}^4 LIDasc(i, m, k)} - 1 \right] \quad (3.27)$$

where the factor $\alpha'_{CorrBackScatterRatio}$ was determined as 0.8 [Streicher et al., 2006].

The vertical profile of the computed scattering ratio in Figure 3.14 is easily explained: In a clear atmosphere the scattering ratio is close to 1.0, while it exceeds a chosen

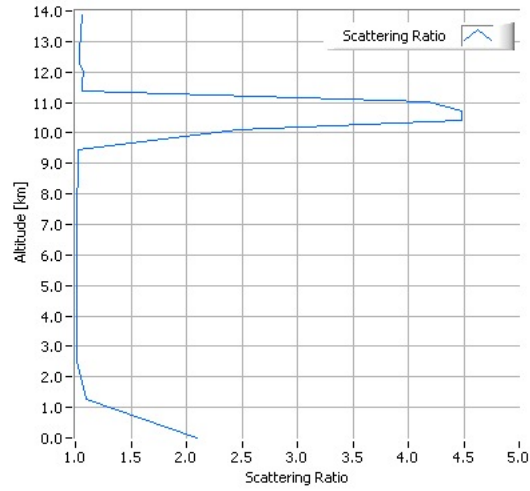


Figure 3.14: Calculated scattering ratio of a cirrus cloud in 10 km altitude with a depth of 1 km and cloud optical depth of 0.2; the true Scattering Ratio $\frac{\beta_A + \beta_{Mol}}{\beta_{Mol}}$ would be 6.7.

threshold of $\rho(i, k) = 1.3$ up to a maximum of almost 5.0 for a simulated cirrus cloud. The true scattering ratio calculated as $\rho_{True} = \frac{\beta_A + \beta_{Mol}}{\beta_{Mol}}$ would result in a slightly higher value of 6.7, which is caused by the Mie signal loss due to the approximations (Equation 3.26) done for A2D.

3.3.3 Detection Algorithm

The simulator forms the basis for this thesis on cloud detection from real data. Since it allows the testing of different thresholds and detection methods, the simulator is suited to develop a cloud detection algorithm using the Signal-to-Noise Ratio (SNR).

According to Figure 3.13 the SNR of the Mie channel is slightly height-dependent and has a strong peak value in case of a strong backscatterer (e.g. cirrus cloud in 10 *km* altitude) in the atmosphere, while it gets almost zero above the cloud in clear atmosphere.

In order to detect cloud base and top, the height-dependent difference of the SNR is used:

$$\Delta SNR = SNR(z_2) - SNR(z_1) \quad (3.28)$$

where $SNR(z_2)$ is the signal-to-noise ratio at altitude z_2 and $SNR(z_1)$ is the Signal-to-noise Ratio at altitude z_1 , with $z_2 > z_1$.

A gradient is then calculated by dividing the difference from equation 3.28 by the difference of the measurement distances. This measurement distance needs to be taken into account, because of the variable vertical resolution, which is shown in section 4.2 for some detection cases.

$$\frac{\Delta SNR}{\Delta z} = \frac{SNR(z_2) - SNR(z_1)}{z_2 - z_1} \quad (3.29)$$

For the following simulations, the vertical resolution is kept close to the applied resolution of the ALADIN Airborne Demonstrator, Figure 3.4. Up to an altitude of 8.837 *km* the vertical resolution is 1.262 *km*, 0.631 *km* up to an altitude of 10.099 *km*, the best vertical resolution of 0.316 *km* is achieved up to an altitude of 12.264 *km*, again 0.631 *km* resolution up to 13.886 *km*, and finally 1.262 *km* for the last range bin up to 15.149 *km*.

For both cases of Figure 3.13, this gradient is shown in Figure 3.15. This figure reveals important properties of the calculated gradients, on the left for an atmosphere without clouds and on the right for an atmosphere with a cirrus cloud at 10 *km*:

- In case of a clear atmosphere the gradient shows almost no height dependency, except for the lowest altitudes,

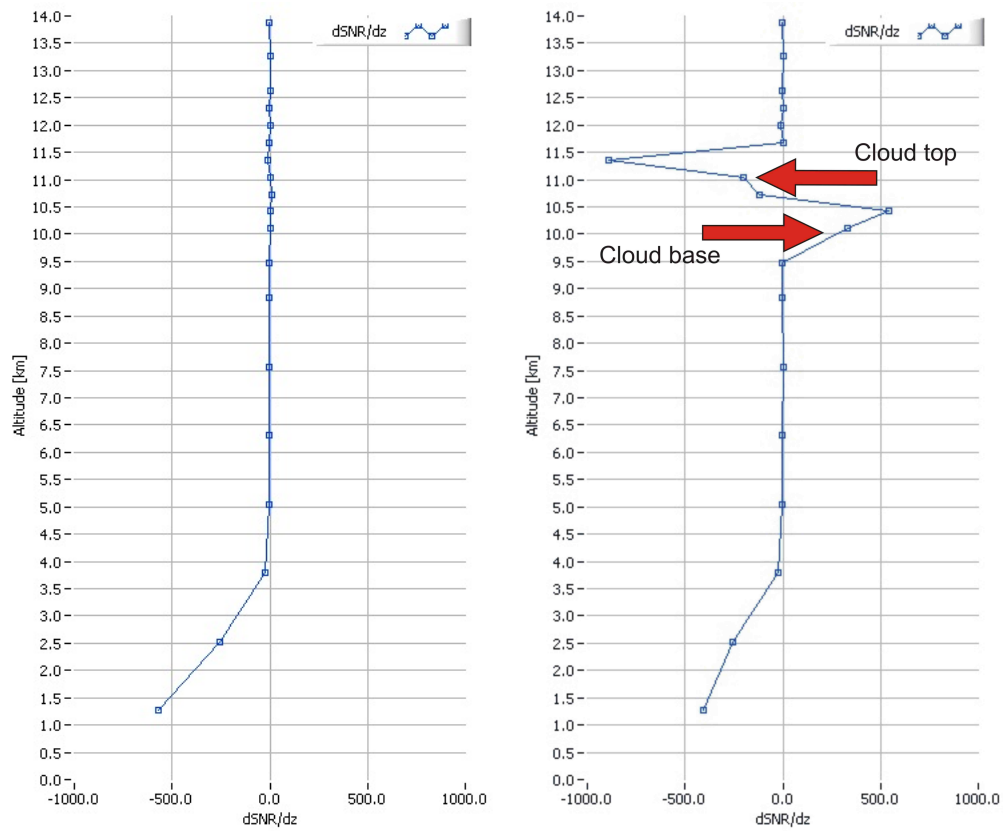


Figure 3.15: Mie SNR-gradient of a clear atmosphere (left) and a cirrus cloud at 10 km (right).

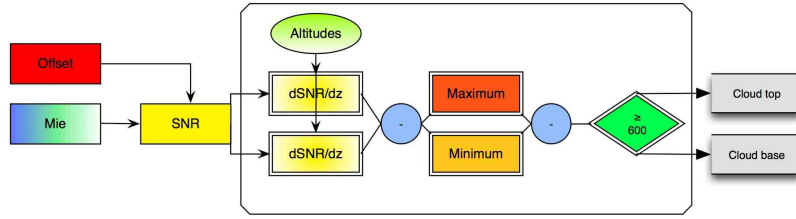


Figure 3.16: Mie channel cloud detection algorithm for the A2D-Simulator.

- When the emitted lidar signal is backscattered by a cloud, the gradient rises to a maximum; several tests with different cloud types, altitudes, and geometrical and optical properties have shown that the real cloud base is located one altitude index below this peak,
- When leaving the cloud, the gradient decreases to a minimum; here the tests have shown that the cloud top is located one altitude index lower, and
- Above the cloud the gradient increases to the clear-sky value below the cloud.

Now, cloud base and cloud top are easily detectable with a single threshold value:

$$\left(\frac{\Delta SNR}{\Delta z}\right)_{max} - \left(\frac{\Delta SNR}{\Delta z}\right)_{min} \geq 600 \quad (3.30)$$

The chosen threshold of 600 was taken due to the strong negative value close to the ground, where the gradient $\frac{\Delta SNR}{\Delta z}$ reaches a value of -300 due to the telescope overlap function and the aerosol backscatter in the boundary layer up to $2 - 3 \text{ km}$. In combination with noise on the signal this value does not exceed the chosen threshold. This threshold is a robust value for testing the cloud detection routine for any cloud type, but it has to be lowered for geometrical and optical thin cirrus clouds, where the peaks in the SNR gradient get close to the noise (down to values of 60 to 100). In case of a cloud (Figure 3.15), the difference of the maximum and the minimum of the gradient exceeds this chosen threshold of 600 (Equation 3.30) and a cloud is detected.

Figure 3.16 shows a simple flowchart of the cloud detection in the case of simulation for the Mie channel.

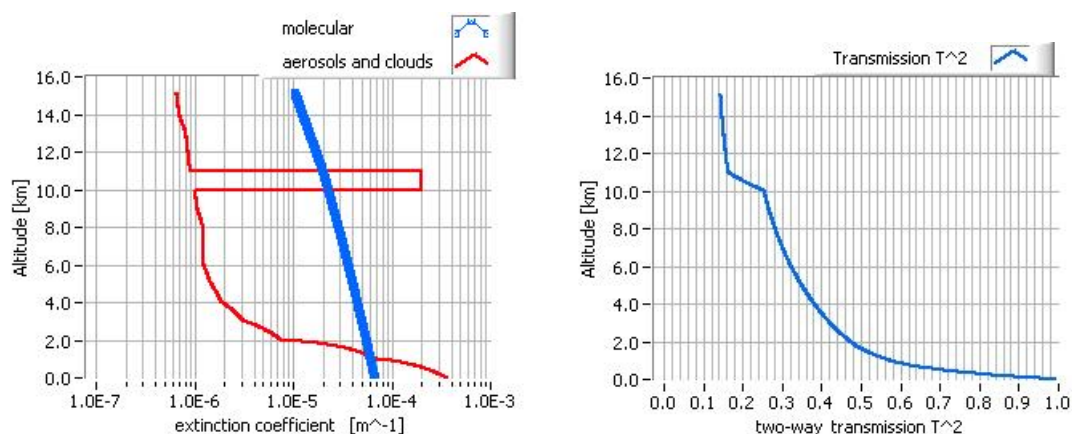


Figure 3.17: Extinction (left) and two-way Transmission (right) of a cirrus cloud at an altitude of 10 km and a depth of 1 km , with a cloud optical depth of 0.2 in the simulated U.S. Standard Atmosphere with Median aerosol model.

3.3.4 Simulated Signals and Minimum Detectable Cloud Optical Depth

In general it is very important to know the minimum detectable cloud optical depths for any cloud detecting system. While it is obvious that optical dense clouds cause a very low transmission for lidar applications, thin clouds are detectable down to very low cloud optical depths.

As one can see from the extinction and transmission in Figure 3.17, the simulated cirrus has a very low extinction, compared to the extinctions of the other cloud types listed in Table 3.1 .

Following Equation 3.11, the two-way transmission T^2 at the base of the simulated cirrus cloud is already fairly low (close to 0.3), and is attenuated by the cirrus cloud itself to a value of 0.15. The cloud optical depth of the simulated cirrus cloud is 0.2.

According to Paffrath et al. [2008], the number of electrons on the Rayleigh ACCD is the same for the satellite instrument ALADIN and for the A2D on ground simulations at an altitude of around 11 km for clear sky atmosphere (Figure 3.18). Due to the fact, that a simulation for the spaceborne instrument is not part of the A2D simulator, and in order to have comparable results of both simulations - for ALADIN and for A2D - a

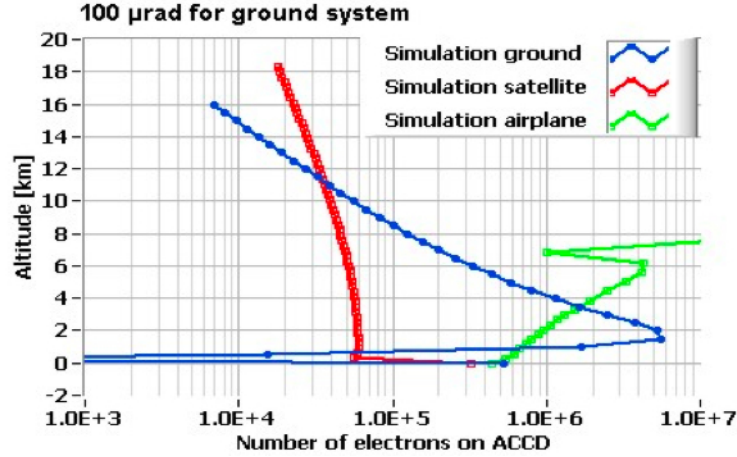


Figure 3.18: Number of electrons on Rayleigh ACCD: simulation for Nadir-pointing ground/airborne/satellite systems with a laser divergence of $100 \mu rad$ [Paffrath et al., 2008].

cloud base altitude of $11.5 km$ is chosen. The telescope overlap function is negligible for atmospheric observations of the satellite instrument, so only the simulated A2D signal above $3 km$ (where the full telescope overlap is simulated) is taken into account for the determination of the minimum detectable cloud optical depth.

With the new possibilities of the simulator introduced in Section 3.2, there are now two ways to decrease the thickness of clouds (optical and geometrical).

The first way is to decrease the depth of the cloud, that means to lower the cloud top starting at $11.6 km$, while the cloud base is kept constant. This is done in steps of one meter until the cirrus disappears to get a very detailed look on the detection sensitivity of A2D. With the cloud depth set to $100 m$, the cirrus cloud is smaller than one range bin of A2D ($315 m$). This is done in order to start with an already thin cirrus and to decrease the simulation time.

The second way is to halven the extinction coefficient for every simulation step n according to:

$$\alpha'_{Cirrus} = \frac{\alpha_{Cirrus}}{2 \cdot n} \quad (3.31)$$

The cloud optical depth can be calculated as (Equation 3.10):

$$\tau = (z_2 - z_1) \cdot \alpha'_{cirrus} = (z_2 - z_1) \frac{\alpha_{cirrus}}{2 \cdot n} \quad (3.32)$$

where $\alpha_{cirrus} = 2.0 \cdot 10^{-4}$ (Table 3.1) and n is the number of the simulation steps (realisations).

When the extinction is lowered, the backscatter coefficient has to be lowered as well in order to keep the lidar ratio constant (Equation 3.8).

For both methods the cloud base is chosen to be in 11.5 *km* altitude with a cloud top at 11.6 *km*.

The simulations are performed for an integration over 18 laser pulses (one measurement) and over 630 laser pulses (one observation) according to Section 3.1.3.

So, the horizontal integration time is lower at the measurement level, which results in a reduced SNR and a lowered scattering ratio compared to the observation level. First the observation level is examined with both ways of decreasing the cloud thickness. With the simulations for observation level (Figure 3.19), the result of the cloud detection routine in the case of decreasing cloud top altitude (upper left) is calculated as:

$$\tau = (z_2 - z_1) \cdot \alpha_{cirrus} = 12m \cdot 2.0 \cdot 10^{-4} m^{-1} = 2.4 \cdot 10^{-3} \quad (3.33)$$

where the minimum detectable geometrical cloud depth is 12 *m* at simulations with constant backscatter and extinction coefficients. With decreasing the cloud's backscatter and extinction, referring to Equation 3.32, the minimum detectable extinction of the cloud with constant geometrical cloud depth is calculated as:

$$\tau = (z_2 - z_1) \cdot \alpha'_{cirrus} = 100m \cdot 2.2 \cdot 10^{-5} m^{-1} = 2.2 \cdot 10^{-3} \quad (3.34)$$

The calculations prove that both cases lead to almost the same result:

A cloud with a cloud optical depth of $2.2 \cdot 10^{-3}$ is still detectable, if the threshold of the SNR-gradient is adjusted in the right way (here: 60 – 80). Using the scattering ratio, as in Equation 3.27, leads to a result similar to that of SNR detection. In order to prevent any false detection, the threshold is set to a value of 1.1, so that a minimum COD of $1.44 \cdot 10^{-3}$ (decreasing cloud depth) and $2.4 \cdot 10^{-3}$ (decreasing backscatter and

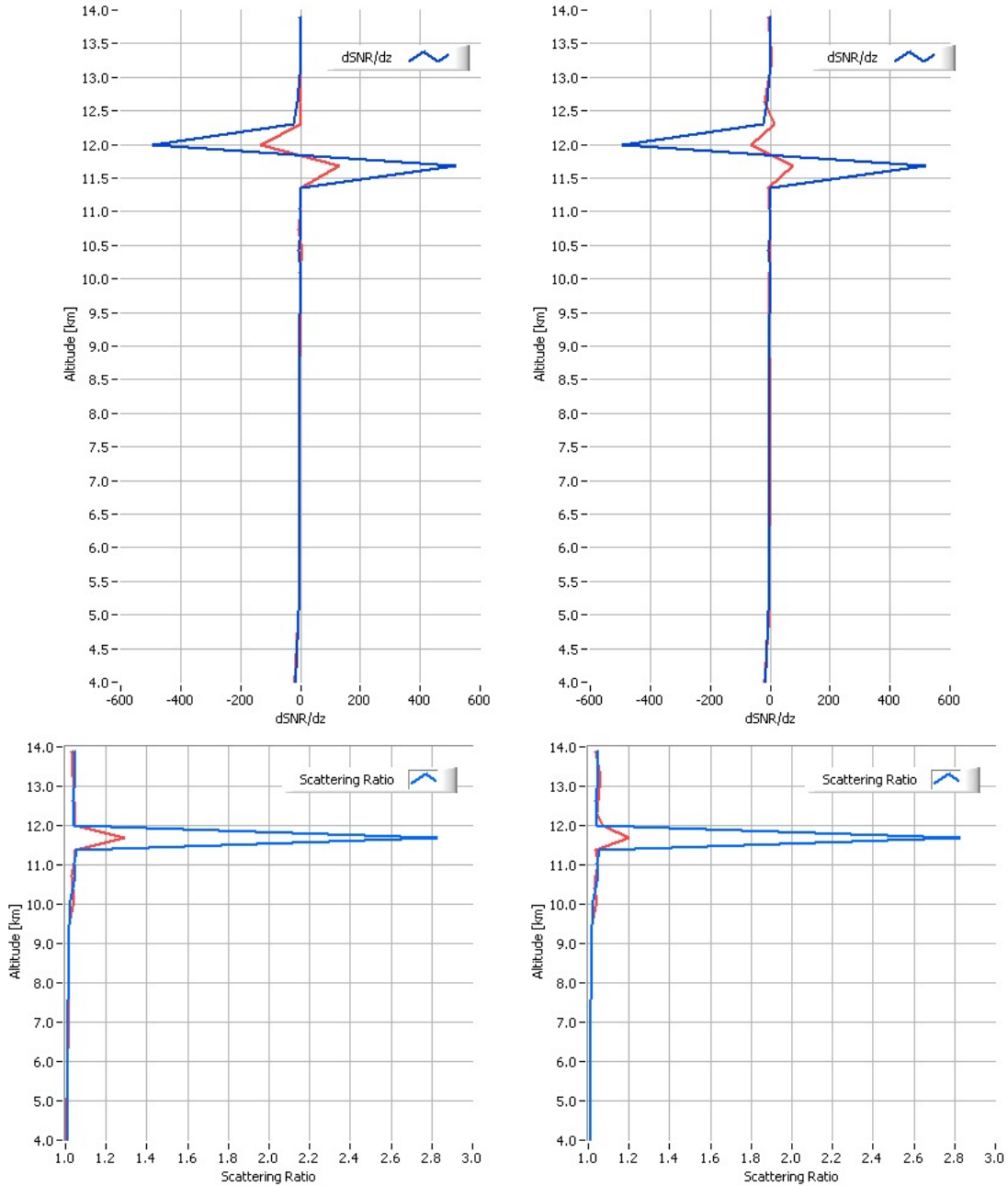


Figure 3.19: SNR-gradient calculated for observation level (630 laser pulses). Decrease in cloud depth (upper row, left) and decrease in extinction and backscatter (upper row, right). The same order for the scattering ratio (lower row). The initial cirrus cloud in blue, the last detected cloud simulation (detection limit) in red. Used thresholds for SNR calculation: 80 (left) and 60 (right), for scattering ratio 1.1.

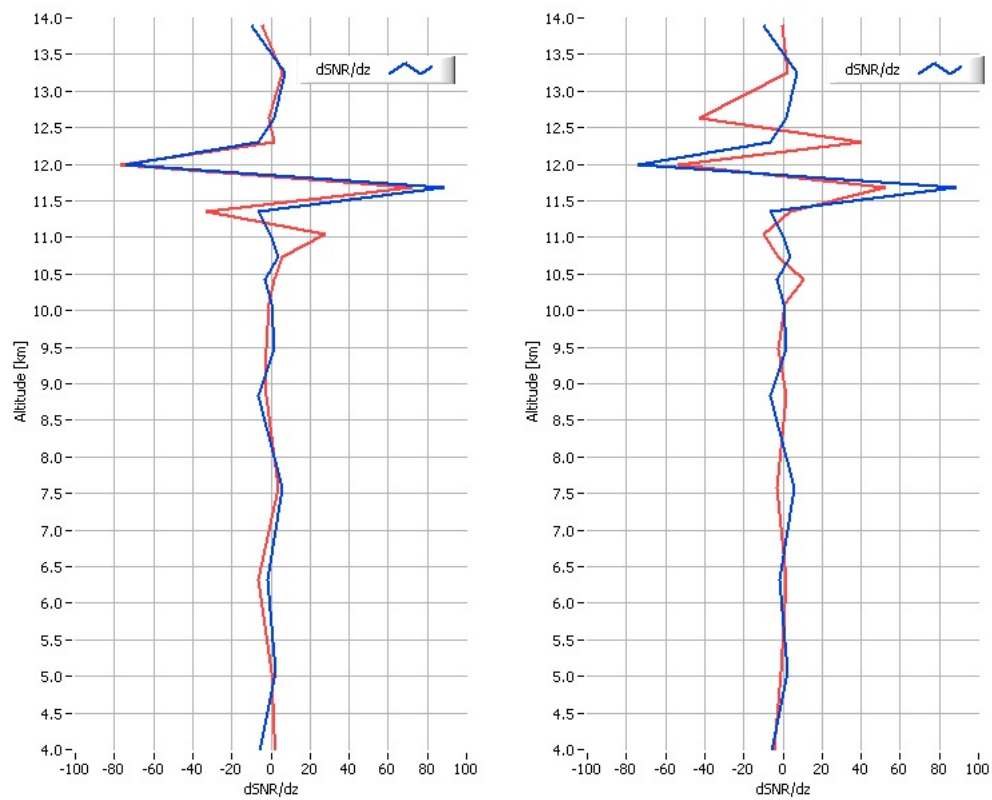


Figure 3.20: SNR-gradient calculated at measurement level. Decrease in cloud depth (left) and decrease in extinction and backscatter (right). The initial cirrus cloud in blue, the detection limit in red.

change in	extinction and backscatter coefficient	cloud depth
Min COD - observation level	$2.2 \cdot 10^{-3}$	$2.4 \cdot 10^{-3}$
Min COD - measurement level	$1.0 \cdot 10^{-2}$	$1.4 \cdot 10^{-2}$
Min COD - Scattering Ratio	$2.4 \cdot 10^{-3}$	$1.4 \cdot 10^{-3}$

Table 3.2: Minimum detectable cloud optical depth for the simulations (observation and measurement level) with decreasing backscatter and extinction coefficients and decreasing cloud depth.

extinction) is detected. A higher threshold would lower the detection sensitivity, while a lower threshold would lead to noise detection.

For the measurement level (18 laser pulses), the SNR gets lower due to the shorter integration time, which is $\frac{1}{35}$ of the observation level (630 laser pulses) as shown in Figure 3.20 . This simulation results in $\tau = 1.4 \cdot 10^{-2}$ for decreasing cloud thickness and in $\tau = 1.0 \cdot 10^{-2}$ for decreasing extinction and backscatter with thresholds of 80 for both simulations.

To summarize:

The results of the detection simulations for the Mie channel are listed in Table 3.2. In the Mie channel it is possible to detect clouds with a cloud optical depth of $\tau = 2.2 \cdot 10^{-3}$ at observation-level and $\tau = 1.0 \cdot 10^{-2}$ at measurement-level. These values are lower than the minimum detectable optical depth of CALIPSO, which is $\tau = 1.5 \cdot 10^{-2} - 7.5 \cdot 10^{-3}$ for 240 laser pulses and $\tau = 5.0 - 7.5 \cdot 10^{-2}$ (day) for 15 laser pulses [Winker et al., 2008]. And is even lower than the COD of subvisible cirrus clouds with a COD of $\tau = 3.0 - 5.0 \cdot 10^{-2}$ [Kärcher, 2002].

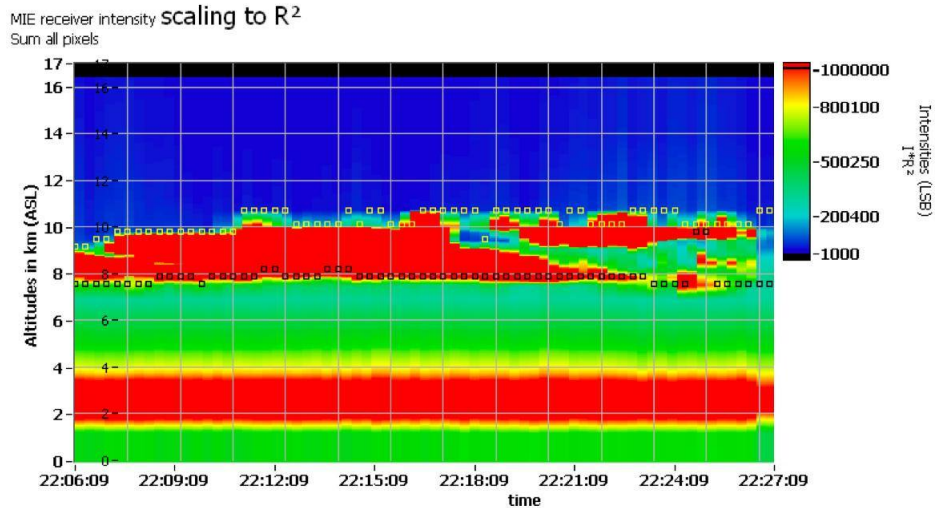


Figure 3.21: Mie receiver intensity, range corrected, 08.07.2007 from 22:06 to 22:27 local time (LT) with schematic detection of cloud base (black dots) and the cloud top (yellow dots).

3.3.5 Observed Signals and Multilayer Cloud Detection

The simulations are performed for single layer clouds. In case of real observations the described detection algorithm (Figure 3.16) results in a single layer cloud. This is shown in Figure 3.21, where the range-corrected Mie receiver intensity is shown in units of *LSB*, the least significant bit, which is the digitiser's smallest unit. Below 4 *km* altitude the strong influence of the telescope overlap causing high intensities on the Mie receiver is viewable and neglected for the detection, while the cirrus cloud has different intensities with a cloud base altitude at 8 *km* and a cloud top at 9 – 10 *km*. The structure or multilayering of the cloud is not detected by the algorithm used for the simulations. Only the boundaries of the cirrus are detectable.

Compared to the simulated SNR values of a cirrus cloud in 9 *km* altitude a real measurement shows several peaks in the Signal-to-Noise Ratio (Figure 3.22, right). The structure of the SNR on the left leads to a clear gradient (Figure 3.23, left). The real data analysis shows that the SNR has peaks for every layer (Figure 3.22) of the cloud causing several minima and maxima at the gradient calculation (Figure 3.23, right).

Ergo, the next step toward detecting multilayer clouds and their structures is to design a kind of sorting routine for the SNR gradient, where not only the global maximum and minimum in a vertical profile indicates cloud base and top, but local maxima and minima.

Beside this search for local maxima and minima, the threshold value is still very important. It still provides the first guess on the detected maxima and minima, before the ordering routine takes place.

In contrast to the simulation the threshold value is now the mean of the whole gradient over one SNR gradient profile plus a chosen value: For the cloud base detection:

$$T_{Mie,cb} = mean \left(\frac{\Delta SNR}{\Delta z} \right)_{Mie} + c_{Mie,cb} \quad (3.35)$$

For the cloud top detection:

$$T_{Mie,ct} = mean \left(\frac{\Delta SNR}{\Delta z} \right)_{Mie} + c_{Mie,ct} \quad (3.36)$$

where $c_{Mie,cb}$ is positive for the cloud base and $c_{Mie,ct}$ is negative for the cloud top. Both values are selectable by the user. In this case $c_{Mie,cb} = 100$ and $c_{Mie,ct} = -100$. For example is $mean \left(\frac{\Delta SNR}{\Delta z} \right)_{Mie} = -68$ for the simulated cirrus cloud in 9 km altitude (Figure 3.23, left).

Both thresholds (Equation 3.35 and 3.36) are the initial guess for a feature and are tested by the ordering algorithm to be a cloud base or top.

After passing the “threshold selection”, the initial guesses are passed to four sorting routines. The routines check if the lowest cloud base is lower than the lowest maximum and the other way around. So, it is checked, if noise leads to failure detections below and above the detected cloud layer.

After those guesses are eliminated, the algorithm continues testing the right order of the possible cloud bases and tops and finally deletes all wrongly ordered bases and tops. This elimination of wrong cloud bases and tops is used to prevent overlapping of cloud bases and tops, and again to prevent noise detection. A rough flowchart of the updated cloud detection routine for the Mie signal is shown in Figure 3.24.

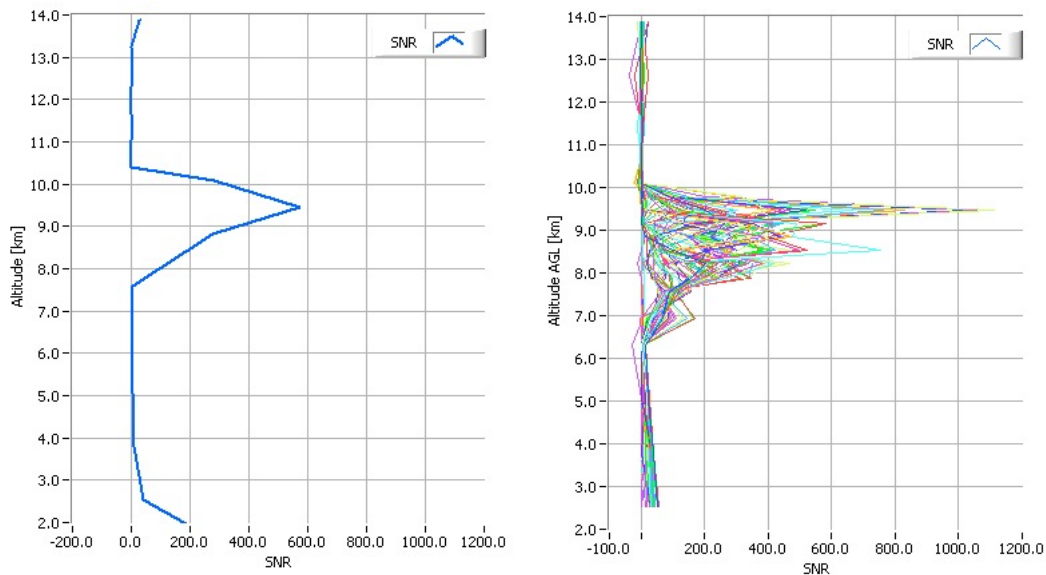


Figure 3.22: SNR of a simulated cirrus at 9 km (left) and of a measured cirrus on the 08.07.2007 from 22:06 to 22:27 local time.

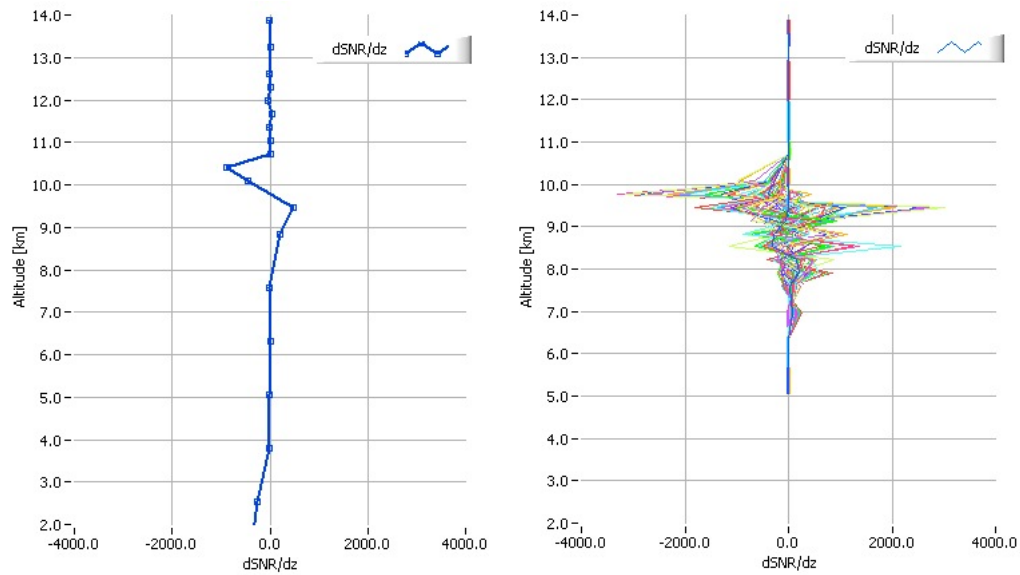


Figure 3.23: The SNR-gradient of a simulated cirrus at 9 km (left) and of a measured cirrus on 08.07.2007 from 22:06 to 22:27 local time.

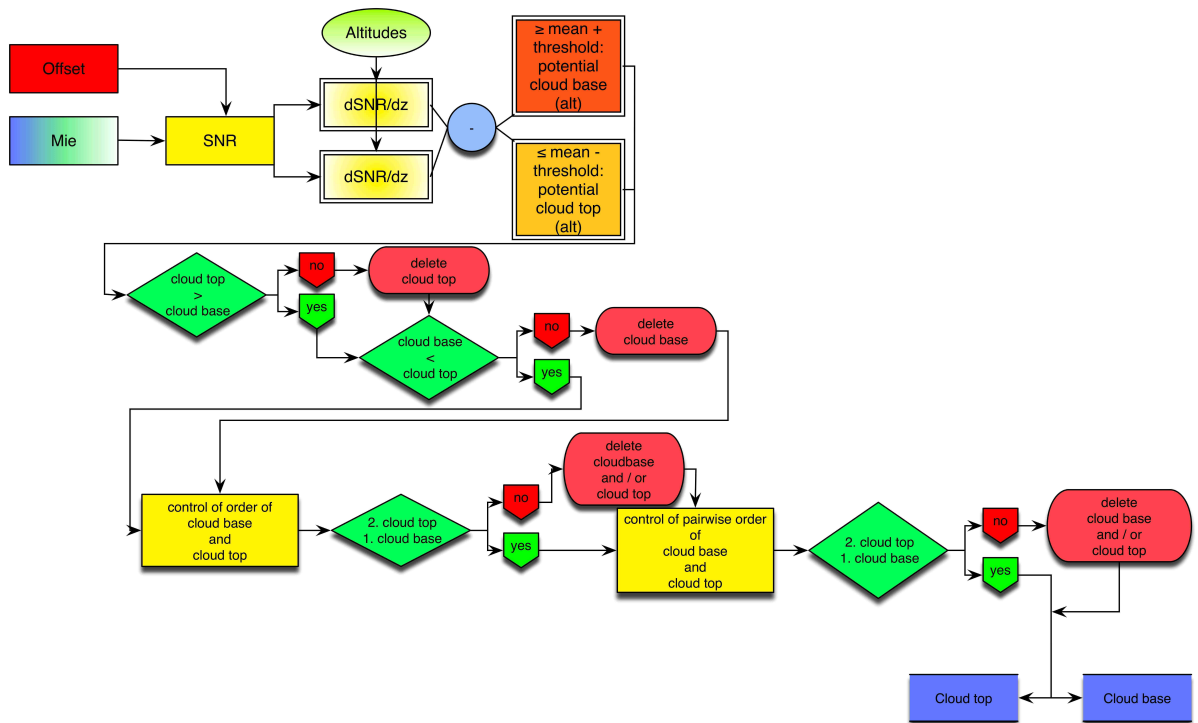


Figure 3.24: Multilayer cloud detection algorithm for the Aladin Airborne Demonstrator for the Mie spectrometer signal.

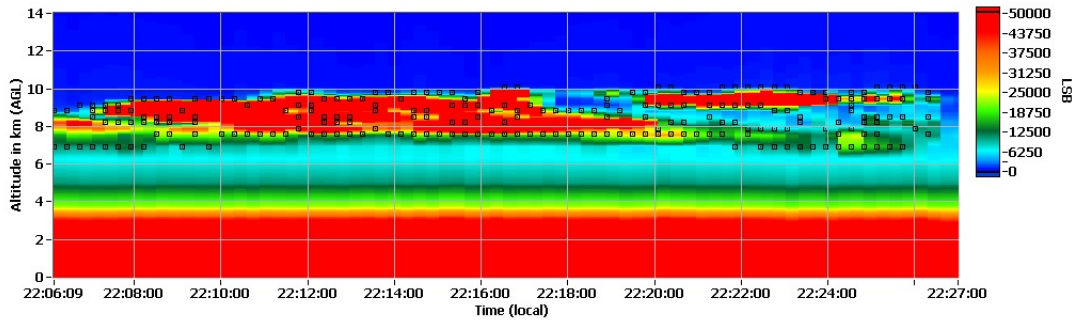


Figure 3.25: Mie receiver intensity, range corrected, 08.07.2007 from 22:06 to 22:27 local time (LT) with schematic detection of cloud base and top (dark points).

The example on the right side of Figures 3.22 and 3.23 is analyzed with this updated detection algorithm in Figure 3.24. Now it is possible to get the real cloud bases and tops including structures like cloud holes and fringes (Figures 3.3.5). The telescope overlap is again not taken into account (up to 4 *km* altitude), while the cirrus cloud from 7 to 10 *km* is detected. Beside the general cloud base and top the structure of the cloud is detected due to the different intensities on the Mie ACCD resulting in up to three layers.

This case will be discussed in more detail in Chapter 4.2.1.

3.4 Cloud Detection from Rayleigh Spectrometer

This section will show that the cloud detection for the Mie spectrometer (Figure 3.24) can be used similarly for the Rayleigh spectrometer. As depicted in Figure 2.4, the two spectrometers will be able to perform observations in different altitudes. So, in addition to the Mie cloud detection, the Rayleigh cloud detection can be used, for example, at high altitudes, which are not in the range of the Mie spectrometer.

3.4.1 Signal-to-Noise Ratio

The received signal on the Rayleigh ACCD is computed as $\sum_{j=0}^{15} P(i, j, k)$, where $i := \text{layer}$, $j := \text{pixel}$, and $k := \text{measurement}$, similar to the Mie signal calculation. Due to the atmospheric noise in combination with the solar background, which is measured separately with a long integration time $t'_i = 3750 \mu s$ in range bin $i = 25$ prior the laser pulse emission. The term $\sum_{j=0}^{15} \frac{t_i}{t'_i} P(25, j, k)$ has to be subtracted for every pixel. This value is scaled by using $\frac{t_i}{t'_i}$ due to the different integration times of the measurement pixel and the background pixel, for example, at a vertical resolution of $315 m$, the ratio is $\frac{t_i}{t'_i} = \frac{2.1 \mu s}{3750 \mu s}$.

The noise is Poisson distributed, so it is defined as $\sqrt{\sum_{j=0}^{15} P(i, j, k) + 2 \sum_{j=0}^{15} \frac{t_i}{t'_i} P(25, j, k)}$. The factor 2 for the “background” is used due to the different time of background and atmospheric backscatter measurement.

Thus, the Signal-to-Noise Ratio for the Rayleigh channel is given by [Streicher et al., 2006]:

$$SNR(i, k) = \frac{\sum_{j=0}^{15} [P(i, j, k) - \sum_{j=0}^{15} \frac{t_i}{t'_i} P(25, j, k)]}{\sqrt{\sum_{j=0}^{15} P(i, j, k) + 2 \sum_{j=0}^{15} \frac{t_i}{t'_i} P(25, j, k)}} \quad (3.37)$$

In order to calculate Equation 3.37 for simulated signals the measured background noise of A2D observations is used. For this reason, a measurement consisting of 95 observations at 630 laser pulses from 06:00 to 06:30 local time on 14.07.2007 was taken

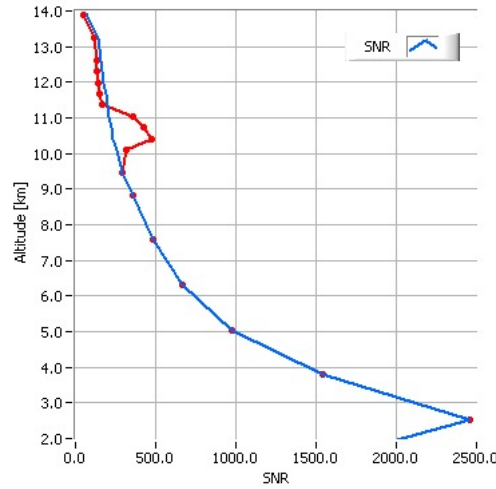


Figure 3.26: Simulated Rayleigh SNR for a clear atmosphere (blue) and with a cirrus cloud at 10 *km* (red) with a geometrical thickness of 1 *km* and a COD of 0.2. Above 11 *km* altitude the Rayleigh backscatter is attenuated by the cirrus cloud.

into account. At this early time it is possible to neglect the solar background radiation, so that the background consists of atmospheric and system noise. The mean of all background measurements was calculated as 1358 *LSB* during 3750 μs . So the Equation 3.37 is updated as follows:

$$SNR(i, k) = \frac{\sum_{j=0}^{15} P_S(i, j, k)}{\sqrt{\sum_{j=0}^{15} P_S(i, j, k) + 2 \sum_{j=0}^{15} \frac{t_i}{t_i} P(25, j, k)}} \quad (3.38)$$

where $P_S(i, j, k)$ is the simulated detected backscattered atmospheric signal, and $P(25, j, k) = 1358$ *LSB* is the measured mean background.

Figure 3.26 shows the Rayleigh signal-to-noise ratio for the simulator according to Equation 3.38. The Signal-to-Noise Ratio shows a strong height dependency over the whole detection range (Figure 3.26). The cirrus cloud at 10 *km* altitude is just

a small peak in the Rayleigh SNR (red) compared to the much stronger peaks of the Mie SNR calculations (c.f. Section 3.3.4), because the cloud backscatter is composed of a spectrally narrowband Mie signal, which is mostly transmitted through the Mie spectrometer. Thus only a small part of the cloud backscatter is reflected towards the Rayleigh spectrometer. Above the cirrus cloud a slight attenuation, depending on backscatter and extinction of the cloud takes place. There, the Rayleigh backscattered signal is lower than the values of a clear atmosphere (blue).

3.4.2 Detection Algorithm

As explained earlier, the Rayleigh detection algorithm is expected to use almost the same detection routine as the Mie algorithm. For this reason, the calculation of the difference of the signal is done according to Equation 3.28:

$$\Delta SNR = SNR(z_2) - SNR(z_1) \quad (3.39)$$

where $SNR(z_2)$ is the SNR at altitude z_2 and $SNR(z_1)$ is the SNR at altitude z_1 , with $z_2 > z_1$.

In order to consider the different vertical resolution, the gradient is created (cf. Equation 3.27):

$$\frac{\Delta SNR}{\Delta z} = \frac{SNR(z_2) - SNR(z_1)}{z_2 - z_1} \quad (3.40)$$

The strong height dependency of the gradient of the SNR (Figure 3.27) makes a cloud detection almost impossible. The strong height dependency leads to a negative gradient especially in the lower atmosphere and converges with a small negative offset to the zero value of the x-axis. When the graph enters the cloud (Figure 3.27, left), it forms a maximum and gets negative above the cloud. This minimum at the cloud top can get close to the signal in the first range bin, especially for clouds with a small optical and physical thickness. A common way to eliminate the range dependency is a range correction of the SNR-gradient $\frac{\Delta SNR}{\Delta z}$ (Figure 3.27, right):

$$\left[\frac{\Delta SNR}{\Delta z} \right]_{rangecorrected} = \frac{SNR(z_2) - SNR(z_1)}{z_2 - z_1} \cdot R^2 = \frac{\Delta SNR}{\Delta z} \cdot R^2 \quad (3.41)$$

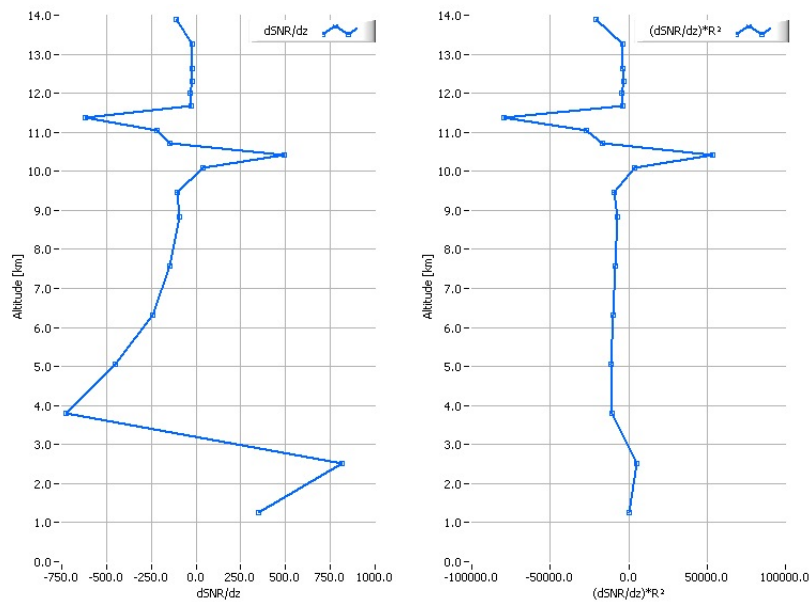


Figure 3.27: Rayleigh SNR-gradient (left) and range-corrected SNR-gradient (right) in case of a cirrus cloud at 10 km with a geometrical depth of 1 km and a cloud optical depth of 0.2.

where R is the range from the lidar system to the backscatter region.

The advantage can directly be seen in Figure 3.27, where the right, range-corrected graph is not height-dependent in contrast to the original gradient on the left, and has a similar shape as the Mie SNR-gradient in Figure 3.15. The differences are:

- a slightly negative offset, which is not relevant, because the cloud detection only searches for the differences between the maximum and the minimum, and
- higher values of the gradient due to the range correction, which makes the detection routine more sensitive for optically and physically thin clouds.

The cloud detection can now be done similar to the Mie cloud detection in Section 3.3.3, but with a much higher threshold value (10000) in the case of a cirrus cloud of 1 km depth. This threshold was again found by several simulations with different cloud types and chosen to prevent false detections. Especially for geometrical and optical thin clouds the threshold has to be lowered.

$$\left(\frac{\Delta SNR}{\Delta z} \cdot R^2 \right)_{max} - \left(\frac{\Delta SNR}{\Delta z} \cdot R^2 \right)_{min} \geq 10000 \quad (3.42)$$

A flowchart is shown in Figure 3.28, which is slightly updated compared to the Mie channel detection algorithm in Figure 3.16.

3.4.3 Simulated Signals and Minimum Detectable Cloud Optical Depth

In order to determine the minimum detectable cloud optical depth, the same cloud simulation (c.f. Section 3.3.4) is done for cirrus clouds with a cloud base altitude of 11.5 km and a cloud depth of 100 m .

Lowering the clouds top altitude from 11.6 km in steps of 1 m is again followed by a simulation with decreasing extinction and backscatter coefficients. Finally the observation level with an integration time of 630 laser pulses and the measurement level with 18 laser pulses is analyzed.

For the observation level, the decreasing cloud top altitude leads to a minimum cloud

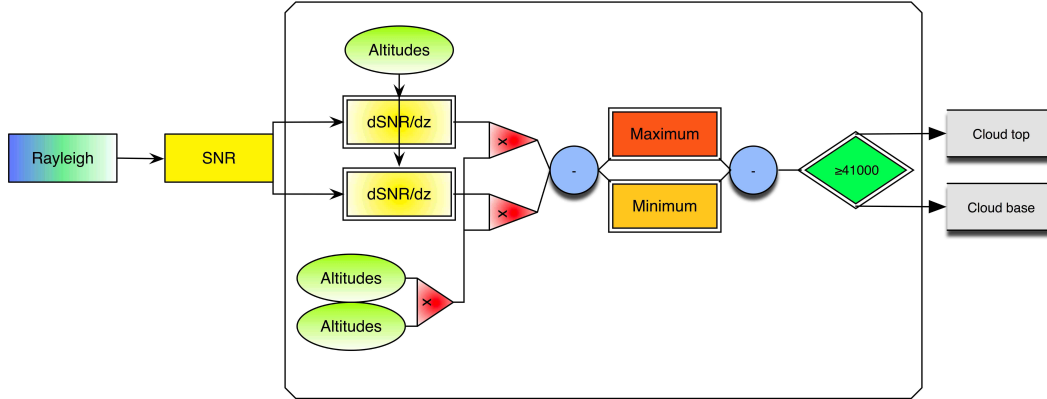


Figure 3.28: Rayleigh channel cloud detection algorithm for the A2D-Simulator.

change in	extinction and backscatter coefficient	cloud depth
Mie Min COD - observation level	$2.2 \cdot 10^{-3}$	$2.4 \cdot 10^{-3}$
Mie Min COD - measurement level	$1.0 \cdot 10^{-2}$	$1.4 \cdot 10^{-2}$
Rayleigh Min COD - observation level	$6.7 \cdot 10^{-3}$	$5.6 \cdot 10^{-3}$
Rayleigh Min COD - measurement level	$1.0 \cdot 10^{-2}$	$1.4 \cdot 10^{-2}$

Table 3.3: Minimum detectable cloud optical depth for the Mie and the Rayleigh simulations (observation and measurement level) with decreasing backscatter and extinction coefficients and decreasing cloud depth.

optical depth of:

$$\tau = 28 \text{ m} \cdot 2.0 \cdot 10^{-4} \text{ m}^{-1} = 5.6 \cdot 10^{-3} \quad (3.43)$$

And for the measurement level:

$$\tau = 72 \text{ m} \cdot 2.0 \cdot 10^{-4} \text{ m}^{-1} = 1.4 \cdot 10^{-2} \quad (3.44)$$

The results for the simulation with decreasing backscatter and extinction coefficients are $\tau = 6.7 \cdot 10^{-3}$ for the observation level and $\tau = 1.0 \cdot 10^{-2}$ for the measurement level. For the Mie and the Rayleigh channel the detection limits are shown in Table 3.3.

Both channels are able to detect clouds with a minimum cloud optical depth of $\tau = 2.2 - 6.7 \cdot 10^{-3}$ at the observation level and $\tau = 1.0 - 1.2 \cdot 10^{-2}$ for the measurement level. So, on both channels a subvisible cirrus is detectable ($\tau_{subvis} = 3.0 - 5.0 \cdot 10^{-2}$ according to Kärcher [2002]). An intercomparison with the performance of NASA's CALIOP instrument onboard CALIPSO shows, that the COD values received with the A2D-Simulator are lower than the CALIOP values at measurement level ($\tau_{A2D} = 1.0 - 1.4 \cdot 10^{-2}$ compared to $\tau_{CALIOP} = 5.0 - 7.5 \cdot 10^{-2}$) and at least in the same region at observation level ($\tau_{A2D} = 2.2 - 6.7 \cdot 10^{-3}$ compared to $\tau_{CALIOP} = 1.5 \cdot 10^{-2} - 7.5 \cdot 10^{-3}$) [Winker et al., 2008].

3.4.4 Observed Signals and Multilayer Cloud Detection

The Rayleigh cloud detection algorithm until here detects only one-layer clouds. For this reason the detection algorithm has to be updated in the same way as the Mie cloud detection to retrieve the structure of multilayer clouds. According to Equation 3.37 the Signal-to-Noise Ratio is computed for A2D observations.

In Figure 3.29 the difference appears clearly with several local minima and maxima on the real data plots (right) and only one strong peak on the simulated signal (left), while the SNR values of the atmospheric signal in cloudfree conditions are comparable (below 7 km). The clouds, detected by A2D (right), at altitudes of 8 – 10 km have higher SNR values than the simulated cirrus, which causes larger SNR-gradients (bottom right, Figure 3.29) than the simulated gradient (bottom left). According to the changes in the Mie cloud detection, the step from fixed to semi-automized thresholds for cloud base and top detection is done:

$$T_{Rayleigh,cb} = \text{mean} \left(\frac{\Delta SNR}{\Delta z} \right)_{Rayleigh} + c_{Rayleigh,cb} \quad (3.45)$$

$$T_{Rayleigh,ct} = \text{mean} \left(\frac{\Delta SNR}{\Delta z} \right)_{Rayleigh} + c_{Rayleigh,ct} \quad (3.46)$$

where $c_{Rayleigh,cb}$ is positive, $c_{Rayleigh,ct}$ is negative. The threshold values are asymmetric $c_{Rayleigh,cb} = +5000$ and $c_{Rayleigh,ct} = -10000$ in this case due to the slightly negative offset of the SNR-gradient profiles in Figure 3.29.

After calculating the thresholds, the search for local minima and maxima is the second step to detect clouds from real data in a proper way. As introduced at the beginning of this chapter, the Rayleigh detection routine is working to work in the same way as the Mie cloud detection (Section 3.3.5).

The first indicator for possible cloud bases and tops are given by the user-defined threshold and passed to the sorting routines, which work in the same way as the Mie routine. With the help of the slightly modified detection routine multilayer clouds and their structure are detectable with high resolution on the Mie spectrometer as well as on the Rayleigh spectrometer. In Figure 3.30, a comparison of the detected cloud bases and tops at the Mie (red) and Rayleigh (yellow) channel is given. The measurement

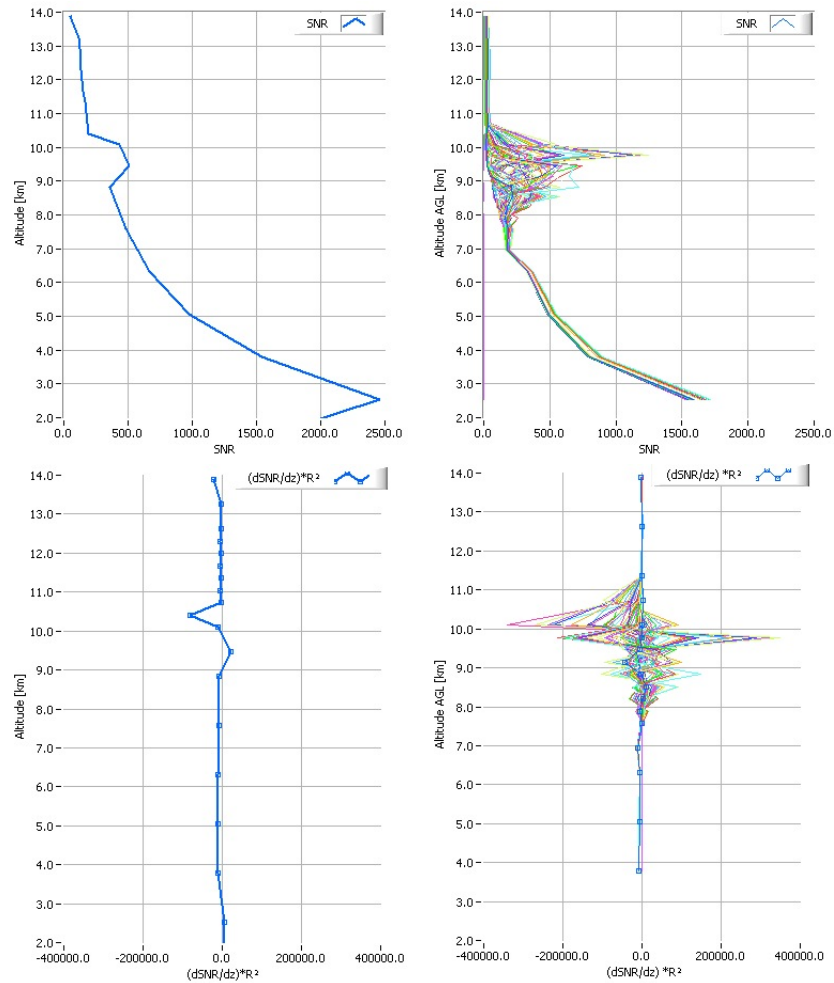


Figure 3.29: Rayleigh SNR for a simulated cirrus at an altitude of 9 km (upper left) and a cloudy case on 08.07.2007 from 22:06 to 22:26 LT (upper right). The results of the range-corrected SNR-gradient for simulation (lower left) and real observations (lower right) is shown.

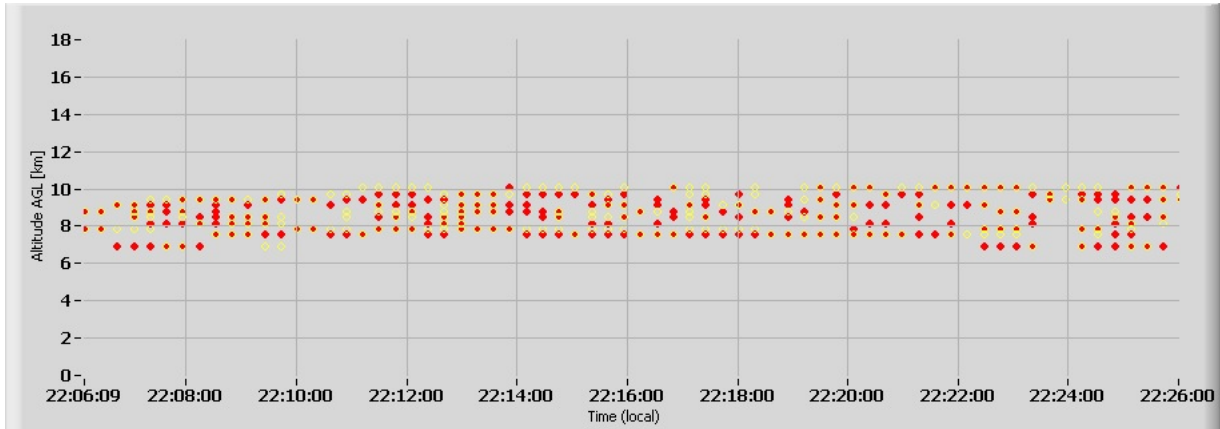


Figure 3.30: Cloud bases and tops for the Rayleigh (yellow) and the Mie (red) detection algorithm on the 08.07.2007 from 22:06 to 22:26 (LT).

was performed on 08.07.2007 from 22:06 to 22:26 and consists of the same data already used for Figure 3.3.5. It is obvious that both detection routines follow the investigated cirrus cloud properly and detect the same cloud bases and cloud tops in most cases. The outer limits of the cloud are detected in a high and comparable quality. Averaged over the the measurement time from 22:06:09 to 22:26:00 LT, with 82 observations taking 117 pairs of cloud bases and tops into account, the Rayleigh multilayer cloud bases are detected 61.2 *m* above the Mie cloud bases within the maximum vertical resolution of 315 *m*, while the Rayleigh multilayer cloud tops are detected 241.2 *m* above the Mie cloud top. Beside these differences in altitude, the number of detected cloud layers per observation differs depending on intensity and structure of the cloud. While the cloud bases, tops, and layers are consistent at 22:13 LT, the Rayleigh spectrometer algorithm detects only one cloud layer compared to two layers on the Mie spectrometer. On the one hand these differences depend on the signal quality on the two spectrometer, on the other hand on the choice of the threshold values for both detection algorithms. In Section 4.2.1 this case is discussed in more detail, where SNR and SNR-gradient profiles make the differences obvious.

A comparison of five different cloud cases detected by the ALADIN Airborne Demonstrator, the **Multiple wavelength Lidar System** (MULIS) of **Meteorologisches Institut der Universität München** (MIM), and a cloud radar of **Deutscher Wetterdienst** (DWD) is given in the next chapter.

Chapter 4

Comparison of A2D, MULIS and Cloud Radar

In Chapter 3.3 and Chapter 3.4 the development of both cloud detection routines - for the Mie and the Rayleigh spectrometer signal - is explained. The quality of the cloud detection routine is now analyzed by a comparison of observed clouds by A2D, MULIS, and a cloud radar.

4.1 Ground Campaign 2007 - Overview

4.1.1 ADM-Aeolus Ground Campaign Objectives

Beside airborne campaign activities in 2007 and 2008 - favorable for a spaceborne lidar [ESA, 2008, Paffrath et al., 2008] - two ground campaigns were accomplished in October 2006 and July 2007 at the Richard-Aßmann-Observatory at Lindenberg, Germany. During the second ground campaign 186 hours of atmospheric measurements were accomplished by scientists of **Deutsches Zentrum für Luft- und Raumfahrt** (DLR), **Deutscher Wetterdienst** (DWD), and **Meteorologisches Institut der Universität München** (MIM). The main objectives were, according to Reitebuch [2006]:

- Validation of the predicted radiometric and wind measurement performance.



Figure 4.1: Measurement set-up of the ALADIN Airborne Demonstrator (container, right), the backscatter lidar MULIS (trailer, left), and the 482 MHz wind profiler (background right) at the Richard-Aßmann-Observatory, Lindenberg, in July 2007.

- Establishing a dataset of atmospheric measurements obtained with an ALADIN type instrument in order to improve algorithm development (corrected and uncorrected horizontal line-of-sight HLOS wind speed, aerosol and cloud products).

These main objectives include establishing of aerosol and cloud products, which are necessary for analyzing and testing the cloud detection algorithm for real observations. So, beside data for wind profile validation, aerosol and cloud observations performed by different instruments (backscatter lidar MULIS, cloud radar) are used for the comparison. Due to the relatively flat orography around Lindenberg, situated 50 km east of Berlin, and a very high variety of remote sensing instruments, the Observatory Lindenberg is suitable for wind profile validation campaigns [Paffrath et al., 2008]. The so called “Lindenberg Column” is a monitoring concept consisting of surface observations, aerological in-situ measurements as well as active and passive remote-sensing techniques.

All measurements were performed simultaneously during the six weeks of campaign in 2007 in order to characterize the atmospheric conditions like clouds, aerosols and wind for an intercomparison with A2D.

In addition to the data provided by the ALADIN Airborne Demonstrator, observations performed by the "METEK MIRA 36" cloud radar and the backscatter lidar MULIS (Figure 4.1) are used and described in the following.

4.1.2 METEK MIRA 36 - Cloud Radar of DWD

The 35.5 *GHz* cloud radar "METEK MIRA 36" is a Ka-Band Doppler radar with high sensitivity allowing to observe even light clouds. It is designed for unattended long-term operations using a magnetron as a transmitter providing 30 *kW* pulse power with 100 *ns* pulse duration. The receiver provides a range resolution of 15, 30, and 60 *m* according to 100, 200, and 400 *ns* pulse width [<http://www.metek.de/mira36.pdf>]. The cloud radar provides a wavelength of $\lambda = 8.45$ *mm*, so mostly scattering from cloud particles is detected.

In this diploma thesis the reflectivity factor is used to get a first overview of the detectable cloud bases and cloud tops. The reflectivity factor Z converts the analog power (in units of *Watt*) received by the radar antenna into a more usable quantity. The reflectivity factor Z takes into account several factors, including the distance of a target from the radar, the wavelength of the transmitted radiation, and certain assumptions about the kind and size of targets detected by the radar. Regarding the drop-size distribution $N(D)$ as a continuous function of drop size D , Z may be written as:

$$Z = \int_0^{\infty} N(D) \cdot D^6 dD \quad (4.1)$$

4.1.3 MULIS - Multiple Wavelength Lidar System of the University Munich

The aerosol backscatter lidar MULIS, developed by the MIM was deployed during the ground campaign. This lidar - equipped with a Nd:YAG laser - transmits three



Figure 4.2: Aerosol backscatter lidar MULIS set up in trailer.

wavelengths: 355 nm , 532 nm , and 1064 nm with a repetition rate of 10 Hz . The pulse-energy is 175 mJ at 1064 nm , 50 mJ at 532 nm , and 175 mJ at 355 nm . In order to obtain qualitative backscatter and extinction coefficients and to be able to observe atmospheric volumes, the lidar was constructed as a scanning system with a telescope diameter of 301 mm [Wiegner et al., 1995].

For a more precise characterization of aerosol particles and in order to derive extinction and backscatter coefficients quantitatively at night, two Raman channels (387 nm and 607 nm) only sensible during night, were implemented recently [Freudenthaler et al., 2009]. Another important issue is the possibility of transportation and measurement set-up in a trailer. For this work the range-corrected 532 nm backscattered signal with parallel polarisation is used providing a temporal resolution of 10.5 s and an averaged vertical resolution of 75 m , derived from the 7.5 m range resolution of the digitalized signal.

4.2 Cases

In this section, five cases of different cloud events during the ADM-Aeolus ground campaign from July 2007 are analyzed. The result of the cloud detection of real data measurements of A2D are compared and discussed with the data collected by MULIS and the cloud radar.

4.2.1 Multilayer Cirrus Cloud - 08.07.2007

The first analyzed case was measured on 08.07.2007 from 22:06 to 22:26 local time (LT). At that time a cirrus with a cloud base at around 8 *km* and a cloud top at 10 *km* was covering the sky over Lindenberg. The cloud's top altitude lies within the maximum resolution of the here used cirrus mode (Figure 3.4), while the cloud base is located at the boundary of two different resolutions, 315 *m* and 630 *m*.

Figures 4.3 and 4.4 show the range-corrected signals of the Mie and the Rayleigh spectrometer of A2D. Each dot represents the center of one range bin, where either a cloud base (black square) or a cloud top (black diamonds) is detected, as in the following Sections.

As shown in Section 3.4, the cloud detection works almost similarly for both spectrometers, but with some differences, which are, on the one hand, slightly different cloud tops and bases (especially after 22:21) and, on the other hand, a different “cloud structure detection”.

The first mentioned differences occur at clouds with low intensities, which have no extinct cloud boundaries to be identified on the A2D signal. This is checked for plausibility, for example, at 22:24 in Figure 4.5 where a slight positive shift in altitude of the lowest Rayleigh SNR cloud peaks is visible compared to the first Mie SNR cloud peaks.

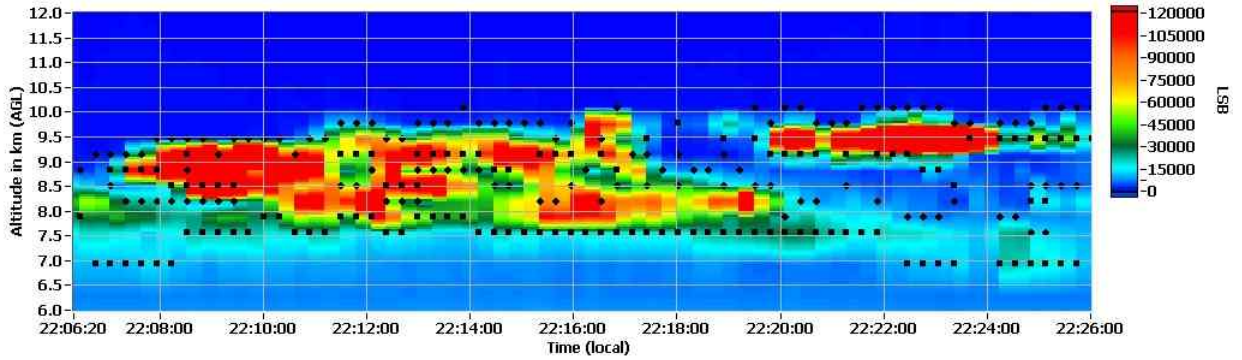


Figure 4.3: Range-corrected Mie receiver intensity (colour coded) with detected cloud bases (black square) and tops (black diamonds) on 08.07.2007.

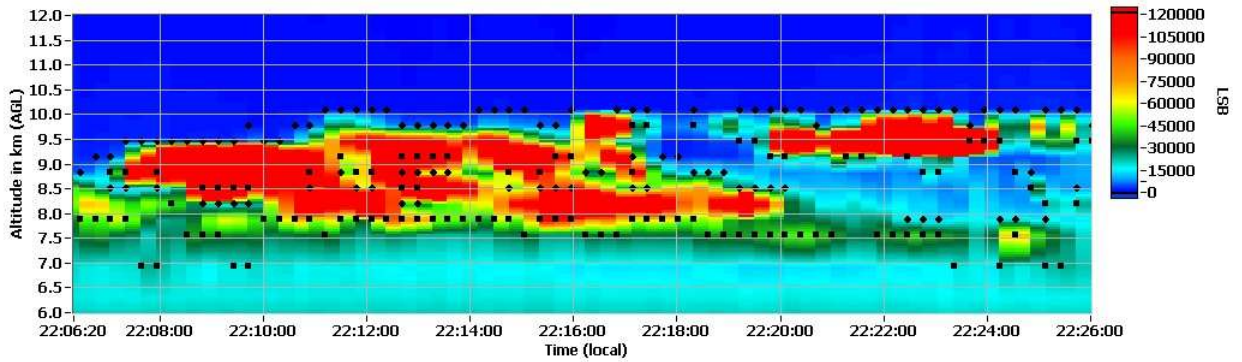


Figure 4.4: Range-corrected Rayleigh receiver intensity (colour coded) with detected cloud bases (black square) and tops (black diamonds) on 08.07.2007.

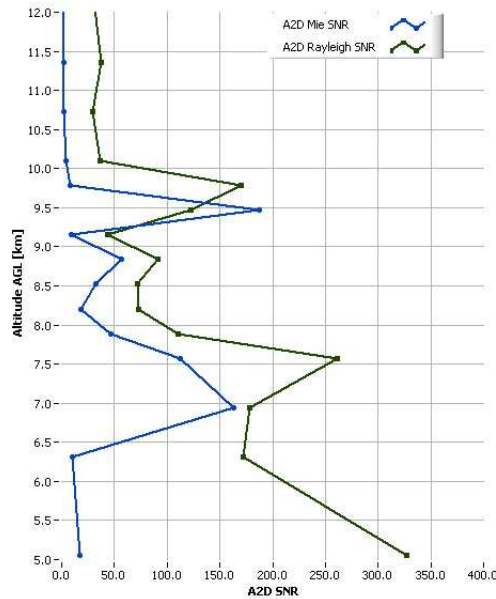


Figure 4.5: Signal-to-Noise Ratio of the Mie (blue) and the Rayleigh (green) channel at 22:24:30.

For the second mentioned discrepancy - the cloud structure analysis - it is necessary to compare the A2D cloud detection to the backscatter signal of the MULIS lidar, which offers a nominal vertical resolution of 7.5 m . This high resolution was averaged to 75 m , which is more than sufficient compared to the maximum vertical resolution of 315 m of the A2D. Beside the higher vertical resolution, the MULIS data are integrated to a horizontal resolution of 10.5 s , while the A2D provides a temporal resolution of 18 s . Therefore, differences in the MULIS backscatter signal and the A2D cloud detection have to be expected. The range-corrected MULIS 532 nm backscatter signal with parallel polarisation is shown colour coded, while the cloud detection of the A2D Mie and Rayleigh spectrometer is plotted as black symbols.

The intercomparison with the MULIS signal (Figure 4.6 and 4.7) shows fairly small differences. The structure of the cloud is comparable between A2D and MULIS in most cases. Even cloud holes and gaps are detectable. If the intensities of the background signal and the cloud get close to each other, structures fail detection.

In general, only some cloud bases deviate from the MULIS intensity signal (for Mie at the start of the measurement and around 22:24, for Rayleigh at the start of the measurement and around 22:27) are detected. This is related to the MULIS backscatter signal starting to increase over at least two range bins of A2D (Figure 4.8), while it reaches its maximum in the third range bin. So, the cloud base peak in the gradient of the SNR is located in this range bin (at 8.2 km altitude) and the cloud base is detected at an altitude of 7.9 km . The first cloud top is detected at an altitude of 8.5 km , which is caused by a decreasing SNR on the A2D spectrometers. But this increase is not viewable in the MULIS backscatter profile where another intensity peak with low vertical extent is located at an altitude of 8.8 km . Above this peak the cloud backscatter decreases up to an altitude of 10.2 km at the MULIS backscatter signal as well as at the A2D SNR profiles for Rayleigh and Mie.

This means, if the intensity of a cloud is increasing at the cloud base over more than one range bin until the maximum intensity if the cloud is reached. The A2D cloud detection locates the right cloud base at least one range bin too high. The same happens to cloud tops at 22:24 on both spectrometers.

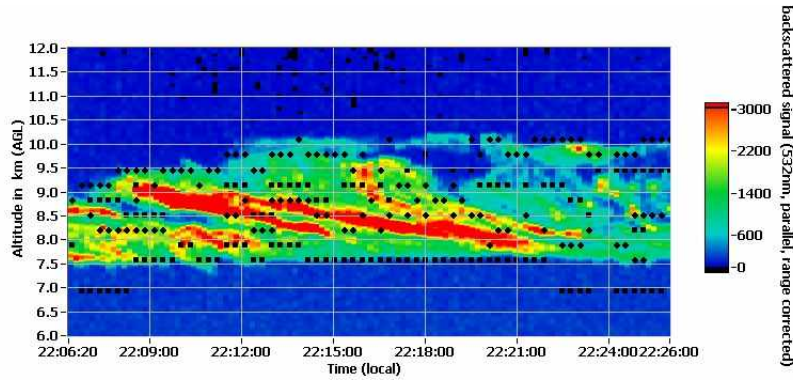


Figure 4.6: Range-corrected MULIS backscatter signal (colour coded) with the A2D Mie Cloud Detection (black symbols) on 08.07.2007.

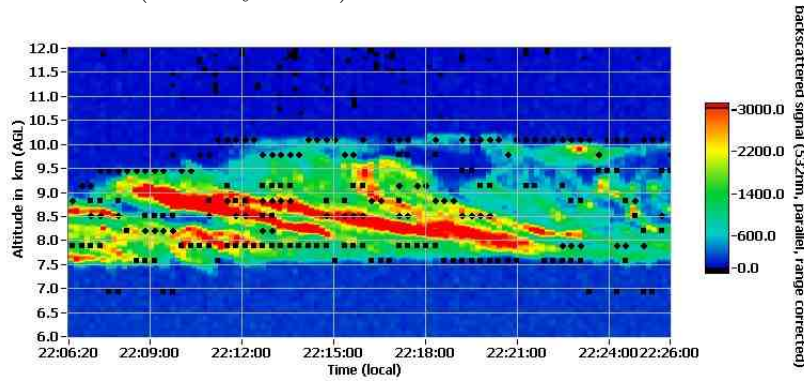


Figure 4.7: Range-corrected MULIS backscatter signal (colour coded) with the A2D Rayleigh Cloud Detection (black symbols) on 08.07.2007.

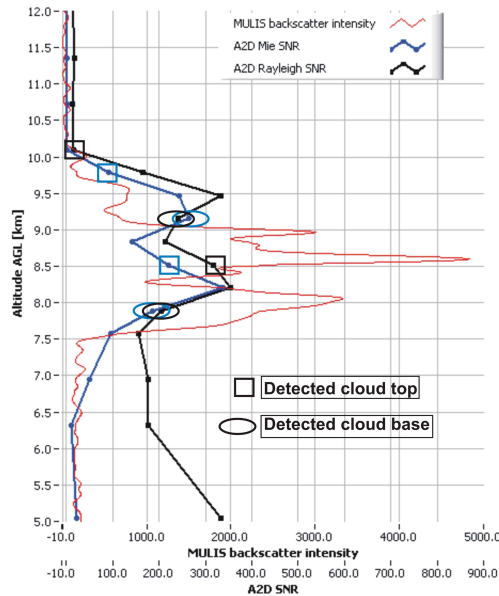


Figure 4.8: A2D Mie SNR (blue), A2D Rayleigh SNR (black) compared to the MULIS backscatter intensity (red) at 22:12.

4.2.2 Deep Broken Cumulus Clouds - 11.07.2007

On 11.07.2007, dense but broken clouds were covering the sky during the measurement timeline from 11:44 to 12:00 LT shown here. For A2D, the detection of low clouds is limited to the geometric arrangement of the emitter and receiver optics, which determines the telescope overlap function.[Weitkamp, 2005, p.5]. This function varies with range and depends on the laser beam diameter, shape and divergence, the telescope's imaging properties, the receiver field of view, and the location of emitter and receiver optical axes relative to each other. For A2D the telescope overlap function is one at a range of 2 – 3 *km*. But this is not relevant for the ADM-Aeolus satellite, where the full telescope overlap is located in the observation regions.

A comparison of the Mie spectrometer detection (Figure 4.9) and the Rayleigh spectrometer detection (Figure 4.10), shows some differences. The Mie detection is sensitive to the atmospheric boundary layer (for example at 11:54 LT), which is not found by the Rayleigh algorithm. Regarding to the telescope overlap, this case proves that the cloud detection algorithm is limited by the quality of the received signal as well.

The intercomparison of the A2D channels and the backscatter signal of the MULIS lidar (Figure 4.11 and 4.12) just confirms the described overlap problems. The Mie channel indicates some good detections of cloud bases, but several failures at cloud top detection, while around 11:54 the structure of the boundary layer is detected.

The Rayleigh channel detects a strong peak within the boundary layer close to the real cloud bases and estimates the tops in a conclusive way with differences of ± 300 *m* altitude.

So, even in case of low signal quality due to the telescope overlap function, A2D can detect aerosols and clouds in the near field of the lidar, and it is possible to find exact cloud tops and bases within an altitude difference of ± 500 *m*.

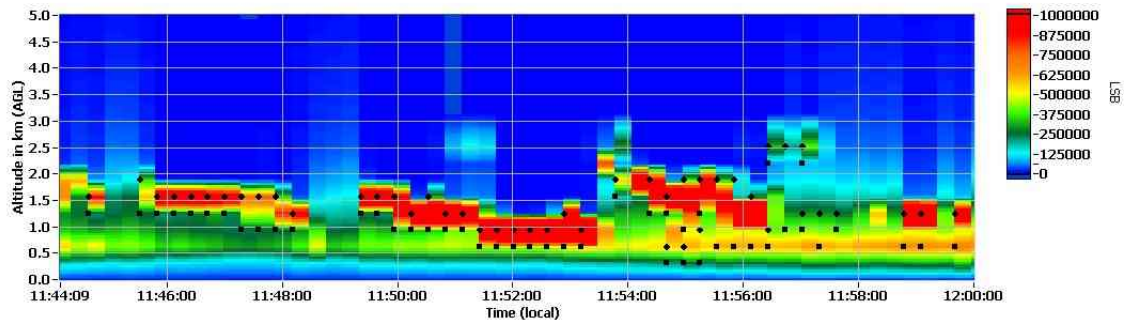


Figure 4.9: Range-corrected Mie receiver intensity (colour coded) with detected cloud bases (black square) and tops (black diamonds) on 11.07.2007.

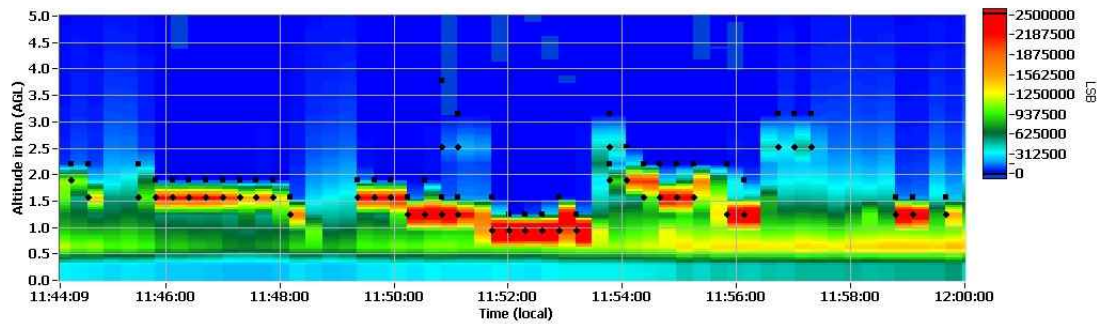


Figure 4.10: Range-corrected Rayleigh receiver intensity (colour coded) with detected cloud bases (black square) and tops (black diamonds) on 11.07.2007.

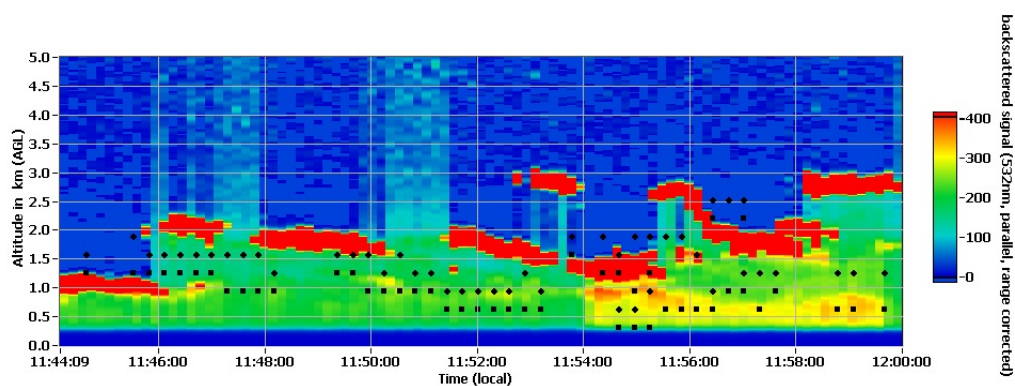


Figure 4.11: Range-corrected MULIS backscatter signal (colour coded) with the A2D Mie Cloud Detection (black symbols) on 11.07.2007.

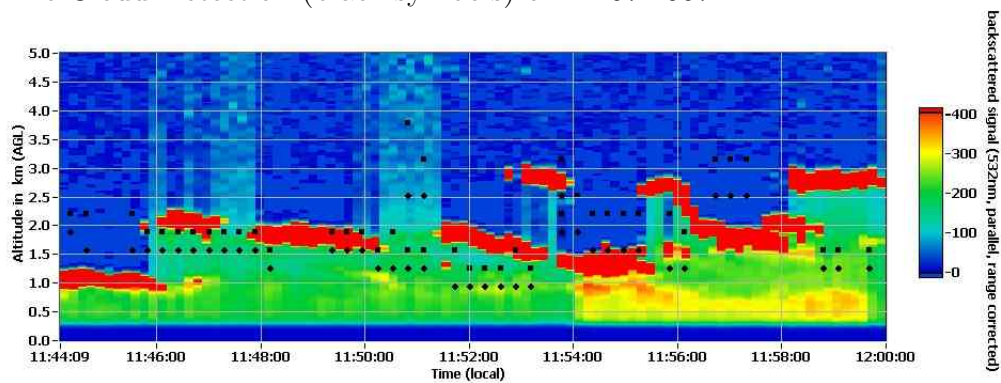


Figure 4.12: Range-corrected MULIS backscatter signal (back) with the A2D Rayleigh Cloud Detection (black symbols) on 11.07.2007.

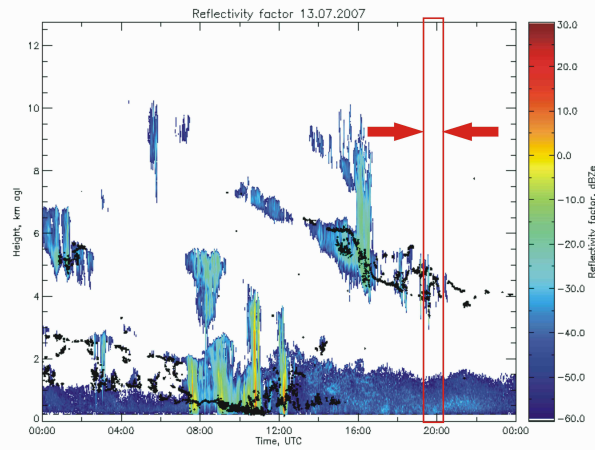


Figure 4.13: Reflectivity factor of the DWD cloud radar (colour coded) and cloud bases detected by Ceilometer (black dots) on 13.07.2007.

4.2.3 Thin Cloud at Medium Altitudes - 13.07.2007

The next cloud case was measured on 13.07.2007 from 21:41 until 22:09 LT. On the cloud radar a very thin cirrus cloud is detected in the late afternoon starting at 16:00 UTC (Figure 4.13). This cloud case is analyzed in contrast to the cirrus in Section 4.2.1 due to its small vertical extent. The multilayering cirrus cloud on the 08.07.2007 had a vertical dimension of 2 *km* compared to the maximum extent of around 500 *m* here.

The detection quality of this cloud on the Mie and the Rayleigh spectrometer has the same structure (Figures 4.14 and 4.15). Cloud bases are detected in the same altitudes, while the tops differ in a few cases, where cloud tops are detected one range bin lower on the Mie compared to the Rayleigh.

Figure 4.16 shows the Mie (blue) and the Rayleigh (green) SNR gradients at 21:43 LT. Additionally, the thresholds for each gradient are plotted in the same color. While the Mie gradient exceeds its threshold for the cloud base and the cloud top exactly for one time each (in 4.2 *km* altitude for the base and in 5.7 *km* for the top), the Rayleigh gradient corresponds to the Mie signal with one peak for the cloud base above the threshold, but two peaks exceed the cloud top threshold. Due to the fact, that the upper peak (at 7 *km*) is more in the negative than the lower peak (at 5.7 *km*), it is

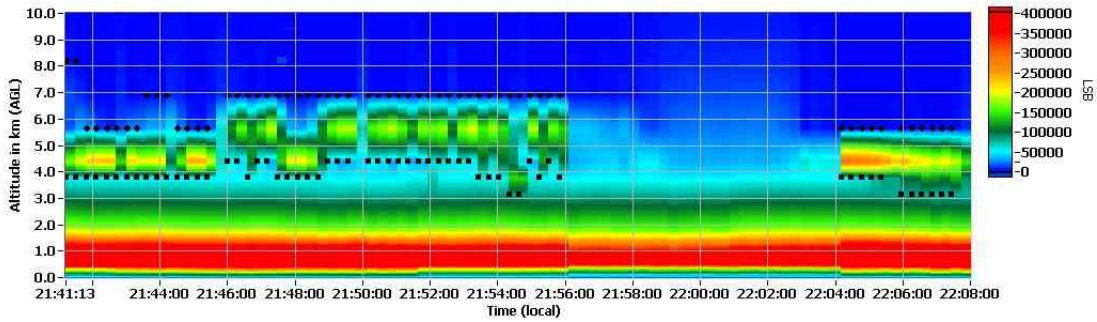


Figure 4.14: Range-corrected Mie receiver intensity (colour coded) with detected cloud bases (black square) and tops (black diamonds) on 13.07.2007.

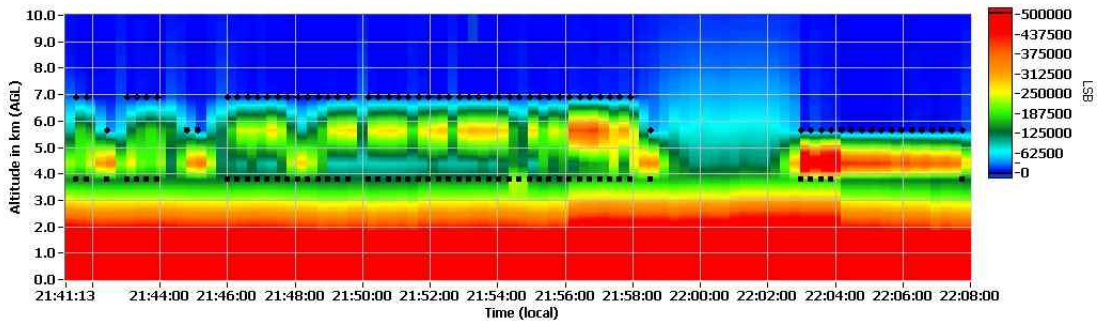


Figure 4.15: Range-corrected Rayleigh receiver intensity (colour coded) with detected cloud bases (black square) and tops (black diamonds) on 13.07.2007.

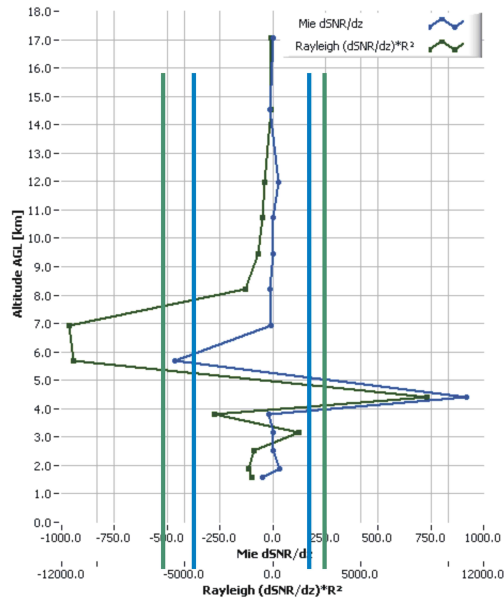


Figure 4.16: SNR gradients of the cloud detection routine for the Mie channel (blue) and the Rayleigh channel (green) at 21:43 LT. The threshold limits for Mie (straight lines, blue) and for Rayleigh (straight lines, green).

identified as the cloud top.

A change in signal strength on the received A2D intensities takes place on the Mie spectrometer from 21:56 to 22:04 LT, which is caused by a commanded frequency shift of the laser. Between 21:59 and 22:02 the range-corrected Rayleigh signal shows a cloudless sky.

The intercomparison of MULIS and A2D shows comparable cloud bases (Figure 4.17 and 4.18) with a negative offset. This offset is caused by the coarse vertical resolution of 630 m of A2D at this altitude and the small vertical dimension of the cloud layers (Figure 4.19). The MULIS backscatter intensity shows two sharp intensity increases (Figure 4.19). The first one is located at the center one range bin of A2D (4.5 km) with a sharp decrease only one hundred meters above. The cloud base is detected by A2D at an altitude of 3.7 km, due to the algorithm. It can be identified as the base of the cloud layer (Figure 4.14 and 4.15). The second intensity peak at the MULIS backscatter signal (5.4 km up to 5.6 km) is again located close to the center of another range bin of A2D (5.7 km). This cloud peak cannot be segregated from the first cloud layer due to the fact that both cloud layers are located in two contiguous range bins. The cloud detection algorithm for the Mie and the Rayleigh spectrometer searches pairwise for cloud base and cloud top to detect a cloud layer.

At Figure 4.19 an overestimation, for example at 21:43 LT, of the detected cloud top on the Mie and the Rayleigh spectrometer is clearly visible. This is caused by a slower decrease of the A2D Rayleigh SNR. Even though the Mie signal is not influenced by the strong signal peak caused by the second cloud layer detected by MULIS in 5.5 km altitude, the Rayleigh signal reaches its minimum one range bin higher, due to the cloud scattering of this second layer (Figure 4.16).

Overall the intercomparison of A2D detection and the MULIS backscattered signal in Figures 4.17 and 4.18 shows, that A2D cloud detection is limited by the vertical resolution. If multilayer clouds have a vertical distance lower than the vertical resolution of A2D, the cloud detection has difficulties to locate the cloud bases and tops in the correct altitude.

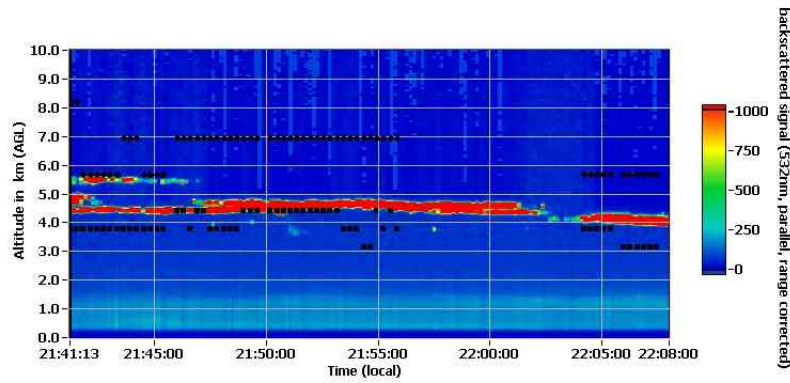


Figure 4.17: Range-corrected MULIS backscatter signal (colour coded) with the A2D Mie Cloud Detection (black symbols) on 13.07.2007.

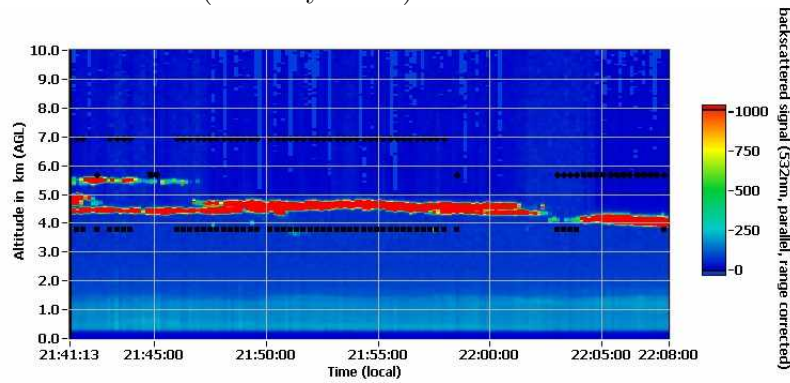


Figure 4.18: Range-corrected MULIS backscatter signal (colour coded) with the A2D Rayleigh Cloud Detection (black symbols) on 13.07.2007.

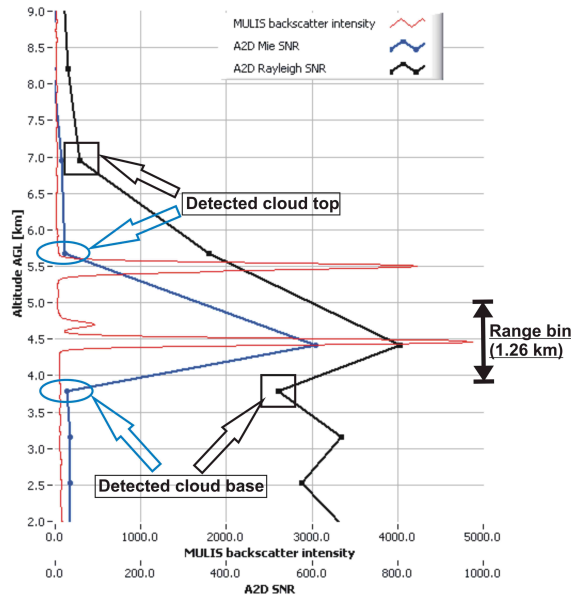


Figure 4.19: A2D Mie SNR (blue), A2D Rayleigh SNR (black) compared to the MULIS backscatter intensity (red) at 21:43 LT.

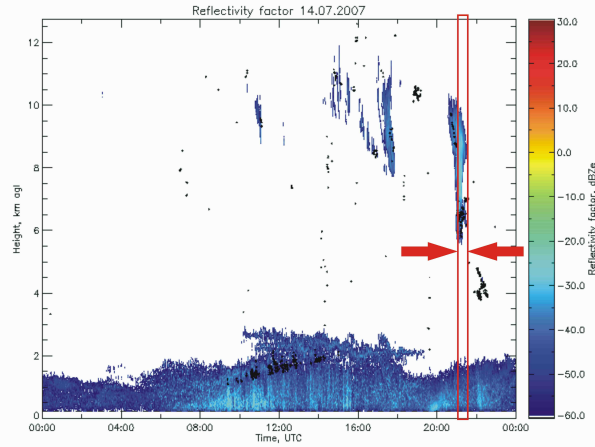


Figure 4.20: Reflectivity factor of the DWD cloud radar (colour coded) and cloud bases detected by Ceilometer (black dots) on 14.07.2007.

4.2.4 Thin Cirrus Cloud - 14.07.2007

The cloud radar on 14.07.2007 shows a cirrus cloud with a base at $5.5 - 6 \text{ km}$ at around 21:00 UTC. The altitude of the cloud top is not clearly indentifiable. Strong structures of this cirrus reach around 7 km , while weak structures with a low reflectivity factor reach 10 km .

During the measurement from 22:59 to 23:27 (LT) the Mie spectrometer intensity shows an false detection behavior for the cloud with detections above the comprised cloud caused by noise and low scattering intensities above the cloud. An intercomparison of Figure 4.21 with the intensity scale of the Mie spectrometer in Figure 4.3 (Section 4.2.1) shows, that in this case the intensities of the cirrus cloud are lower (40000 compared to 120000 *LSB*). Thus, the threshold values for the cloud detection have to be small. But in case of small thresholds a higher false detection rate gets obvious (Figure 4.21 and 4.22). The cloud detection has false detections especially in the Mie spectrometer above altitudes of 8.5 to 10 km . On the Rayleigh receiver (Figure 4.22) several cloud layers are detected with less “noise” failures above the cloud.

In general, the algorithm detects the different intensities between 5 and 9 km altitude

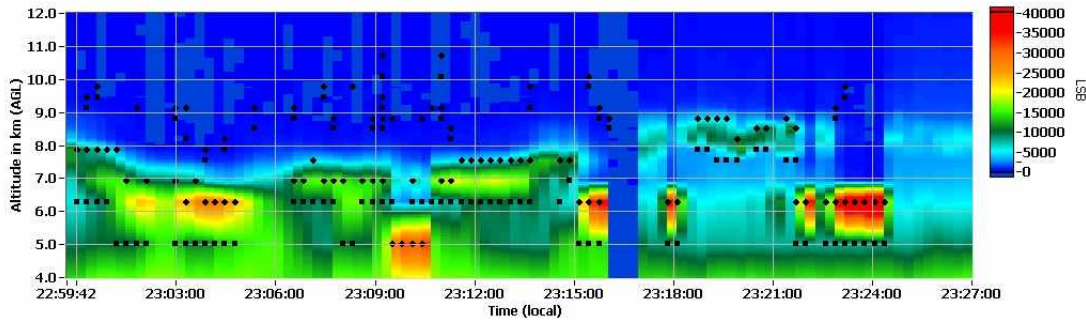


Figure 4.21: Range-corrected Mie receiver intensity (colour-coded) with detected cloud bases (black square) and tops (black diamonds) on 14.07.2007.

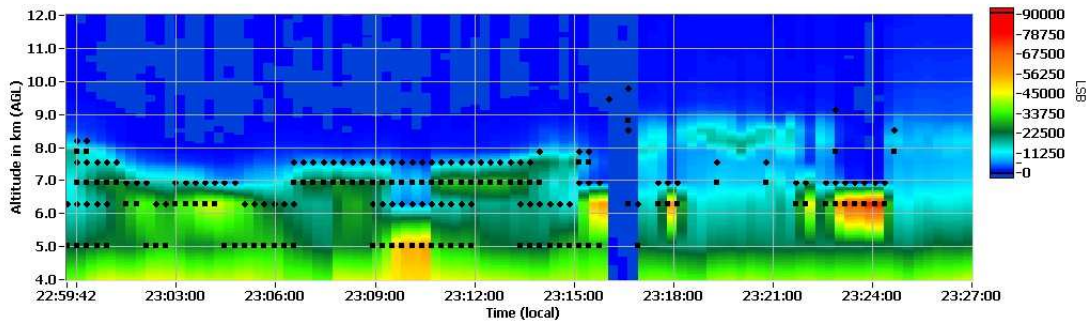


Figure 4.22: Rayleigh receiver intensity (colour-coded) with detected cloud bases (black square) and tops (black diamonds) on 14.07.2007.

on the Mie and the Rayleigh signal.

Figure 4.23 shows that the contour of the cloud is detected correctly, while details are missed. The same gets obvious for the Rayleigh detection (Figure 4.24). The Rayleigh detection shows a better correlation with the MULIS signal, even when the upper layer after 23:20 is not detectable. The mentioned noise on the Rayleigh spectrometer above the cloud is now identified as a cloud top with very low intensities.

Figure 4.25 shows the comparison of the MULIS backscatter intensity (red) and the Rayleigh (green) and Mie (blue) SNR. The MULIS backscatter intensities show several peaks with different, but low intensities, compared to the cirrus cloud in Section 4.2.1. The Mie and the Rayleigh SNR of A2D show only a slight increase caused by the weak

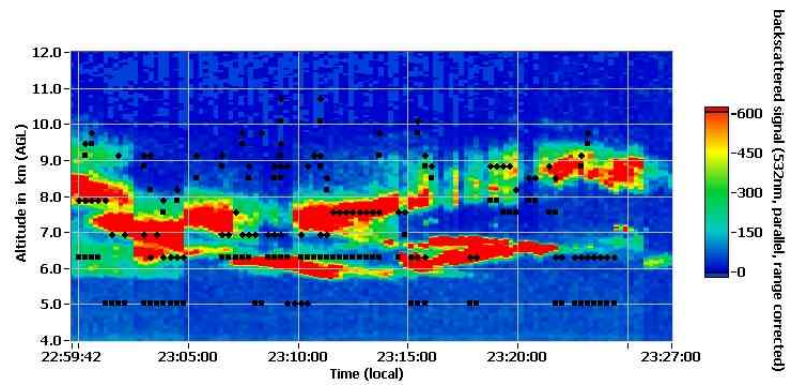


Figure 4.23: Range-corrected MULIS backscatter signal (colour-coded) with the A2D Mie Cloud Detection (black symbols) on 14.07.2007.

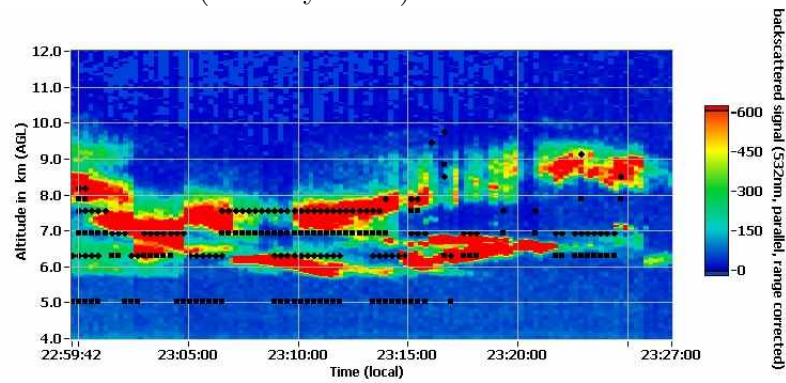


Figure 4.24: Range-corrected MULIS backscatter signal (colour-coded) with the A2D Rayleigh Cloud Detection (black symbols) on 14.07.2007.

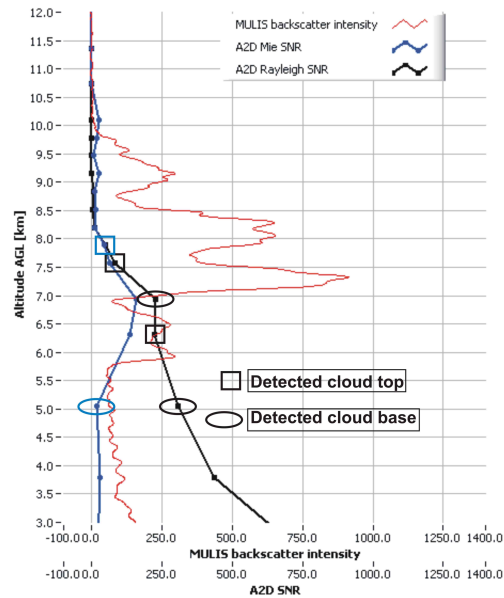


Figure 4.25: A2D Mie SNR (blue), A2D Rayleigh SNR (black) compared to the MULIS backscatter intensity (red) at 23:02 LT.

backscatter of the cirrus cloud layer. The cloud base starts to increase fairly slow at 5.7 *km* altitude with the “washed” cloud top in regions of 7.5 to 10.0 *km*. The Mie and the Rayleigh SNR show a faster decrease above 7.0 *km*.

So, this case shows, that clouds with low intensities are detectable on both spectrometers even when low detection thresholds for the SNR gradient cause “noise” detections.

4.2.5 Clear Sky and Thin Single Layer Cloud - 17.07.2007

The last analyzed case was measured on 17.07.2007 from 10:20 to 10:56 LT, with clear sky until 10:40. After 10:40 LT a medium altitude cloud layer was passing the measurement site. These clouds have similar properties like the cloud layer in section 4.2.3, with a small vertical extent.

The Mie detection (Figure 4.26) is working in a proper way, the clear sky event causes no failures. A thin cloud layer was detected with cloud bases at altitudes of 4.4 – 5.0 *km* and tops at 5.0 – 6.3 *km*.

For the same cloud case, the Rayleigh detection (Figure 4.27) shows almost the same results with lower variations at cloud base altitudes until 10:53 LT. Afterwards the same “jump” to lower altitudes of bases and altitudes is detected as on the Mie receiver.

The intercomparison of the MULIS backscatter signal and the A2D cloud detection (Figures 4.28 and 4.29) shows an overestimation of the cloud tops, while cloud bases are detected properly. The overestimation of the cloud tops is again caused by the vertical resolution of 0.6 *km* for an altitude of 2.5 *km* up to 5.0 *km* and only 1.3 *km* above 5.0 *km* height until an altitude of 11.3 *km* is reached. This resolution is called “Standard Mode” (Figure 3.4). The cloud top is again within two range bins and causes an overestimation of the cloud’s maximum altitude on both channels.

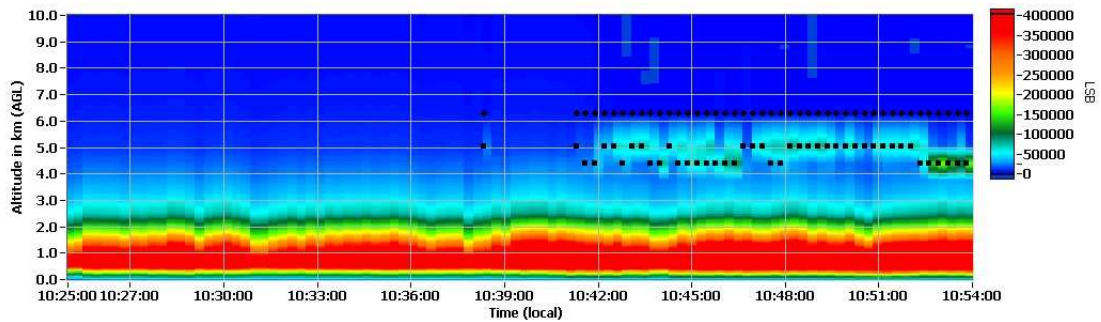


Figure 4.26: Range-corrected Mie receiver intensity (colour coded) with detected cloud bases (black square) and tops (black diamonds) on 17.07.2007.

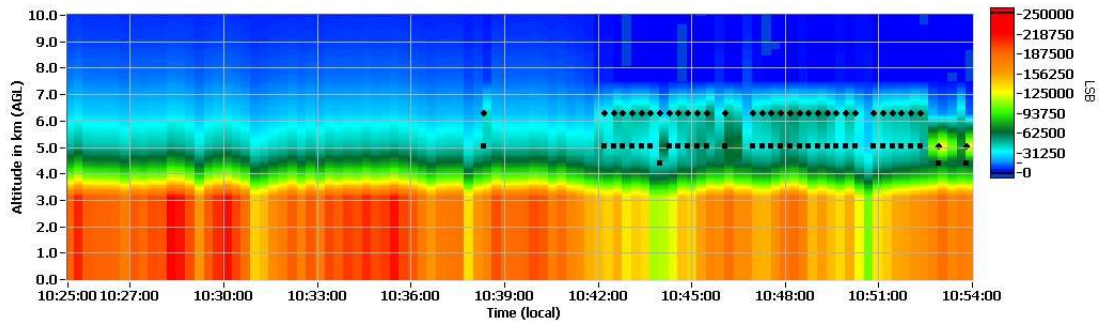


Figure 4.27: Range-corrected Rayleigh receiver intensity (colour coded) with detected cloud bases (black square) and tops (black diamonds) on 17.07.2007.

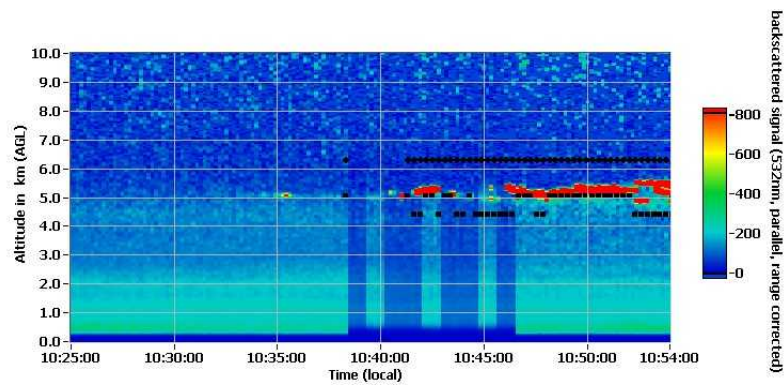


Figure 4.28: Range-corrected MULIS backscatter signal (colour coded) with the A2D Mie Cloud Detection (black symbols) on 17.07.2007.

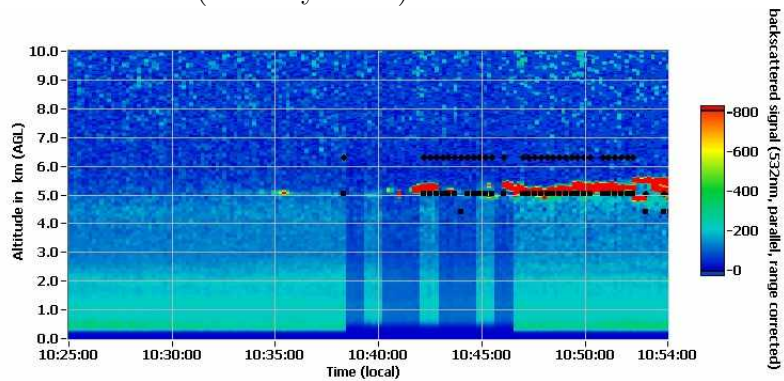


Figure 4.29: Range-corrected MULIS backscatter signal (colour coded) with the A2D Rayleigh Cloud Detection (black symbols) on 17.07.2007.

4.3 Discussion

In general it is proved, that the cloud detection algorithm, explained in Section 3.3 for the Mie and Section 3.4 for the Rayleigh spectrometer signals, works appropriate under different atmospheric conditions.

Cirrus clouds like in Sections 4.2.1 and 4.2.5 are detected well. This means for an altitude greater than 6 *km* bases and tops of clouds with a relatively low optical thickness are detected correctly compared with the measurements of the aerosol lidar MULIS and the cloud radar.

According to Section 4.2.1 structures of these clouds are detected. Only small deviations from the shape of the cloud measured by the MULIS lidar can be recognized.

For cirrus clouds with low backscatter intensity (Section 4.2.4) the weak Mie backscatter causes difficulties for the algorithm to find the exact cloud bases and tops. These problems are caused by the extinction of the signal in lower atmospheric layers, like the planetary boundary layer, where a strong Mie scattering is caused by high amounts of aerosols. The same influence is apparent on the Rayleigh signal with a slightly higher feasibility to detect cloud bases and tops in the right altitudes, even when different structures get visible.

Overall the results of these three cases show a comparable detection to the simulations in Sections 3.3.4 and 3.4.3 for Mie and Rayleigh signals, even when exact measurements of the cloud measured by A2D, MULIS and cloud radar show no indication on the cloud optical depth.

Another reason for some inferior detection quality compared to the simulations is the coarse vertical resolution for some cases. The cloud's bases and tops are not placed within the range bin of the maximum vertical resolution, so the feasibility of detecting the right vertical size of a cloud is lower than for simulated clouds.

In addition to the three cirrus cases above, validation was performed on mid-altitude and boundary layer clouds.

A very deep broken cumulus cloud was analyzed (Section 4.2.2). As mentioned, the telescope overlap of A2D causes serious detection problems close to the lidar for low altitudes of 0 to 2 *km*.

For mid-altitude clouds (Section 4.2.3) the detection quality is high as well. Only problems due to the lower vertical resolution lead to an overestimating of cloud tops while cloud bases are detected properly.

Overall, section 4.2 proves the correct detection of cloud bases, cloud tops, and cloud structures. The limitations are caused by the telescope overlap in the near field of A2D and by the coarse vertical resolutions.

Chapter 5

Conclusions

During this diploma thesis a cloud detection algorithm for the ALADIN airborne demonstrator A2D was developed and validated. The A2D is the airborne prototype for the future spaceborne lidar ALADIN on ADM-Aeolus.

The first task was the development of a flexible cloud simulator module for the A2D-Simulator. Changes in the atmospheric simulations led to variable one-layer cloud reproduction with various altitudes, thickness, and optical depth of different kinds of clouds, like cirrus, stratus, and cumulus clouds. Additionally, cloud bases and tops can be raised and lowered beside varying backscatter and extinction coefficients.

A cloud detection algorithm based on the Signal-to-Noise Ratio (SNR) of the Mie and the Rayleigh backscattered signal was developed. In order to separate the Mie signal from the Rayleigh background, a Lorentz-Function with constant offset was used.

Beside the SNR calculation, the Scattering Ratio was calculated for the Mie spectrometer signal, showing another option for cloud detection. The simulated Rayleigh SNR was derived using measured background noise. Due to the reflection of a small part of the Mie signal to the Rayleigh spectrometer, this signal can be used for cloud detection as well. Thus, cloud detection is possible for both spectrometers. For the SNR calculation of the Rayleigh signal, background noise has to be taken into account.

With the help of a pure height dependent gradient $\frac{\Delta SNR}{\Delta z}$ for the Mie SNR and a range-corrected, height dependent gradient $\frac{\Delta SNR}{\Delta z} \cdot R^2$ for the Rayleigh SNR, the cloud detection was performed with analyzing the global minimum and maximum of each

simulated atmospheric profile.

For high integration times (observation level, 630 laser pulses) the simulated minimum detectable cloud optical depth (COD) is:

- $2.4 \cdot 10^{-3}$ for the Mie detection, and
- $6.7 \cdot 10^{-3}$ for the Rayleigh detection.

For lower integration times (measurement level, 18 laser pulses) the minimum detectable COD shows a similar result of:

- $1.4 \cdot 10^{-2}$ for the Mie and the Rayleigh detection.

For high and low integration times comparable and even lower minimum detectable cloud optical depths to those of the CALIOP instrument onboard CALIPSO are reached. According to the simulations, subvisible cirrus clouds with a COD of $\sim 3.0 - 5.0 \cdot 10^{-2}$ are detectable even on measurement level.

The second part of the thesis was the adaption of the cloud detection algorithm for real observations. Therefore, changes in the algorithm were performed like the search for local minima and maxima of the gradients, considering the different intensities of real clouds by taking the average of these gradients into account, and some sorting algorithms to eliminate spuriously detected cloud bases and tops.

The detected cloud bases were compared with a cloud radar, operated by “Deutscher Wetterdienst” (DWD), and the aerosol backscatter lidar MULIS, developed operated by “Meteorologisches Institut der Universität München” (MIM). The analyses showed a good comparison for cirrus and medium altitude clouds.

According to this comparison even fine scale cloud structures were detected, like cloud fraction and holes.

Nevertheless, the detection is limited in the near field up to 2.0 km altitude by the telescope overlap function and by the coarse vertical resolution of typically 315 to 1260 km in the troposphere.

Chapter 6

Outlook

For further developments, it is proposed to automate the threshold determination for the Mie (Sections 3.3.5) and the Rayleigh (Sections 3.4.4) spectrometer signal. In this diploma thesis only fixed thresholds in combination with the averaged gradient of the Signal-to-Noise Ratio (SNR) over the whole profile are used to find cloud bases and tops. As explained for ICESat and CALIPSO (Section 2.4 and 2.5), a self-scaling threshold value has a much higher detection sensitivity than a fixed threshold.

This automation means that the different intensities of aerosols (boundary layer) and cloud backscatter should lead to a rescaling of the two threshold values, considering the attenuation forced by aerosols and clouds. For example, the maximum and the minimum of the gradient could be calculated in consideration of the backscatter intensities of the single layers.

Beside the threshold automation, an aerosol and cloud discriminator (c.f. Section 2.4 and 2.5) is the next step for the algorithm to retrieve exact values of aerosol layers within the atmosphere, but due to the telescope overlap, aerosol and cloud discriminations are solely feasible for airborne measurements in a downward looking geometry.

A testing for airborne measurements is necessary with the negative algebraic sign for the gradients of $\frac{\Delta SNR}{\Delta z}$ owing to the opposite measurement direction. In this case, especially the ground return has to be eliminated for the signal-to-noise ratio profiles and the gradients. In this case a lower detectable cloud optical depth should be reached due to the A2D measuring through almost clear air until the first layer is detected.

Additional this adaptation would give a first realistic guess on the possibility of using the cloud detection algorithm on the satellite ADM-Aeolus (Section 2.3).

An retrieval of the cloud optical depth can be performed due to the attenuation of the Rayleigh signal forced by clouds. Therefore a fit to the Rayleigh signal has to be performed from the cloudless parts of the profile.

The adaption of the multilayer cloud detection algorithm to other lidar instruments, like ceilometers achieving vertical resolutions of 10 *m* and lower is another option for the here designed cloud detection. Only a Signal-to-Noise Ratio depending on the backscatter intensity of the atmosphere is necessary.

List of Figures

1.1	Schematic view on the earth's annual global energy budget [Kiehl and Trenberth, 1997].	2
2.1	Schematic view on a spaceborne lidar	7
2.2	An example of Mie and Rayleigh backscatter intensities from a 355 nm (λ_0) lidar system versus wavelength. The spectrum in respect to 0 $\frac{m}{s}$ LOS wind speed (solid line) and a Doppler-shifted spectrum referring to a wind speed of 210 $\frac{m}{s}$ (dashed line) is illustrated [Paffrath, 2006].	9
2.3	Illustrated view on ADM-Aeolus in orbit.	10
2.4	LOS viewing geometry for ADM-Aeolus [Stoffelen et al., 2005].	12
2.5	Basis concept of the aerosol and cloud retrieval algorithm using ADM-Aeolus data [Flamant et al., 2008].	14
2.6	Illustrated view on ICESat.	15
2.7	Simulated GLAS profile of attenuated backscatter coefficients at 532 nm [Palm et al., 2002].	17
2.8	ICESat aerosol and cloud layer discrimination algorithm [Palm et al., 2002].	19
2.9	GLAS lidar over China, aerosol and cloud layer products [Spinhirne et al., 2005].	22
2.10	NASA afternoon train.	23
2.11	Attenuated backscatter coefficients and scattering ratios derived from LITE data [Vaughan et al., 2004].	28
2.12	Base detection on attenuated scattering ratio [Vaughan et al., 2004].	29

2.13	Threshold update after attenuation by feature regions [Vaughan et al., 2004].	30
3.1	A2D installed in the ground container [Reitebuch et al., 2008].	34
3.2	Schematic figure of the A2D receiver [Paffrath, 2006].	35
3.3	Transmission curve of the Fizeau interferometer [Paffrath, 2006].	36
3.4	Vertical sampling modes of A2D during the 2nd Ground Campaign [Paffrath et al., 2008].	37
3.5	Conception of the A2D-Simulator.	39
3.6	Profiles from ESA-RMA: temperature and pressure.	41
3.7	Molecular backscatter β_{Mol} and extinction α_{Mol} coefficient resulting from the U.S. Standard Atmosphere at $0.355 \mu m$	42
3.8	RMA-Profiles for the aerosol backscatter β_A and the aerosol extinction α_A at a wavelength of $0.355 \mu m$	43
3.9	Graphical user interface of the cloud simulator.	45
3.10	Simulated cirrus clouds with a cloud base at $12 km$ and its top at $13 km$ altitude with different cloud optical depths.	46
3.11	Two-way Transmission calculated for molecular (blue), aerosol (red, Median model), and summarized (green) extinction coefficients.	48
3.12	Detected signal on the Mie ACCD with the schematic variables of the Lorentz function calculation.	50
3.13	Mie SNR of clear atmosphere and a simulated cirrus cloud at $10 km$ with a geometric depth of $1 km$ ($COD = 0.2$).	52
3.14	Scattering ratio of a cirrus cloud at $10 km$ altitude with a depth of $1 km$ ($COD = 0.2$).	55
3.15	Mie SNR-gradient of a clear atmosphere (left) and a cirrus cloud at $10 km$ with a depth of $1 km$ (right).	57
3.16	Mie channel cloud detection algorithm for the A2D-Simulator.	58
3.17	Extinction and two-way Transmission of a cirrus cloud at an altitude of $10 km$ and a depth of $1 km$ in the simulated U.S. Standard Atmosphere with Median aerosol model.	59

3.18	Number of electrons on Rayleigh ACCD for ground, airborne, and satellite system [Paffrath et al., 2008].	60
3.19	Mie SNR-gradient and the scattering ratio calculated for observation level (630 laser pulses) for different simulations.	62
3.20	Mie SNR-gradient calculated at measurement level for different simulations.	63
3.21	Mie receiver intensity, range corrected, 08.07.2007 from 22:06 to 22:27 (LT) with schematic detection of cloud base and cloud top.	65
3.22	Mie SNR of a simulated cirrus at 9 km and of a measured cirrus on the 08.07.2007 from 22:06 to 22:27 (LT).	67
3.23	Mie SNR-gradient of a simulated cirrus at 9 km and of a measured cirrus on 08.07.2007 from 22:06 to 22:27 (LT).	67
3.24	Multilayer cloud detection algorithm for the Aladin Airborne Demonstrator for the Mie spectrometer signal.	68
3.25	Mie receiver intensity, range corrected, 08.07.2007 from 22:06 to 22:27 (LT) with detection of cloud base and top.	69
3.26	Simulated Rayleigh SNR for a clear atmosphere and with a cirrus cloud at 10 km with a geometrical depth 1 km ($COD = 0.2$).	71
3.27	Rayleigh SNR-gradient (left) and range-corrected SNR-gradient (right) in case of a cirrus cloud at 10 km with a geometrical depth of 1 km and a cloud optical depth of 0.2.	73
3.28	Rayleigh channel cloud detection algorithm for the A2D-Simulator. . .	75
3.29	Rayleigh SNR for a simulated cirrus at an altitude of 9 km and a cloudy case on 08.07.2007 from 22:06 to 22:26 (LT) and the range-corrected SNR-gradients.	78
3.30	Cloud bases and tops for the Rayleigh (yellow) and the Mie (red) detection algorithm on the 08.07.2007 from 22:06 to 22:26 (LT).	79
4.1	Measurement set-up, Lindenberg in July 2007.	82
4.2	Aerosol backscatter lidar MULIS set up in trailer.	84
4.3	Range-corrected Mie receiver intensity (colour coded) with detected cloud bases (black square) and tops (black diamonds) on 08.07.2007.	86

4.4	Range-corrected Rayleigh receiver intensity (colour coded) with detected cloud bases (black square) and tops (black diamonds) on 08.07.2007.	86
4.5	Signal-to-Noise Ratio of the Mie (blue) and the Rayleigh (green) channel at 22:24:30.	86
4.6	Range-corrected MULIS backscatter signal (colour coded) with the A2D Mie Cloud Detection (black symbols) on 08.07.2007.	88
4.7	Range-corrected MULIS backscatter signal (colour coded) with the A2D Rayleigh Cloud Detection (black symbols) on 08.07.2007.	88
4.8	A2D Mie SNR (blue), A2D Rayleigh SNR (black) compared to the MULIS backscatter intensity (red) at 22:12.	88
4.9	Range-corrected Mie receiver intensity (colour coded) with detected cloud bases (black square) and tops (black diamonds) on 11.07.2007.	90
4.10	Range-corrected Rayleigh receiver intensity (colour coded) with detected cloud bases (black square) and tops (black diamonds) on 11.07.2007.	90
4.11	Range-corrected MULIS backscatter signal (colour coded) with the A2D Mie Cloud Detection (black symbols) on 11.07.2007.	91
4.12	Range-corrected MULIS backscatter signal (back) with the A2D Rayleigh Cloud Detection (black symbols) on 11.07.2007.	91
4.13	Reflectivity factor of the DWD cloud radar (colour coded) and cloud bases detected by Ceilometer (black dots) on 13.07.2007.	92
4.14	Range-corrected Mie receiver intensity (colour coded) with detected cloud bases (black square) and tops (black diamonds) on 13.07.2007.	93
4.15	Range-corrected Rayleigh receiver intensity (colour coded) with detected cloud bases (black square) and tops (black diamonds) on 13.07.2007.	93
4.16	SNR gradients of the cloud detection routine for the Mie channel (blue) and the Rayleigh channel (green) at 21:43 LT. The threshold limits for Mie (straight lines, blue) and for Rayleigh (straight lines, green).	93
4.17	Range-corrected MULIS backscatter signal (colour coded) with the A2D Mie Cloud Detection (black symbols) on 13.07.2007.	95
4.18	Range-corrected MULIS backscatter signal (colour coded) with the A2D Rayleigh Cloud Detection (black symbols) on 13.07.2007.	95

4.19	A2D Mie SNR (blue), A2D Rayleigh SNR (black) compared to the MULIS backscatter intensity (red) at 21:43 LT.	95
4.20	Reflectivity factor of the DWD cloud radar (colour coded) and cloud bases detected by Ceilometer (black dots) on 14.07.2007.	96
4.21	Range-corrected Mie receiver intensity (colour-coded) with detected cloud bases (black square) and tops (black diamonds) on 14.07.2007.	97
4.22	Rayleigh receiver intensity (colour-coded) with detected cloud bases (black square) and tops (black diamonds) on 14.07.2007.	97
4.23	Range-corrected MULIS backscatter signal (colour-coded) with the A2D Mie Cloud Detection (black symbols) on 14.07.2007.	98
4.24	Range-corrected MULIS backscatter signal (colour-coded) with the A2D Rayleigh Cloud Detection (black symbols) on 14.07.2007.	98
4.25	A2D Mie SNR (blue), A2D Rayleigh SNR (black) compared to the MULIS backscatter intensity (red) at 23:02 LT.	99
4.26	Range-corrected Mie receiver intensity (colour coded) with detected cloud bases (black square) and tops (black diamonds) on 17.07.2007.	101
4.27	Range-corrected Rayleigh receiver intensity (colour coded) with detected cloud bases (black square) and tops (black diamonds) on 17.07.2007.	101
4.28	Range-corrected MULIS backscatter signal (colour coded) with the A2D Mie Cloud Detection (black symbols) on 17.07.2007.	102
4.29	Range-corrected MULIS backscatter signal (colour coded) with the A2D Rayleigh Cloud Detection (black symbols) on 17.07.2007.	102

List of Tables

2.1	Comparative attributes of aerosol and cloud layers	20
2.2	Measurement objectives of the CALIPSO mission [Winker et al., 2002].	24
3.1	Backscatter and extinction coefficient depending on cloud types, designed in the ESA RMA [Vaughan et al., 1998].	44
3.2	Minimum detectable cloud optical depth for the simulations (observation and measurement level) with decreasing backscatter and extinction coefficients and decreasing cloud depth.	64
3.3	Minimum detectable cloud optical depth for the Mie and the Rayleigh simulations (observation and measurement level) with decreasing backscatter and extinction coefficients and decreasing cloud depth.	75

Appendix

Acronyms

A2D	ALADIN Airborne Demonstrator
ACCD	Accumulation Charge-Coupled Device
ALADIN	Atmospheric Laser Doppler Instrument
ADM	Atmospheric Dynamics Mission
CALIOP	Cloud-Aerosol Lidar with Orthogonal Polarization
CALIPSO	Cloud-Aerosol Lidar and Infrared Pathfinder Satellite Observations
CCD	Charge-Coupled Device
COD	Cloud Optical Depth
DLR	Deutsches Zentrum für Luft- und Raumfahrt
DWD	Deutscher Wetterdienst
DWL	Doppler Wind Lidar
EARLINET	European Aerosol Research Lidar Network
ESA	European Space Agency
FWHM	Full-Width-Half-Maximum
GCM	Global Circulation Model
GLAS	Geoscience Laser Altimeter System
GMAO	Global Modelling and Assimilation Office
HLOS	Horizontal Line of Sight
ICESat	Ice, Cloud and Land Elevation Satellite
IIR	Imaging Infrared Radiometer

IPCC	Intergovernmental Panel on Climate Change
ISCCP	International Satellite Cloud Climatology Project
LASER	Light Amplification by Stimulated Emission of Radiation
LIDAR	Light Detection and Ranging
LITE	Lidar In-space Technology Experiment
LOD	Local Optical Depth
LOSU	Level of Scientific Understanding
LSB	Least Significant Bit
LT	Local time
MBV	Measured Backscatter Variation
MIM	Meteorologisches Institut der Universität München
MULIS	Multiple wavelengths Lidar System
NASA	National Aeronautics and Space Administration
Nd:YAG	Neodymium doped Yttrium Aluminium Garnet
NWP	Numerical Weather Prediction
PDM	Pre-Development Model
RADAR	Radio Detection and Ranging
RBV	Relative backscatter variation
RF	Radiative Forcing
RMA	Reference Model Atmosphere
SCA	Scene Classification Algorithm
SNR	Signal-to-Noise Ratio
STD	Standard Deviation
UTC	Universal Time Coordinated
WFC	Wide Field Camera

Constants

Velocity of light	$c = 2.9979 \cdot 10^8$	$\frac{m}{s}$
Planck's constant	$h = 6.625 \cdot 10^{-34}$	$J \cdot s$
Loschmidt's number ($T = 23^\circ$, $p = 1013 \text{ hPa}$)	$N_L = 2.4791019 \cdot 10^{25}$	m^{-3}

Symbols

a	Height of the Lorentz function	
A	Airy function	
$\frac{A_0}{R^2}$	Acceptance solid angle of the receiving optics	rad
C	Offset of the Lorentz function	
C_λ	Calibration constant at wavelength λ	$mJ\ m\ sr$
E, E_L	Laser energy	mJ
F	Finesse	
G_A	Amplifier gain	
j	Number of pixel on the Mie ACCD	$pixel$
j_0	Position of peak value	$pixel$
k	Instrument constant	
L	Lorentz function	
L_0	Peak value of the signal	$pixel$
N_{Mol}	Number of molecules per volume	cm^{-3}
N_{ph}	Number of photons emitted by laser	
p	Pressure	hPa
P	Received lidar signal	
P'_λ	Normalized lidar signal	
R	Range to target	m
Rf	Reflection	
ΔR	Range resolution	
S_A	Aerosol lidar ratio	sr
S_{Mol}	Molecular lidar ratio	sr
SNR	Signal-to-Noise Ratio	
t	time	s
t_i	Integration time of measurement pixel	s
t'_i	Integration time of background pixel	s
T	Temperature	K
T^2	Two-way transmission	
z	Altitude	m

Greek Symbols

α	Extinction coefficient	m^{-1}
α_A	Aerosol extinction coefficient	m^{-1}
α_M, α_{Mol}	Molecular extinction coefficient	m^{-1}
β	Backscatter coefficient	$m^{-1}sr^{-1}$
β_A, β_{Aer}	Aerosol backscatter coefficient	$m^{-1}sr^{-1}$
β_M, β_{Mol}	Molecular backscatter coefficient	$m^{-1}sr^{-1}$
β_P	Particulate backscatter coefficient	$m^{-1}sr^{-1}$
$\beta'(\lambda)$	Attenuated backscatter coefficient	$m^{-1}sr^{-1}$
$\gamma_{feature}$	Integrated attenuated backscatter	$m^{-1}sr^{-1}$
λ_L	Wavelength	m
ρ	Scattering Ratio	
σ_{Mol}	Molecular Rayleigh backscatter cross section	m^2sr^{-1}
τ	Cloud optical depth	
ψ	Optical separation of the Fabry-Perot interferometer plates	cm

Bibliography

- S. Arrhenius. On the influence of carbonic acid in the air upon the temperature of the ground. *The London, Edinburgh, and Dublin Philosophical Magazine and Journal of Science*, Vol. 5, pp. 237-276, 1896.
- J. Bösenberg and V. Matthias. EARLINET: A European Aerosol Research Lidar Network to Establish an Aerosol Climatology. Report 348, 191 pp., [available at: Max-Planck-Institut for Meteorology, Hamburg, Germany], September 2003.
- I. N. Bronstein, K. A. Semendjajew, G. Musiol, and H. Mühlig. *Taschenbuch der Mathematik*. Verlag Harri Deutsch, Thun und Frankfurt am Main, 5th edition, 1195 pp., ISBN: 3-8171-2005-2, 2001.
- K. S. W. Champion. Standard and reference atmospheres. In *Handbook of geophysics and the space environment*. p. 14-1, United States Air Force Geophysics Laboratory, 1985.
- Y. Durand, R. Meynard, M. Endemann, E. Chinal, D. Morançais, T. Schröder, and O. Reitebuch. Manufacturing of an airborne demonstrator of ALADIN: the direct detection Doppler wind lidar for ADM-Aeolus. *Proc. of SPIE - Int. Symposium on Remote Sensing*, Vol. 5984, October 2005.
- Y. Durand, E. Chinal, M. Endemann, R. Meynard, O. Reitebuch, and R. Treichel. ALADIN Airborne Demonstrator: a Doppler Wind Lidar to prepare ESA's ADM-Aeolus Explorer Mission. *SPIE*, Vol. 6296, No. 1D, 9 pp., 2006.
- M. Endemann, A. Culoma, D. Wernham, and W. Veith. Characterization & Qualifica-

- tion Status of the ADM-Aeolus Mission. In *24th International Lidar Radar Conference*, pp. 1220-1223, Boulder, Colorado, 23-27 June 2008.
- ESA. *ADM-Aeolus Science Report*. European Space Agency (ESA), [available at: ESTEC, P.O. Box 299, 2200 AG Noordwijk, The Netherlands], SP-1311, 121 pp., ISBN: 9-2922-1404-3, April 2008.
- ESA. *Atmospheric Dynamics Mission - The four candidate Earth Explorer Core missions: Reports for Mission selection*. European Space Agency (ESA), [available at: ESTEC, P.O. Box 299, 2200 AG Noordwijk, The Netherlands], SP-1233, 157 pp., ISBN: 9-2909-2528-0, 1999.
- A. T. Evan, A. K. Heidinger, and D. J. Vimont. Arguments against a physical long-term trend in global ISCCP cloud amounts. *Geophys. Res. Lett.*, 34, No. 4, L04701, doi: 10.1029/2006GL028083, February 2007.
- P. Flamant, J. Cuesta, M.-L. Denneulin, A. Dabas, and D. Huber. ADM-Aeolus retrieval algorithms for aerosol and cloud products. *TELLUS A*, Vol. 60, pp. 273-286, September 2008.
- V. Freudenthaler, M. Esselborn, M. Wiegner, B. Heese, M. Tesche, A. Ansmann, D. Müller, D. Althausen, M. Wirth, A. Fix, G. Ehret, P. Knippertz, C. Toledano, J. Gasteiger, M. Garhammer, and M. Seefeldner. Depolarization ratio profiling at several wavelengths in pure Saharan dust during SAMUM 2006. *TELLUS*, Vol. 61, 15 pp., 2009.
- E. F. Harrison, P. Minnis, B. R. Barkstrom, V. Ramanathan, R. D. Cess, and G. G. Gibson. Seasonal variation of cloud radiative forcing derived from the Earth Radiation Budget Experiment. *J. Geophys. Res.*, Vol. 95, No. D18, pp. 18687-18703, 1990.
- W. C. Hinds. *Aerosol Technology - Properties, Behavior, and Measurement of Airborne Particles*. John Wiley Sons, Inc., New York, 504 pp., ISBN: 0-4711-9410-1, 2nd edition, 1998.

- IPCC. *Climate Change 2007 - Synthesis Report*. Intergovernmental Panel on Climate Change, [available at: C/o World Meteorological Organization (WMO), 7bis avenue de la Paix, P.O. Box No. 2300, CH- 1211 Geneva 2, Switzerland], 52 pp., ISBN: 9-2916-9122-4, June 2008.
- M. Iqbal. *An Introduction to Solar Radiation*. Academic Press, Orlando, Florida, United States, 390 p., ISBN: 0-1237-3750-8, January 1984.
- B. Kärcher. Properties of subvisible cirrus clouds formed by homogeneous freezing. *Atmos. Chem. Phys.*, Vol. 2, pp. 161-170, June 2002.
- J. T. Kiehl and K. E. Trenberth. Earth's Annual Global Mean Energy Budget. *Bull. Am. Meteorol. Soc.*, Vol. 78, No. 2, pp.197-208, February 1997.
- Z. Liu, M. Vaughan, D. Winker, C. Hostetler, L. Poole, D. Hlavka, W. Hart, and M. McGill. Use of probability distribution functions for discriminating between cloud and aerosol in lidar backscatter data. *J. Geophys. Res.*, Vol. 109, D15202, doi: 010.1029/2004/JD004732, August 2004.
- Z. Liu, M. Vaughan, C. Kittaka, R. E. Kuehn, A. Omar, and K. Powell. The CALIPSO Lidar Cloud and Aerosol Discrimination: Version 2 - Algorithm, Performance and Validation Strategies. In *24th International Lidar Radar Conference*, pp. 1133-1136, Boulder, Colorado, 23-27 June 2008.
- R. M. Measures. *Laser Remote Sensing - Fundamentals and Applications*. Krieger Publishing Company, Krieger Drive, Malabar, Florida 32950, 524 p., ISBN: 0-8946-4619-5, August 1991.
- I. I. Mokhov and M. Schlesinger. Analysis of Global Cloudiness 1. Comparison of Meteor, Nimbus 7, and International Satellite Cloud Climatology Project (ISCCP) Satellite Data. *J. Geophys. Res.*, Vol. 98, No. D7, pp. 849-868, March 1993.
- I. I. Mokhov and M. E. Schlesinger. Analysis of Global Cloudiness, 2, Comparison ground-based and satellite-based cloud climatologies. *J. Geophys. Res.*, Vol. 99, No. D8, pp. 45-65, April 1994.

- U. Paffrath. *Performance assessment of the Aeolus Doppler wind lidar prototype*. Deutsches Zentrum für Luft und Raumfahrt (DLR e.V.), [available at: Oberpfaffenhofen, Germany], Forschungsbericht 2006-12, 144 pp., ISSN: 1434-8454, June 2006.
- U. Paffrath, O. Reitebuch, and I. Nikolaus. TN 5.1 - ADM-Aeolus Ground Campaigns Results. Technical Note AE.TN.DLR.A2D.TN51.310708, Deutsches Zentrum für Luft- und Raumfahrt (DLR e.V.), Oberpfaffenhofen, Germany, July 2008.
- S. Palm, W. D. Hart, D. L. Hlavka, E. J. Welton, A. Mahesh, and J. D. Spinhirne. Geoscience Laser Altimeter System (GLAS) - Algorithm Theoretical Basis Document - GLAS Atmospheric Data Products. Algorithm theoretical basis document, Goddard Space Flight Center, Greenbelt, MD 20771, [available at http://eosps0.gsfc.nasa.gov/eos_homepage/for_scientists/atbd/docs/GLAS/ATBD-GLAS-01.pdf], October 2002.
- S. P. Palm, A. Benedetti, and J. Spinhirne. Validation of ECMWF global forecast model parameters using GLAS atmospheric channel measurements. *Geophys. Res. Lett.*, Vol. 32, L22S09, doi: 10.1029/2005GL023535, September 2005.
- O. Reitebuch. Technical Note TN 3.1 - ADM-Aeolus Ground Campaign Implementation Plan. Doc. No.: AE.TN.DLR.A2D.TN31.080906, 32 pp., [available at: Deutsches Zentrum für Luft- und Raumfahrt (DLR e.V.), Oberpfaffenhofen, Germany], September 2006.
- O. Reitebuch and M. Weissmann. Impact of Airborne and Future Spaceborne Wind Lidar Observations of ADM-Aeolus on Weather Prediction Skills. In *24th International Lidar Radar Conference*, pp. 211-213, Boulder, Colorado, 23-27 June 2008.
- O. Reitebuch, M. Endemann, D. Engelbart, V. Freudenthaler, V. Lehmann, C. Lemmerz, E. Nagel, U. Paffrath, S. Rahm, and B. Witschas. Pre-Launch Validation of ADM-Aeolus with an Airborne Direct-Detection Wind Lidar. In *24th International Lidar Radar Conference*, pp. 41-44, Boulder, Colorado, 23-27 June 2008.
- W. B. Rossow and R. A. Schiffer. Advances in Understanding Clouds from ISCCP. *Bull. Am. Meteorol. Soc.*, Vol. 80, No. 11, doi: 10.1175/1520-0477(1999)080, pp. 2261-2287, November 1999.

- T. Schröder, C. Lemmerz, O. Reitebuch, M. Wirth, C. Wührer, and R. Treichel. Frequency jitter and spectral width of an injection-seeded Q-switched Nd:YAG laser for a Doppler wind lidar. *Appl. Phys. B*, Vol. 87, No. 3, doi: 10.1007/s00340-007-2627-5, pp. 437-444, May 2007.
- J. D. Spinhirne, S. P. Palm, W. D. Hart, D. L. Hlavka, and E. J. Welton. Cloud and aerosol measurements from GLAS: Overview and initial results. *Geophys. Res. Lett.*, Vol. 32, L22S03, doi: 10.1029/2005GL023507, September 2005.
- A. Stoffelen, J. Pailleux, J. M. Vaughan, L. Isaksen, P. Flamant, W. Wergen, E. Andersson, H. Schyberg, A. Culoma, R. Meynart, M. Endemann, and P. Ingmann. The Atmospheric Dynamics Mission for Global Wind Field Measurement. *Bull. Am. Meteorol. Soc.*, Vol. 86, No. 1, doi: 10.1175/BAMS-86-1-73, pp. 73-87, January 2005.
- J. Streicher, D. Huber, U. Paffrath, O. Reitebuch, and I. Leike. Technical Note TN 2.1 - Sensitivity Analysis. Doc. No. AE.TN.DLR.GS.TN2.1-V3.4-290906, [available at: Deutsches Zentrum für Luft- und Raumfahrt (DLR e.V.), Oberpfaffenhofen, Germany], September 2006.
- D. G. H. Tan, E. Andersson, J. de Kloe, G.-J. Marseille, A. Stoffelen, P. Poli, M.-L. Denneulin, A. Dabas, D. Huber, O. Reitebuch, P. Flamant, O. L. Rille, and H. Nett. The ADM-Aeolus wind retrieval algorithms. *TELLUS A*, Vol. 60, No. 2, doi: 10.1111/j.1600-0870.2007.00285.x, pp. 191-205, November 2007.
- J. M. Vaughan, D. W. Brown, C. Nash, S. B. Alejandro, and G. G. Koenig. Atlantic atmospheric aerosol studies 2. Compendium of airborne backscatter measurements at $10.6\mu\text{m}$. *J. Geophys. Res.*, Vol. 100, No. D1, pp. 1043-1065, 1995.
- J. M. Vaughan, C. Flesia, and P. H. Flamant. Establishment of a backscatter coefficient and atmospheric database. Final Report, ESA contract 12510/97/NL/RE, [available at: Defence Evaluation and Research Agency UK (DERA), Farnborough, Hampshire GU14 0LX, UK], June 1998.
- M. Vaughan, S. Young, D. Winker, K. Powell, A. Omar, Z. Liu, Y. Hu, and C. Hostetler. Fully automated analysis of space-based lidar data: an overview of the Calipso re-

- trieval algorithms and data products. *SPIE*, Vol. 5575, doi: 10.1117/12.572024, pp. 16-30, 2004.
- M. Vaughan, D. Winker, and K. Powell. CALIOP Algorithm Theoretical Basis Document, Part 2: Feature Detection and Layer Properties Algorithms. Algorithm Theoretical Basis Document No. PC-SCI-202 Part 2, [available at: NASA Langley Research Center, Hampton, Virginia, USA], September 2005.
- M. Vaughan, R. E. Kuehn, S. Young, M. J. McGill, Z. Liu, and Y. Hu. Validating Cirrus Clouds Optical Properties Retrieved by CALIPSO. In *24th International Lidar Radar Conference*, pp. 1090-1093, Boulder, Colorado, 23-27 June 2008.
- J. M. Wallace and P. V. Hobbs. *Atmospheric Science - An Introductory Survey*. Academic Press, 504 pp., ISBN: 0-1273-2951-2, 2nd edition, March 2006.
- U. Wandinger, A. Ansmann, I. Mattis, D. Müller, and G. Papparlardo. CALIPSO and beyond: Long-Term Ground-Based Support Of Space-Borne Aerosol And Cloud Lidar Missions. In *24th International Lidar Radar Conference*, pp. 715-718, Boulder, Colorado, 23-27 June 2008.
- Z. Wang and K. Sassen. Cloud Type and Macrophysical Property Retrieval Using Multiple Remote Sensors. *J. Appl. Meteorol.*, Vol. 40, pp. 1665-1682, doi: 10.1175/1520-0450(2001)040, October 2001.
- C. Weitkamp. *LIDAR - Range-Resolved Optical Remote Sensing of the Atmosphere*. Springer, Berlin, 460 pp., ISBN: 0-387-40075-3, August 2005.
- M. Wiegner, H. Quenzel, D. Rabus, W. Volker, P. Volger, J. Ackermann, C. Kahler, F. Fergg, and G. Wildgruber. Mobile three-wavelength backscatter lidar of the Meteorological Institute of the University of Munich. *Proc. of SPIE - Lidar and Atmospheric Sensing*, Vol. 2505, pp. 2-10, doi: 10.1117/12.219632, 15 September 1995.
- B. A. Wielicki and L. Parker. On the Determination of Cloud Cover From Satellite Sensors: The Effect of Sensor Spatial Resolution. *J. Geophys. Res.*, Vol. 97, No. D12, pp. 799-823, 1992.

- D. Winker, C. Hostetler, M. Vaughan, and A. Omar. CALIOP Algorithm Theoretical Basis Document, Part 1: CALIOP Instrument, and Algorithm Overview. Algorithm Theoretical Basis Document No. PC-SCI-202 Part 1, [available at: NASA Langley Research Center, Hampton, Virginia, USA], September 2006.
- D. Winker, B. Getzewitch, and M. Vaughan. Evaluation and Applications of Cloud Climatologies from CALIOP. In *24th International Lidar Radar Conference*, pp. 1079-1082, Boulder, Colorado, 23-27 June 2008.
- D. M. Winker, J. Pelon, and M. P. McCormick. The CALIPSO mission: Spaceborne lidar for observation of aerosols and clouds. *Proc. of SPIE - Lidar Remote Sensing for Industry and Environment Monitoring III, Hangzhou, China*, Vol. 4893, 24-25 October 2002.
- D. M. Winker, W. H. Hunt, and M. J. McGill. Initial performance assessment of CALIOP. *Geophys. Res. Lett.*, Vol. 34, L19803, doi: 10.1029/2007GL030135, October 2007.
- B. Witschas. Characterisation of beam profile and frequency stability of an injection-seeded Nd:YAG laser for a Doppler wind lidar system. Master's thesis, Hochschule München, Fachbereich 06 Physikalische Technik, Munich, Germany, December 2007.
- H. J. Zwally, B. Schutz, W. Abdalati, J. Abshire, C. Bentley, A. Brenner, J. Bufton, J. Dezio, D. Hancock, D. Harding, T. Herring, B. Minster, K. Quinn, S. Palm, J. Spinhirne, and R. Thomas. ICESat's laser measurements of polar ice, atmosphere, ocean, and land. *J. Geodyn.*, Vol. 34, No. 3-4, pp. 405-445, doi: 10.1016/S0264-3707(02)00042-X, 2002.

Acknowledgements

I would like to express my deepest gratitude to my mentor Dr. Oliver Reitebuch for the guidance he provided during the study of this thesis and for never being tired of answering my questions and giving advises, as well as Dr. Matthias Wiegner of “Meteorologisches Institut der Universität München” (MIM) for professional and extensive advises during this diploma thesis.

I am grateful to Professor Dr. U. Schumann, director of “Institut für Physik der Atmosphäre” (DLR) and to Dr. G. Ehret, head of the lidar group, for their encouragement giving me the opportunity to carry out this research work.

My special thanks goes to Dr. Ulrike Paffrath for supporting my programming work, data analyses, and countless discussions. I wish to thank Christian Lemmerz, Engelbert Nagel, Jürgen Streicher and Benjamin Witschas for being a very cooperative and helpful team for the ten months of my work in the lidar department. I also want to thank the whole lidar department of DLR for the preeminently support.

I would like to thank Dr. Volker Freudenthaler, Franziska Schnell, Silke Groß, Markus Eifried, and Theresa Schadow of “Meteorologisches Institut der Universität München” (MIM) for performing the MULIS measurements during the second ADM-Aeolus ground campaign in July 2007 and for preparing and analyzing the data,.

I want to appreciate Dr. Ulrich Görzdorf for performing and analyzing the used cloud radar data, and Dr. Volker Lehmann as well as Dr. Dirk Engelbart of “Deutscher Wetterdienst” (DWD) for making the ground campaign possible at the Observatory Lindenberg of the DWD.

I am very indebted to my parents Marion and Hans Jürgen, my brother Wolfgang (who corrected this thesis during sleepless nights), and my girlfriend Mariana for giving me their love and their support in all respects.

Name: Stephan Kox
Geb.: 09.01.1982
Matr.Nr.: 18204858
Semester WS 08/09

Erklärung

gemäß §16 Abs. 8 Diplomprüfungsordnung

Hiermit erkläre ich, dass ich die Diplomarbeit selbstständig verfasst, noch nicht anderweitig für Prüfungszwecke vorgelegt, keine anderen als die angegebenen Quellen oder Hilfsmittel benutzt, sowie wörtliche und sinngemäße Zitate als solche gekennzeichnet habe.

Ort, Datum

Unterschrift